Characterising concrete using micro X-ray fluorescence (μXRF)

Fatmawati Abdul Wahid

Department of Civil and Environmental Engineering

Imperial College London

November 2016

A thesis submitted in fulfilment of the requirements for the degree of

Doctor of Philosophy and Diploma of Imperial College London

Declaration

I hereby declare that this thesis, submitted for the degree of Doctor of Philosophy and Diploma of Imperial College London is the result of my own work, and that all else is appropriately referenced.

The copyright of this thesis rests with the author and is made available under a Creative Commons Attribution Non-Commercial No Derivatives licence. Researchers are free to copy, distribute or transmit the thesis on the condition that they attribute it, that they do not use it for commercial purposes and that they do not alter, transform or build upon it. For any reuse or redistribution, researchers must make clear to others the licence terms of this work.

Signature:



Date: 6 November 2016

“My Lord, increase me in knowledge”

Quran 20:114

Abstract

Micro X-ray fluorescence (μXRF) is a relatively new technique that is able to perform elemental analyses at high resolution. However, very few studies have been carried out to apply this technique for cement and concrete research. This thesis aims to develop, optimise, and exploit μXRF as a technique for characterising concrete and for studying transport of aggressive species such as chloride and sulphate in cement-based materials. This is important because μXRF has several advantages over existing techniques and the ability to detect the presence of aggressive species, measure their amount and rate of penetration is a key aspect in characterising long-term durability of concrete structures.

The effect of seven operating conditions of μXRF on its sensitivity to chloride and sulphate was first investigated to understand factors influencing accuracy and to determine optimum operating conditions. The results show that the signal-to-noise ratio (SNR) and limit of detection (LOD) for chloride and sulphur improves when the analysis is carried out at higher beam voltages, longer acquisition times, in vacuum chamber and using a 30 μm beam spot. The application of 25 μm aluminium filter improves chloride analysis, but this is not necessary for sulphur analysis. A dead time of 30 – 50% and an amplifier time constant of 12.8 μs is recommended to obtain an optimised set-up. At these conditions, a LOD of 0.007% wt. cement for chloride and 0.003% wt. cement for sulphur is achievable.

The ability to separate cement paste regions from aggregate particles during μXRF analysis is important as it helps to reduce signal interference and allow measurements solely on cement paste or aggregate particles. A new approach for identifying cement paste regions in mortars and concretes has been developed. This method is based on exploiting the change in dead time when the beam samples cement paste or aggregate regions. The main advantage of this approach over conventional elemental mapping and image analysis is speed and ease of use.

Calibration graphs for chloride and sulphate in cement-based materials have been developed to enable quantitative analysis. This is done by analysing samples containing known amounts of chloride (or sulphate) and examining the strength of the

correlation between measured X-ray intensities and actual amounts. A strong linear correlation ($R^2 > 0.9$) is observed for a range of samples with a different w/c ratio, binder type, curing age, and drying condition. This is also observed when samples were analysed in a wet state (as-is) in ambient environment. These findings provide evidence that the measured characteristic X-ray intensities from μXRF and the observed correlations can be used for quantitative analysis of unknown samples.

Sample drying and moisture state has a major effect on the measured X-ray intensities. This was investigated to establish an appropriate preparation method for μXRF analysis of mass transport processes in cement-based materials. Rapid oven drying at 50°C distorts the measured chloride profiles. However, freeze-drying was able to preserve chloride profiles much better, producing identical chloride penetration depths to that measured before drying. Analysis on a flat ground surface provides more representative results than that on rough fractured surfaces. Finally, quantitative analysis of chloride and sulphate was demonstrated by combining the proposed dead time approach and calibration graphs. Results from μXRF are comparable to those from wet chemistry analysis (titration). The study also provides evidence that μXRF has sufficient sensitivity to detect changes in transport properties of samples with different binder types, water/binder ratio and drying conditions.

Acknowledgements

Thank you Allah for giving me the strength to successfully complete this PhD journey.

I would like to express my special appreciation and thanks to my supervisors Dr. Hong Wong and Professor Nick Buenfeld, who have been tremendous mentors for me throughout the duration of this study. I am very grateful for their guidance, support, advice, and trust in me throughout this challenging journey. I am grateful to Ministry of Education Malaysia in conjunction with Universiti Malaysia Perlis for sponsoring my tuition fees as well as the allowances through the Academic Training Scheme for Institutions of Higher Education (SLAI) scholarship.

I would also like to acknowledge the contribution of the following individuals, without which, the work presented here would not have been possible.

- My mum and dad for their love, encouragement, faith, and endless prayers;
- Nilla Olsson from Lund University, Sweden for provision of the mortar samples for Chapter 6;
- Mr. Andrew Morris for his dedicated assistance in the laboratory;
- Yi Won Ho for the collaboration work for Chapter 4 and François Marin-Cudraz for the collaboration work for Chapter 6;
- Andrew Lee from Edax Inc., Mahwah, New Jersey for the really useful and helpful training on the Orbis μXRF and Paul Wright from Edax UK for the advice and for troubleshooting the technical issues related to the Orbis μXRF;
- Department of Civil and Environmental Engineering staff for general assistance. I wish to express my thanks to Fionnuala Ni Dhonnabain in particular for her assistance and care;
- My colleagues at the Concrete Durability Group: Han, Zhigen, Sukina, Saeed, Marcus, Monika, Fadhilah, and Alalea for valuable suggestions and moral support;
- Universiti Teknikal Malaysia Melaka (Utem) for approving the unpaid leave for my husband so he can accompany me throughout this challenging PhD journey.

To my wonderful husband Mohd. Rashid and lovely children, Muhammad Raif Firas and Muhammad Rashad Faheem, thank you very much for your endless prayers, understanding, patience, unconditional love, support, encouragement, and cuddles and big bear hugs. You are one of my sources of strength and this work presented here is dedicated to you.

Notation

Roman letters

AAS	Atomic absorption spectroscopy
AES	Atomic emission spectroscopy
Al	Aluminium
Al_2O_3	Aluminium oxide
As_2O_3	Arsenic trioxide
c	Known concentration of an analyte
C_3A	Tricalcium aluminate
C_4AF	Tetracalcium aluminoferrite
Ca	Calcium
CaO	Calcium oxide
$Ca(OH)_2$	Calcium hydroxide
CEM I	Ordinary Portland cement
Cl^-	Chloride
CPS	Counts per second
Cr	Chromium
C_s	Concentration of diffusing species at the surface of the sample
C_2S	Dicalcium silicate
C_3S	Tricalcium silicate
C-S-H	Calcium silicate hydrates
Cu	Copper
$C(x,t)$	Concentration of diffusing species at distance x and time t
D	Diffusion coefficient
EDX/EDXRF	Energy dispersive X-ray spectroscopy
erf	Statistical error function
Fe	Iron
Fe_2O_3	Iron (III) oxide
FP	Fundamental parameters
ICP	Inductively coupled plasma

K	Potassium
KCl	Potassium chloride
keV	Kilo electron volt
K_2O	Potassium oxide
kV	Kilovolt
LIBS	Laser induced breakdown spectroscopy
LOD	Limit of detection
LOI	Loss on ignition
MgO	Magnesium oxide
Mn	Manganese
n	Number of analysed points
NaCl	Sodium chloride
Na_2O	Sodium oxide
Na_2SO_4	Sodium sulphate
OH^-	Hydroxide ion
OPC	Ordinary Portland cement
PFA	Pulverised fuel ash
ppm	Parts per million
RH	Relative humidity
ROI	Region of interest
rpm	rotations per minute
S	Sulphur
SCMs	Supplementary cementitious materials
S.E	Standard error
SEM	Scanning electron microscopy
SF	Silica fume
Si	Silicon
SiO_2	Silicon dioxide
SNR	Signal-to-noise ratio
SO_3	Sulphur trioxide
SO_3^{2-}	Sulphite ion
SO_4^{2-}	Sulphate ion
t	Time

Ti	Titanium
w/b	water-to-binder ratio
w/c	water-to-cement ratio
WDXRF	Wavelength dispersive X-ray spectrometry
x	Distance from the exposed surface
XRF	X-ray fluorescence

Greek letters

σ	Standard deviation
μXRF	Micro X-ray fluorescence

Contents

Declaration 2

Abstract 4

Acknowledgements 6

Notation 7

Contents 10

List of Tables 14

List of Figures 15

Chapter 1 Introduction 20

1.1 Research motivation 20

1.2 Objective and scope 21

1.3 Thesis outline 23

Chapter 2 Literature review 25

2.1 Chloride and sulphate attack in concrete structures 25

2.2 Transport of chloride and sulphate in concrete structures 26

2.2.1 Pore structure and moisture condition 26

2.2.2 Transport mechanisms 27

2.2.3 Pore solution and binding 30

2.3 Methods for elemental analysis 31

2.3.1 Titrimetry 32

2.3.2 Atomic spectroscopy 32

2.3.3 Scanning electron microscopy with energy dispersive X-ray spectroscopy (SEM-EDX) 35

2.4 X-ray fluorescence spectrometry (XRF) 36

2.4.1 Theory of X-ray fluorescence 36

2.4.2 Spurious peaks in XRF 38

2.4.3 Quantitative XRF analysis 39

2.5 Micro X-ray fluorescence (μXRF) 41
2.5.1 Beam voltage 43
2.5.2 Dead time 43
2.5.3 Analysis chamber 45
2.5.4 Filter 46
2.5.5 Acquisition time 48
2.5.6 Time constant 49
2.5.7 Beam spot size 49
2.6 Applications of μXRF in cement and concrete research and other fields 49
2.7 Summary 53
Chapter 3 Optimisation of μXRF for cement-based materials 55
3.1 Introduction 55
3.2 Methodology 56
3.2.1 Sample preparation 57
3.2.2 Freeze drying 58
3.2.3 Sample surface preparation 59
3.2.4 Data acquisition 60
3.2.5 Data analysis 60
3.3 Results and discussions 65
3.3.1 Beam voltage 65
3.3.2 Analysis chamber 68
3.3.3 Filter 70
3.3.4 Acquisition time 72
3.3.5 Time constant 74
3.3.6 Beam spot size 79
3.3.7 Dead time 81
3.3.8 LOD at optimum operating conditions 82

3.4 Conclusions 84
Chapter 4 Identification of cement paste and aggregate regions 88
4.1 Introduction 88
4.2 Elemental mapping 89
4.2.1 Acquisition of elemental maps 89
4.2.2 Parametric study 91
4.2.3 Composite element map via image analysis 95
4.2.4 Results 98
4.3 Dead time method 103
4.3.1 Background 103
4.3.2 Samples 104
4.3.3 Dead time measurements 105
4.3.4 Data analysis 106
4.3.5 Results 107
4.4 Comparison between elemental mapping and dead time method 119
4.4.1 Procedure 119
4.4.2 Results 120
4.5 Conclusions 122
Chapter 5 Calibration graphs for quantitative analysis of chlorine and sulphur 124
5.1 Introduction 124
5.2 Methodology 126
5.2.1 Samples containing admixed chloride 126
5.2.2 Samples containing admixed sulphate 127
5.2.3 Preparation for μXRF analysis 128
5.3 Results 129
5.3.1 General observations 129
5.3.2 Effect of w/c ratio 129

5.3.3 Effect of binder type 132
5.3.4 Effect of curing age 134
5.3.5 Effect of sample conditioning 136
5.4 Conclusions 139
Chapter 6 Transport of chloride and sulphate in cement based materials 141
6.1 Introduction 141
6.2 Parametric study 142
6.2.1 Methodology 143
6.2.2 Results and discussions 152
6.3 Study on chloride ingress in mortars using dead time approach 160
6.3.1 Methodology 160
6.3.2 Results and discussions 162
6.4 Study on sulphate ingress in concretes using dead time approach 164
6.4.1 Methodology 164
6.4.2 Results and discussions 168
6.5 Conclusions 170
Chapter 7 Conclusions and recommendations for further research 172
7.1 Main conclusions 172
7.2 Recommendations for further research 175
References 177

List of Tables

Table 3-1: Operating condition for the study on the effect of beam voltage. 65
Table 3-2: Optimum operating conditions for the analysis of chloride and sulphur. 86
Table 4-1: The μXRF measuring condition. 106
Table 5-1: Effect of drying condition on dead time achieved for samples from Series III. 139
Table 6-1: Oxide composition of the OPC and slag. 144
Table 6-2: Details on the location of the points. 148
Table 6-3: Details on the location of the points for M_{SF5}-0.380-50% RH. 149
Table 6-4: Operating condition for chloride profile determination. 151
Table 6-5: Operating condition for the study on chloride ingress using dead time approach. 162
Table 6-6: Oxide composition and LOI of the CEM I. 164
Table 6-7: Saturated surface dry (SSD) specific gravity, moisture content, and absorption of the aggregates. 165
Table 6-8: Mix proportion of the concrete. 165
Table 6-9: Operating condition for the study on sulphate ingress using dead time approach. 168

List of Figures

Figure 2-1: Schematic diagram of atomic emission. 33

Figure 2-2: Emission spectrum of (a) hydrogen and (b) iron. [Pogge, 2013] 33

Figure 2-3: Principle of atomic absorption spectrometry. 1: primary radiation source, 2: atomiser, 3: sample, 4: dispersive system, 5: detector, 6: data acquisition and processing, 7: data editing. 34

Figure 2-4: Basic structure of iron atom. 36

Figure 2-5: Stages in the emission of characteristic X-rays, (a) an atom in ground state, (b) an atom in ionised state, and (c) an atom emitting its characteristic X-rays. 37

Figure 2-6: Calibration curves for binaries illustrating matrix effects in XRF [de Vries & Vrebos, 2002]. 40

Figure 2-7: Schematic showing the main components of Orbis PC μXRF. 1: X-ray tube, 2: X-ray optics, 3: High magnification camera, 4: Low magnification camera, 5: Specimen, 6: XYZ motorised stage, 7: X-ray detector, 8: Detector signals, 9: Analyser. 42

Figure 2-8: Intensity of calcium K sum peak increases with increase in dead time. 44

Figure 2-9: Chloride K peaks measured in air and vacuum chamber. 45

Figure 2-10: Location of beam filter wheel [EDAX, 2010]. 46

Figure 2-11: Effect of different filters on the detection of arsenic trioxide [EDAX, 2010]. 47

Figure 2-12: Effect of acquisition time on the measured peaks for chlorine and potassium in KCl reference mineral standard. 48

Figure 3-1: Sample naming convention. 57

Figure 3-2: The main components of Lyotrap freeze dryer. 1: Stainless steel chamber, 2: Tiered sample holder, 3: Perspex cylindrical cover, 4: Round glass plate, 5: Vacuum pump 59

Figure 3-3: Setup for generating raw spectra in comma-separated value (CSV) file format, (a) Automation Setup dialog, and (b) Instrument Console 61

Figure 3-4: Background subtraction to obtain net counts for chloride peak. 63

Figure 3-5: Flow chart for background subtraction. 63

Figure 3-6: Effect of beam voltage on the (a) SNR and LOD for chloride, and (b) SNR and LOD for sulphur in P_{CEMI}-0.4-28d-0.50% Cl^-. 66

Figure 3-7: Effect of beam voltage on the intensity of bremsstrahlung radiation and visibility of elements at low energies. 68

Figure 3-8: Effect of analysis chamber on the (a) SNR for chloride, (b) LOD for chloride, (c) SNR for sulphur, and (d) LOD for sulphur in P_{CEMI}-0.4-3d-2.00% Cl^-. 69

Figure 3-9: Removal of Rh L peak using 25 μm Al filter to improve detection of chloride. 71

Figure 3-10: Effect of acquisition time on the (a) SNR and LOD for chloride, and (b) SNR and LOD for sulphur in P_{CEMI}-0.4-28d-0.15% Cl^-. 73

Figure 3-11: Effect of time constants 1.6, 3.2, 6.4, and 12.8 μs on the (a) SNR and LOD for chloride, and (b) SNR and LOD for sulphur in P_{CEMI}-0.4-28d-0.50% Cl^-.. 75

Figure 3-12: Effect of time constant (1.6 and 12.8 μs) on the resolution of elemental spectrum 76

Figure 3-13: Effect of time constants of 12.8, 25.6, 51.2, and 102.4 μs on the (a) SNR and LOD of chloride, and (b) SNR and LOD of sulphur in P_{CEMI}-0.4-28d-0.50% Cl^-. 78

Figure 3-14: Effect of beam spot size (30 μm, 2 mm) on the (a) SNR for chloride and sulphur, and (b) LOD for chloride and sulphur in P_{CEMI}-0.4-28d-0.50% Cl^-..... 79

Figure 3-15: Beam sizes available for μXRF analysis, (a) 30 μm, (b) 1 mm, and (c) 2 mm. Note that the 30 μm beam is too small to be shown on (a), thus the red spots are not to scale..... 81

Figure 3-16: SNR and LOD of chloride at optimum operating conditions in P_{CEMI}-0.4-28d-0.50% Cl^-. 82

Figure 3-17: SNR and LOD of sulphur at optimum operating conditions in P_{CEMI}-0.4-28d-0.50% Cl^-. 84

Figure 4-1: Randomly selected area of a concrete sample for parametric study (Field of view: 11.4mm×8.9mm). 91

Figure 4-2: Effect of beam spot size on the captured calcium map (a, b, c) and silicon map (d, e, f) of the concrete sample shown in Fig 4-1. 92

Figure 4-3: Effect of dwell time on the obtained calcium map for the concrete sample shown in Fig 4-1. 94

Figure 4-4: Example of manganese trace elemental map. 96

Figure 4-5: Flowchart demonstrating the steps to obtain the first composite image [Ho, 2013]. 97

Figure 4-6: Flowchart demonstrating the steps to obtain the second composite image [Ho, 2013]. 98

Figure 4-7: Concrete sample 1 with limestone coarse aggregates: (a) simple overlay approach using “merge channels” function, and (b) composite map approach using combination of key and trace element maps. Field of view = 95.11 mm × 42.72 mm. 99

Figure 4-8: Concrete sample 2 with Thames Valley aggregates: (a) simple overlay approach using “merge channels” function, and (b) composite map approach using combination of key and trace element maps. Field of view = 80.14 mm × 55.40 mm 100

Figure 4-9: Concrete sample 3 with Lytag lightweight aggregates: (a) simple overlay approach using “merge channels” function, and (b) composite map approach using combination of key and trace element maps. Field of view = 99.63 mm × 51.70 mm 102

Figure 4-10: Schematic showing input count rate (R_{in}), detector, and output count rate (R_{out}). 104

Figure 4-11: Examples of the analysed spots on pure paste samples. 108

Figure 4-12: Effect of (a) w/c ratio and (b) curing age on the dead time measured on neat cement pastes. 108

Figure 4-13: Examples of analysed paste matrix in concretes. 109

Figure 4-14: Dead times in neat pastes and paste regions in concretes at different (a) w/c ratio, and (b) curing age. 110

Figure 4-15: Image and the corresponding spectrum of (a) siliceous, (b) calcareous, and (c) ferrous aggregate..... 111

Figure 4-16: Effect of aggregate type on dead time and its corresponding intensity. 112

Figure 4-17: Effect of different regions of concrete on dead times and their corresponding intensities..... 115

Figure 4-18: Spectra of different regions of concrete. 116

Figure 4-19: (a) Interface 1-beam spot approximately 40 μm away from the aggregate, (b) Interface 2-the edge of the beam is just touching the cement paste-aggregate interface, and (c) Interface 3-beam spot is right on the interface..... 118

Figure 4-20: Regions selected for mapping on sample C_{CEMI}-0.40-7d (2.32mm×1.79mm). 119

Figure 4-21: Different phases in sample C_{CEMI}-0.40-7d. 120

Figure 4-22: Comparison between elemental mapping and dead time approach. ... 120

Figure 4-23: Schematic showing different phases of concrete based on dead time. 121

Figure 5-1: Correlation between measured characteristic X-ray intensity and actual chloride content for 28-day CEM I cement pastes at various w/c ratios. 131

Figure 5-2: Effect of cement type on the correlation between measured characteristic X-ray intensity and actual chloride content for 28-day cement pastes 133

Figure 6-1: The sample naming convention..... 143

Figure 6-2: Wet curing of the mortar samples [Personal communication with Nilla Olsson]. 145

Figure 6-3: The wick action test setup [Personal communication with Nilla Olsson]. 146

Figure 6-4: Examples of the selected points for analysis..... 147

Figure 6-5: Sample and point orientation. 148

Figure 6-6: Examples of the selected points for analysis for M_{SF5}-0.380-50% RH. 149

Figure 6-7: Distance between X-ray beam to the sample surface for M_{SF5}-0.380-50% RH. 150

Figure 6-8: Effect of binder type on chloride profiles of the mortars. 153

Figure 6-9: Effect of w/b ratio on chloride profiles for samples exposed to the drying environment of (a) 33% RH and (b) 75% RH. 154

Figure 6-10: Chloride profiles of before and after drying in oven at 50^0C for sample M_{SF5}-0.380-50%RH. 156

Figure 6-11: Chloride profiles of before and after freeze drying for samples (a) M_{OPC}-0.380-33%RH and (b) M_{Slag40}-0.386-33%RH. 157

Figure 6-12: Effect of sample grinding on the chloride profiles of M_{Slag70}-0.391-33%RH. 158

Figure 6-13: Schematic of rough (left) and ground surface (right) [Marin-Cudraz, 2015]. 159

Figure 6-14: Analysed surface of sample M_{OPC}-0.380-33% RH (a) as-is and (b) ground with silicon carbide paper of grit size 120. 159

Figure 6-15: Examples of the selected points for analysis on M_{OPC}-0.380-33% RH (Replicate). 161

Figure 6-16: Chloride profiles determined by µXRF and wet chemistry. 163

Figure 6-17: Sulphate penetration test setup. 166

Figure 6-18: Examples of the selected points for analysis. 167

Figure 6-19: Sulphate profile of the sample exposed to 5% Na_2SO_4 solution for 35 days 169

Chapter 1 Introduction

1.1 Research motivation

All of the major physicochemical deterioration mechanisms that affect the durability of concrete structures require water and transport of aggressive species into concrete. For example, ingress of chloride initiates the corrosion of embedded steel in reinforced concrete, which is the primary cause of degradation of reinforced concrete structures worldwide [Klinghoffer et al., 2000]. Corrosion of reinforcement eventually leads to cracking and spalling of the cover, reduction of steel cross-section and loss of load bearing capacity. Ingress of sulphates causes deleterious reactions with the hardened cement paste that result in expansion, cracking and loss of cohesiveness of the concrete [Mehta & Monteiro, 2006].

As such, investigations of concrete degradation often require testing to detect the presence of aggressive species, measure their amount and rate of penetration into concrete. The obtained information is used to establish the cause, rate and severity of the degradation, to formulate the appropriate rehabilitation strategy and possibly to predict remaining service-life [Buenfeld & Wong, 2011]. It is also of great importance to better understand the transport of aggressive species in order to develop more durable concretes and approaches to mitigate deterioration processes.

There are several methods available for measuring chlorides and sulphates in concrete. However, all existing methods have limitations. An inter-laboratory investigation undertaken by the Concrete Society [Barnes & Ingham, 2013] showed that the conventional acid extraction and titration methods described in BS 1881-124 [1988] for determining chloride and sulphate content in hardened concrete are low in accuracy and precision. Chloride content was overestimated while sulphate content showed a large scatter. The study concluded that these methods do not provide sufficiently accurate results to judge whether or not the tested samples would be within allowable limits [Barnes & Ingham, 2013]. The inaccurate results may be caused by poor sample preparation [Barnes & Ingham, 2013/2014]. Other studies have also suggested that the profile grinding and nitric acid extraction for chloride analysis is prone to sample

preparation errors and may not dissolve all chloride from powdered samples [Dhir et al., 1990; Wall & Nillson, 2008].

Bulk X-ray fluorescence uses a large X-ray beam (millimetres to centimetres in dimension) and this limits its spatial resolution. The integration of scanning electron microscopy (SEM) with energy dispersive X-ray spectroscopy (EDX) produces a powerful analytical tool for characterising the microstructure and elemental composition at the micrometre scale. However, the SEM-EDX method requires samples to be dried, polished and subjected to high vacuum condition. These processes may cause damages or alter the distribution of the mobile species under investigation. Although SEM-EDX has very high spatial resolution, it is a time-consuming and laborious to analyse large samples. As such, it is not a practical routine method for characterising transport in bulk concrete.

Micro X-ray fluorescence (μXRF) is a relatively new technique that is able to perform spot analysis, line scan and mapping of elements at high spatial resolution compared to conventional methods [Müller, 2004]. It is similar to SEM-EDX but has several distinct advantages including requiring little sample preparation, no sample pre-drying and no vacuum chamber so that measurements can be made in ambient environment. It is also able to analyse large samples in a relatively short period of time. These features of μXRF lend itself a huge potential for the study of transport mechanisms in concrete such as chloride and sulphate ingress. However, very little research has been carried out so far to develop, optimise and exploit this technique for cement and concrete research.

1.2 Objective and scope

The overall research aim is to develop, optimise and exploit μXRF for characterising concrete and for studying transport of chloride and sulphate in concrete. The sub-objectives are as follows:

i. Optimise μXRF for analysis of chloride and sulphate in concrete. This will be achieved by investigating the effects of operating condition and sample preparation on the sensitivity of μXRF to chloride and sulphate analyses;

ii. Develop μXRF for identifying the cement paste and aggregate regions in hardened concrete. The ability to do this is important since chloride and sulphate penetrate concrete mainly through the porous cement paste matrix. In addition, aggregates may contain naturally occurring chloride. Therefore, the inclusion of aggregates in μXRF analysis may lead to potential errors in the determination of chloride ingress;

iii. Develop μXRF for studying the penetration of chloride and sulphate in concrete, and for measuring their transport coefficients. Calibration graphs will be developed to enable conversion of measured X-ray intensities of chloride and sulphate to mass concentration. This is necessary to check, for example, whether the chloride concentration exceeds the threshold value for corrosion initiation. The new approach for identifying cement paste and aggregate regions together with the calibration graphs will be applied for quantitative analysis of chloride and sulphate.

μXRF has several advantages over existing techniques. For example, its ability to map element distribution in an ambient environment means that the risk of sample alteration due to drying or exposure to strong vacuum is reduced. It is also able to analyse large samples at high spatial resolution in a relatively short period of time. Therefore, the potential benefit arising from a successful outcome of this research is an improved ability to detect the presence of aggressive species, measure their amount and rate of penetration. This will open up new possibilities for studying mass transport mechanisms which is an important aspect in characterising long-term durability of concrete structures**.**

1.3 Thesis outline

The thesis consists of seven chapters. Chapter 1 introduces the research background and objectives and scope of the study. Chapter 2 presents the literature review on the topics related to the scope of this thesis. Chapters 3, 4, 5, and 6 present the experimental work and main findings of this research. The methodology of the experimental work which includes materials, sample preparation, and testing is described under each of these four results chapters.

Chapter 3 presents the results on the optimisation of μXRF operating parameters for analysis of chloride and sulphate in concrete. The results are reported in the form of signal-to-noise ratio (SNR) and its corresponding limit of detection (LOD). The operating parameters under study were beam voltage, analysis chamber, filter, acquisition time, time constant, beam spot size, and dead time. The results showed that the SNR of both chloride and sulphur were greater at higher beam voltages and longer acquisition times. The SNR of both ions were also greater when the analyses were executed in vacuum chamber and using the 30 μm beam size. The application of the 25 μm aluminium filter is a requisite for chloride analysis, but not necessary for sulphur analysis. Dead time of 30-50% and time constant of 12.8 μs are recommended for optimised results.

Chapter 4 presents a new approach for identifying cement paste regions in mortars and concretes. The method is based on the observed changes in dead time when a 30 μm beam samples cement paste or aggregate regions. The paste regions identified using this approach was compared to those identified by conventional elemental mapping. This Chapter also investigates the effect of four operating parameters on the quality of elemental maps. The operating parameters were beam spot size, beam voltage, time constant, and dwell time. The beam spot size of 30 μm was superior to 1 or 2 mm in terms of producing sharp elemental maps. Beam voltage and time constant had insignificant effects, but there was a slight improvement in the clarity of calcium and silicon maps at higher dwell times.

Chapter 5 presents the development of calibrations graphs by analysing pure cement paste standards containing known amounts of admixed chloride or sulphate. The function of the calibrations standards is to convert the measured chloride and sulphur intensities in the form of counts per second into chloride and sulphur percent by mass of cement. The effects of drying, w/c ratio, curing age, and cement type on the calibration graphs are discussed.

Chapter 6 demonstrates the application of the dead time approach proposed in Chapter 4 and calibration graphs developed in Chapter 5 on concrete or mortar samples exposed to sodium chloride (NaCl) and sodium sulphate (Na_2SO_4) solutions. The study also included the effects of grinding and drying on the measured chloride and sulphur profiles.

Finally, the main findings from this thesis are summarised in Chapter 7. Recommendations for further research are also presented.

Chapter 2 Literature review

This Chapter presents a literature review on the topics relevant to the scope of this thesis.

2.1 Chloride and sulphate attack in concrete structures

Chloride is one of the major aggressive species to reinforced concrete structures. This is because when it is present in sufficient quantities exceeding a threshold level at the reinforcing steel, it destroys the self-generated protective passive oxide layer and initiates corrosion of reinforcement bars. The propagation of corrosion and formation of corrosion products will eventually lead to cracking and spalling of the concrete cover [Zhao et al., 2011; Wong et al., 2010]. Chloride threshold level for corrosion initiation is most commonly expressed as total chloride content by weight of cement or concrete. Some of the reported threshold levels expressed as total chloride content by weight of cement ranged between 0.4 and 1.6% [Hansson & Sorensen, 1990], 0.5 and 2.0% [Schiessl & Raupach, 1990], and 1.6 and 2.5% [Lambert et al., 1991].

Threshold values have also been expressed as free chloride content per weight of cement, or concrete, or as concentration in the pore solution. Free chloride is normally expressed as a function of the hydroxyl concentration in the pore solution in the form of chloride to hydroxyl concentration ratio. Cl^-/OH^- values of 0.6 [Hausmann, 1967], 0.3 [Diamond, 1986], and 0.25-0.80 [Goni & Andrade, 1990] have been suggested for use in practice. Free chloride refers to the mobile chloride ions in pore solution while bound chloride refers to chloride ions bound to cement hydration products through adsorption or chemical binding in the form of Friedel's salt. Hence, total chloride content refers to the sum of both free and bound chloride in a sample. Chloride threshold level is best expressed as the total chloride content by mass of cement since bound chloride may be released under some circumstances to participate in corrosion [Glass & Buenfeld, 1997; Castellote & Andrade, 2001]. An extensive review on the critical chloride content for corrosion initiation of reinforced concrete can be found in Angst et al. [2009].

The mechanism of sulphate attack can be divided into chemical and physical attack [Skalny et al., 2002; Neville, 2004]. Chemical and physical sulphate attack can occur simultaneously in one specimen [Nehdi et al., 2014; Whittaker & Black, 2015]. Chemical sulphate attack is also referred to as "classical" sulphate attack [Mehta, 2000]. Essentially, this involves the reaction between sulphate ions from an external source and cement hydration products leading to expansion and cracking of concrete due to the formation of ettringite and gypsum. The formation of gypsum also causes a reduction of pH of the system as well as loss in stiffness and strength of concrete [Mehta & Monteiro, 2006]. An internal form of chemical sulphate attack can also occur when the source of sulphate is from within the concrete, for example when a cement of unusually high sulphate content is used in concrete production. Physical sulphate attack refers to the damage caused by salt crystallisation. In this research, we will use the term sulphate attack to refer to chemical sulphate attack only.

2.2 Transport of chloride and sulphate in concrete structures

The kinetics of transport of aggressive ions depend on the pore structure, moisture condition of concrete, the transport mechanisms involved, and on the interactions (i.e. binding) between the transported ions with the cement hydration products. Since a particular focus of this research is on mass transport in concrete, these influencing factors are briefly reviewed in the subsequent sections.

2.2.1 Pore structure and moisture condition

The main compounds of Portland cement are tricalcium silicate (C_3S), dicalcium silicate (C_2S), tricalcium aluminate (C_3A), and tetracalcium aluminoferrite (C_4AF). During the hydration of cement, C_3S and C_2S react with water to form calcium silicate hydrates (C-S-H) and calcium hydroxide ($Ca(OH)_2$), which are the main hydration products that act as the binder in concrete [Richardson et al., 2010]. Capillary pores and gel pores are two distinct types of pores in the hydrated cement paste that influence transport. Capillary pores which are about 1 μm in dimension are the residual space within the hardened paste that are not filled with hydration products. In contrast, gel pores are approximately 2 nm in dimension and these are located within the solid hydration products. Hollow-shell voids or also known as "Hadley grains" sometimes form within the original boundary of reacting cement particles [Head et al., 2006].

Concrete may also contain entrained air voids typically 0.1 mm in diameter, entrapped air voids of up to several millimetres in diameter, as well as other voids that include internal cracks, voids under aggregate particles created by trapped bleed water, and 'honeycomb' voids [Buenfeld et al., 1998]. The interface between cement paste and aggregate particles, i.e. the "interfacial-transition zone" (ITZ) is also of particular interest because this zone inherently containing higher amount of porosity and lower amount of cement particles [Ollivier et al., 1995; Scrivener et al., 2004; Wong & Buenfeld., 2006b]

The rate of any transport mechanism relies on the volume fraction, tortuosity, and connectivity of the pore structure and any cracks that exist in the microstructure. These factors are influenced by parameters such as water/cement ratio, cement content, cement type, use of supplementary cementitious materials and aggregate type and content [Hooton 1986; H. Abdul Razak et al., 2004; Lothenbach et al., 2011; Dehghanpoor Abyaneh et al., 2013]. Mass transport properties are also significantly influenced by moisture content and degree of saturation of the pores [Houst et al., 1994; Abbas et al., 1999; Wong et al., 2007]. When the capillary porosity is low, entrained and entrapped air voids are isolated from one another and thus have little influence on transport in concrete. If these voids are empty, they facilitate gaseous transport but will block the movement of ions [Wong et al., 2011]. A continuous network of cracks and other large voids will significantly increase the transport of water and aggressive species into concrete [Lee et al., 2010, 2016; Wu et al., 2014; Dehghanpoor Abyaneh et al. 2016]. In the absence of continuous cracks and other large voids, the transport of deleterious species will be dominated by interconnected capillary pores [Ngala et al., 1995].

2.2.2 Transport mechanisms

The ingress of chloride and sulphate ions into concrete can occur through transport mechanisms such as diffusion, capillary suction and permeation. These transport mechanisms might occur individually or simultaneously. Permeation refers to transport under a pressure gradient, but this is rarely a driving force of fluids entering concrete [Neville, 2011] and is often assumed negligible for most concrete structures in typical exposure environments [Maage et al., 1994]. Diffusion is the transport of

ions via a concentration gradient in saturated condition, and this alone can be a very slow process. In unsaturated concrete, the dominant transport mechanism is capillary suction [Martys & Ferraris, 1997]. In comparison to other mechanisms, transport via capillary suction occurs at the fastest rate [Maage et al., 1994; Dehghanpoor et al., 2014]. Wick action is another type of transport mechanisms and is defined as the transport of water (and various ions that it may contain) through a concrete element from a side in contact with water to a drying side [Buenfeld et al., 1995]. Wick action is a major transport mechanism that occur in structures such as tunnels and basements, and this will be reviewed in detail in Chapter 6. Diffusion and capillary suction are further explained in the subsequent sections.

2.2.2.1 **Diffusion**

In the presence of concentration gradient between the external environment of concrete such as seawater and the internal concrete environment, the mechanism of transport of aggressive species into and through concrete would be by means of diffusion. Ionic diffusion will be more effective in saturated pores than in partially saturated pores. Marine structures that are fully submerged will be saturated and therefore pure diffusion governs the transport of deleterious ions such as chloride into concrete. The diffusion process can be measured under steady state or non-steady state conditions.

Fick's first law of diffusion describes the steady state process and this is shown in Equation 2-1. This is only applicable if the flux entering the system equals to the flux exiting the system. In practice, it may require a very long time to reach a steady state condition in concrete structures.

$$F = -D\frac{dC}{dx} \qquad \textbf{Eq. 2-1}$$

where:

F = flux (kg/m^2.s)

C = concentration of diffusing species present at distance x from the exposed surface (kg/m^3)

D = diffusion coefficient (m^2/s)

In non-steady state conditions, the flux varies with time and this process is governed by Fick's second law which is shown in Equation 2-2.

$$\frac{\partial C}{\partial t} = D\frac{\partial^2 C}{\partial x^2} \qquad \textbf{Eq. 2-2}$$

This equation is normally integrated based on some assumptions and the solution is shown in Equation 2-3.

$$\frac{C(x,t)}{C_s} = 1 - \text{erf}(\frac{x}{2\sqrt{Dt}}) \qquad \textbf{Eq. 2-3}$$

where:

$C(x,t)$ = Concentration of diffusing species at distance x and time t

C_s = concentration of diffusing species at the surface of the sample

erf = statistical error function

x = distance from the exposed surface

D = diffusion coefficient

t = time

2.2.2.2 **Capillary suction**

Water in contact with partially saturated concrete will be absorbed by capillary action. Capillary absorption increases with increase in porosity and with decrease in moisture content. Measurement of capillary absorption in concrete is normally carried out via a sorptivity test. In this test, the dried sample is placed in contact with water in a manner such that only 2 to 5 mm of the sample is submerged. The mass of water absorbed is measured over time by weighing. The rate of capillary suction (i.e. sorptivity coefficient) can be obtained from the slope of the best-fit line of the absorbed water vs. square-root time plot using Equation 2-4.

$$A = C + St^{1/2} \qquad \textbf{Eq. 2-4}$$

where:

A = mass of water absorbed per unit cross-sectional area

C = y-axis intercept due to surface effects at the start of the experiment

S = sorptivity coefficient

t = time

2.2.3 Pore solution and binding

Water in hardened cement paste exists as one of three forms: combined water, gel water, and capillary water [Neville & Brooks, 2010]. Combined water is the water that is chemically or physically combined with the hydration products. Gel water is held to the hydration products either as adsorbed water that is held by surface forces of gel particles or as interlayer water held between the layers of hydration products. Capillary water is the water contained in the capillary pores. Capillary pores can be empty, partially saturated or filled with water, depending on the quantity of the original mix water, curing and exposure conditions. The water in the hydrated cement paste is also called the pore solution.

As a consequence of cement hydration, the pore solution contains a high concentration of several dissolved ions. The major cations are sodium (Na^+), potassium (K^+), and calcium (Ca^{2+}) and the major anions are hydroxyl (OH^-) and sulphate (SO_4^{2-}). Na^+ and K^+ originate from alkali oxide in the cement such as Na_2O and K_2O while SO_4^{2-} come mainly from gypsum added during cement production, contaminated aggregates, or mixing water. The concentration of these ions depends on the chemical composition of cement, w/c ratio, use of supplementary cementitious materials, degree of hydration, and moisture content [Buenfeld et al., 1998].

The principle of electroneutrality requires that the sum of positive and negative charges within matter must balance to zero. This means that the transport of excess ions such as chloride (Cl^-) in one direction may only occur if other ions of the same charge such as OH^- are transported in the opposite direction [Yu et al., 1993]. For example, during the diffusion of sodium chloride (NaCl) into concrete, the transport of chloride ions into concrete via pore solution will become increasingly more difficult due to the build of positive charge Na^+ in the source unless a significant counter-diffusion of OH^- or SO_4^{2-} ions occurs. Therefore the type and concentration of ionic species in the pore solution affect the kinetics of transport in concrete.

Another factor that affects the rate of ionic transport is binding. This occurs due to interactions between the porous cement paste matrix and diffusing species leading to the reduction and removal of the mobile species from the pore solution. For example, all cements has the capacity to bind a proportion of chloride present. Binding removes free chloride from the transport process and alters the concentration of the pore solution, hence the concentration gradient that drives diffusion. The degree of chloride binding relies on cement type, composition of pore solution, and the external environment. The net effect of chloride binding is the slowing down of the rate of chloride penetration into concrete exposed to an external chloride source [Sergi et al., 1992].

2.3 Methods for elemental analysis

Elemental analysis can be qualitative or quantitative. Qualitative analysis refers to the process of identifying the elements present in a sample while quantitative analysis allows the amount of the elements present to be determined. The emphasis of this research is on quantitative analysis since this is vital for characterising the transport of deleterious species into concrete. As an example, the determination of chloride concentration distribution in concrete is important for modelling the time to reinforcement corrosion and service life of concrete structures in marine environment. The different techniques used to quantify chloride and sulphate content in concrete are reviewed in this section.

2.3.1 Titrimetry

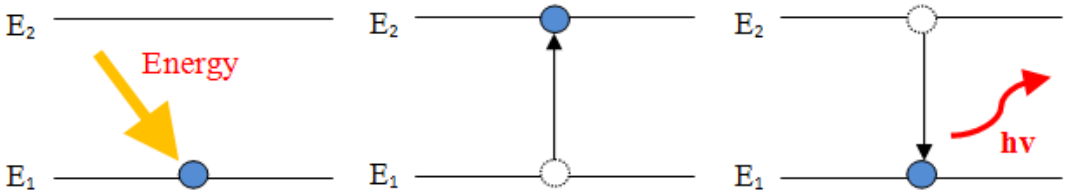
Titrimetry refers to quantitative chemical analysis used to determine the concentration of an analyte by volumetric or gravimetric measurements. Volumetric titrimetry is based on measuring the volume of a solution of known concentration needed to react completely with the analyte. This is by far the most widely-used method [Skoog, West, & Holler, 1994]. Gravimetric titrimetry is based on weighing the mass of precipitates that are formed in the reaction between the analyte and a precipitating agent. From the mass and known stoichiometry, the concentration of the analyte can be determined. This method is very accurate due to the fact that it is feasible to weigh substances to high accuracy with analytical balances [Kellner, 1998]. The sample needs to be in solution for both methods and therefore, titrimetry are destructive methods. Furthermore, these methods are time consuming and require laborious sample preparation. Measurements are carried out on bulk samples and the spatial resolution is relatively low. The determination of chloride or sulphate content in concrete is usually associated with profile grinding, which is specified in NT Build 443 [1995], NT Build 208 [1996], ASTM C1556 [2011], ASTM C1152/C1152M [2012] and BS 1881-124 [1988].

2.3.2 Atomic spectroscopy

Atomic spectroscopy is a technique for determining the concentration of an analyte by observing its electromagnetic spectrum. Atomic emission and absorption spectroscopy are two analytical methods in atomic spectroscopy.

2.3.2.1 **Atomic emission spectroscopy (AES)**

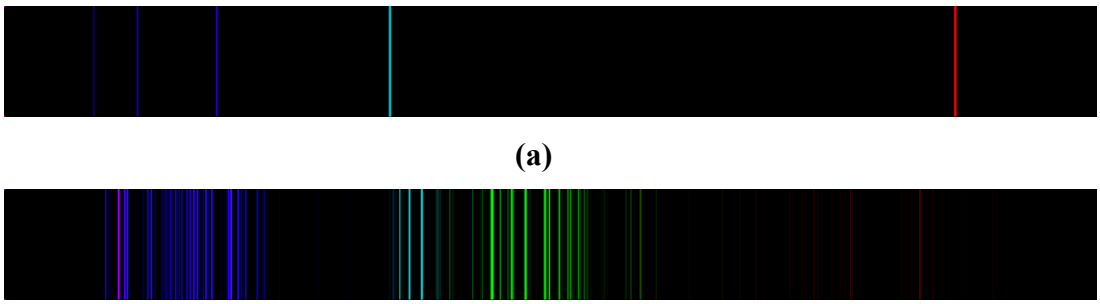
AES is probably one of the oldest methods employed for elemental analysis. The principle behind AES is based on the Bohr's atomic model (Section 2.4.1). Electrons are bounded to the nucleus by a specific amount of energy which in turn depends on the location of the shells and sub-shells. This specific amount of energy is called the electron binding energy. The closer the electrons to the nucleus, the higher the binding energy and vice versa.



(a) **(b)** **(c)**

Figure 2-1: Schematic diagram of atomic emission.

Figure 2-1 (a) shows an electron of an atom in its ground state. E_1 and E_2 are the atomic shells each possessing different energy values. If sufficient amount of energy is imposed on the atom, the electron gets excited to higher energy orbital as shown in Figure 2-1 (b). The electron will then fall back from the excited state to ground state and simultaneously releasing energy as illustrated in Figure 2-1 (c). The wavelength or frequency of the emitted photon is equal to the difference in energy between the two states. AES is based on the detection of the emitted light when elements transition from an excited state to the ground state. The energy of the emitted light is specific to the element and therefore, the type and amount of the element present can be determined by means of a spectrometer. Figure 2-2 shows the emission spectrum of hydrogen and iron.



(a)

(b)

Figure 2-2: Emission spectrum of (a) hydrogen and (b) iron. [Pogge, 2013]

In AES, a radiation source is used to atomise the sample in order to release free atoms and to excite the atoms to higher energy states. Flame spectrometry is primarily used for the determination of alkali and alkaline earth elements [Mermet, 1998] which are exclusive of sulphur and chloride. In contrast, inductively coupled plasma (ICP) – AES [Philips, 2008; Mermet, 1998] has the ability to measure most of the elements in the

periodic table. However, these techniques are bulk analysis methods and require the sample to be in solution form.

Laser induced breakdown spectroscopy (LIBS) is another example of the AES technique [Anabitarte et al., 2012]. In LIBS, an intense laser pulse is focused on the sample to create a plasma which is then analysed using spectroscopy. Previous LIBS systems were seen as overly complicated, limited in spectral coverage, bulky and expensive [Kearton & Mattley, 2008]. Due to advancement in technology, current LIBS system is highly sensitive, fast, and requires minimal sample preparation. In cement and concrete research, the feasibility of using LIBS to measure chloride content and sulphate content in cement based materials has been studied and demonstrated by several authors including Wilsch et al., 2005; Šavija et al., 2014; Gondal et al., 2009; Labutin et al., 2013 and by Weritz et al., 2005; Weritz et al., 2009.

2.3.2.2 **Atomic absorption spectroscopy (AAS)**

In contrast to AES, AAS is based on the absorption of radiation by atoms in a sample of interest when exposed to a primary radiation source such as hollow cathode lamp (HCL) and electrodeless discharge lamp (EDL). Figure 2-3 shows a schematic diagram of AAS. The primary source emits specific radiations while the function of the atomiser is to convert the sample into free atoms. Commonly employed atomisers are flame and electro-thermal atomisers (furnace). The atomised elements from the sample absorb the primary radiation with wavelength equal to that of the element line. The acquired data is processed to determine the wavelength and amount of absorbed radiation, which is proportional to the concentration of the element.

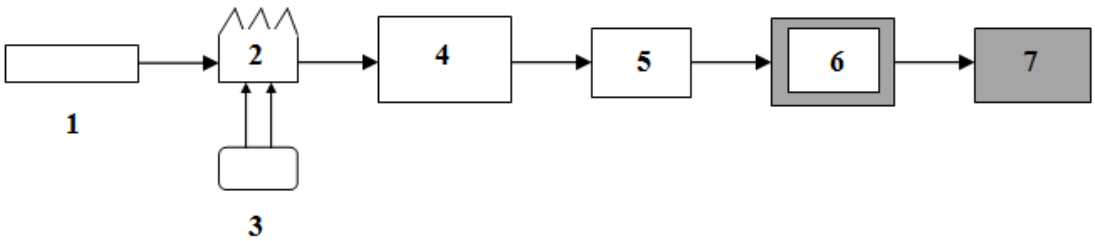


Figure 2-3: Principle of atomic absorption spectrometry. 1: primary radiation source, 2: atomiser, 3: sample, 4: dispersive system, 5: detector, 6: data acquisition and processing, 7: data editing.

Flame AAS is normally used to analyse liquid or dissolved samples, while electro-thermal AAS may be used to analyse liquid, solid, and gaseous samples. AAS is highly element specific technique and this can be a disadvantage when analysing complex mixtures containing many elements. For example, several hollow cathode lamps each with a different pure metal as the hollow cathode are required for multi-element analysis.

2.3.3 Scanning electron microscopy with energy dispersive X-ray spectroscopy (SEM-EDX)

SEM-EDX employs a high energy electron beam with accelerating voltages between 5 and 30 keV [NORAN Instruments, 1999] to impinge the sample. The interactions between the electron beam and sample produce several signals such as secondary electrons, backscattered electrons, and characteristic X-rays that emerged at depths of several microns from the sample surface. The depth of signal interaction volume depends mainly on the composition and accelerating voltage applied [Wong et al. 2006c, Yio et al., 2016]. These signals are detected and processed to form either an image or a spectrum that contains microstructural information. Secondary electrons are those with energies below 50 eV that escape from near the sample surface and these provide topographic information. Backscattered electrons have energies greater than 50 eV, emerge from a greater depth and provide information about the composition of the sample. The energies of characteristic X-rays correlate to the type and amount of elements present in the sample. The main disadvantages of SEM-EDX are the need for samples to be dried, epoxy impregnated, flat polished, and analysed under a high vacuum condition. Non-conductive specimens must also be coated since they tend to charge when scanned by the electron beams. Furthermore, only a very small volume of the sample is analysed at each spot therefore a large number of analysis is required to obtain sufficient and representative data at the scale of concrete.

2.4 X-ray fluorescence spectrometry (XRF)

XRF is based on the production and detection of characteristic X-rays emitted by elements in the sample when they are irradiated with a primary beam of X-ray. The acquired characteristic X-rays are processed to obtain information concerning the type and quantity of the elements present. Two methods of measuring characteristic X-rays are the wavelength dispersive X-ray spectrometry (WDXRF) and the energy dispersive X-ray spectrometry (EDXRF). The latter approach was employed throughout this research.

2.4.1 Theory of X-ray fluorescence

According to Bohr's model, an atom consists of dense nucleus made of protons and neutrons at its centre and surrounded by clouds of negatively charged electrons located in their orbitals, also referred to as levels or shells. These levels are designated by the letters K, L, M, N and so on as they become farther away from the nucleus. The principal quantum number is n = 1 for K shell electrons, n = 2 for L shell electrons and so on. The K shell is a single shell without sub-levels or sub-shells, while the L shell consists of three sub-shells (L_1, L_2, and L_3), the M shell consists of five sub-shells (M_1 to M_5) and the N shell consists of seven sub-shells (N_1 to N_7) [Lachance & Claisse, 1995]. For example, Figure 2-4 shows a schematic of the iron atom (atomic number 26) based on Bohr's model.

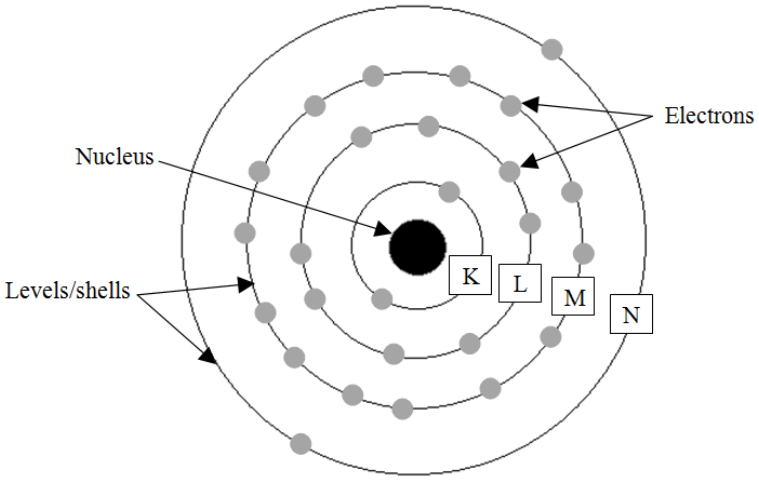


Figure 2-4: Basic structure of iron atom.

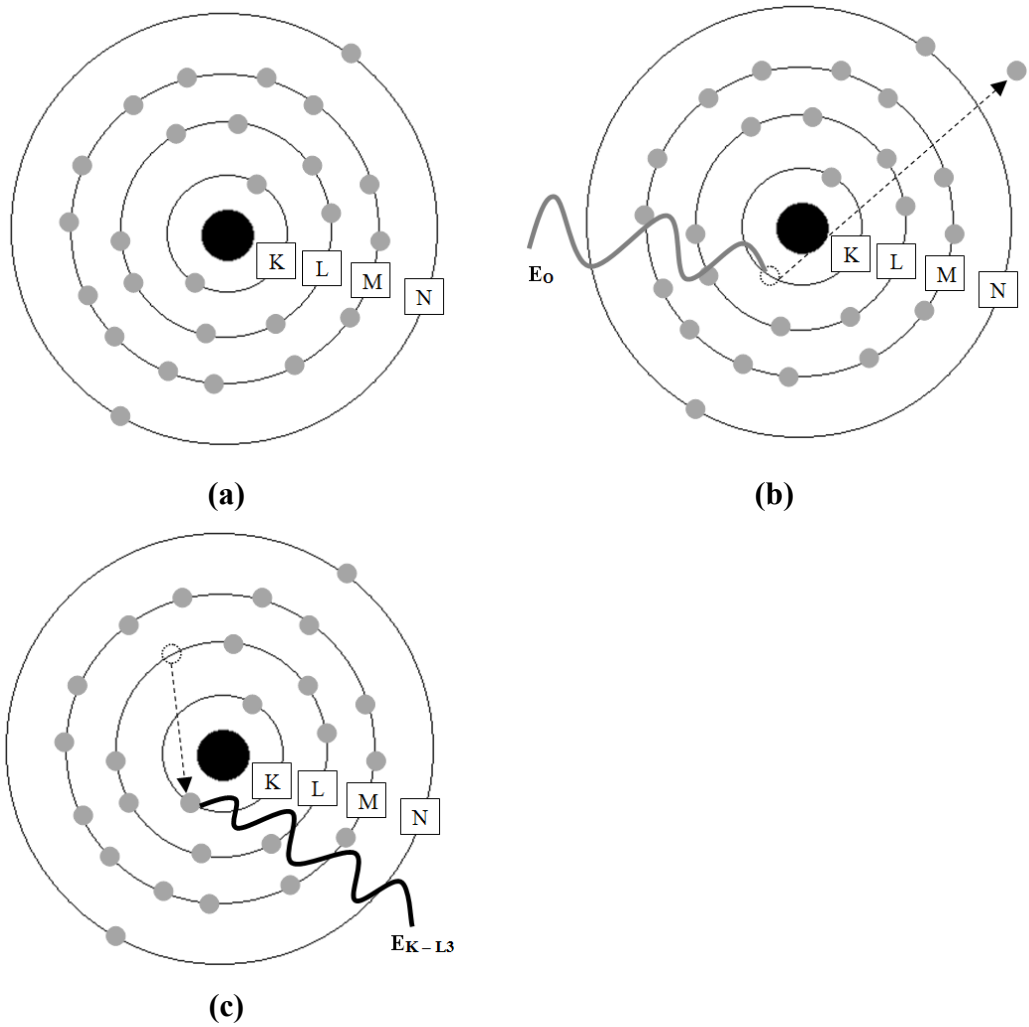


Figure 2-5: Stages in the emission of characteristic X-rays, (a) an atom in ground state, (b) an atom in ionised state, and (c) an atom emitting its characteristic X-rays.

Figure 2-5 shows the stages involved in the emission of characteristic X-rays. When the atom is in its ground state (Figure 2-5a), each electron is bound to the nucleus by a specific amount of energy which is dependent on the location of its shell and sub-shell. The closer the electrons to the nucleus, the higher the binding energy. The binding energies of electrons for each shell and sub-shell for most elements are known and available elsewhere, e.g. Poole [n.d.]. If the sample is irradiated by incoming X-ray of energy E_O that is equal to or higher than the binding energy of, for example an electron in the K shell, the electron will be ejected from the atom leaving it in an ionised or excited state (Figure 2-5b). An atom in ionised state is unstable and electrons from higher shell level will fill in the vacancy created by the ejected electron. For example, if a K shell electron is ejected, the vacancy will be filled by an electron from one of the L, M, or N sub-shells. Each transition constitutes an energy loss resulting

in emission of characteristic X-ray with energy equal to the difference between the energy levels involved. As shown in Figure 2-5(c), an electron from L_3 sub-shell fills the vacancy created in the K shell leading to the emission of K – L_3 characteristic X-ray (corresponding to $K_{\alpha 1}$ in Siegbahn notation). In EDXRF, the energies of the detected characteristic X-ray are measured and shown in a spectrum that indicates the type and amount of elements present.

2.4.2 Spurious peaks in XRF

There are several artefact peaks that might be present in the XRF spectrum in addition to the elemental peaks. These include the sum and escape peaks which are two false peaks originating from the detection process, and the Rayleigh and Compton scatter, which are false peaks arising from the X-ray tube source.

Sum peak occurs when two characteristic X-ray photons arrive simultaneously at the detector such that these cannot be recognised as two separate events. This creates a new peak that has an energy equal to the sum of the two X-ray energies. Sum peaks can be formed by photons from the same element or photons from different elements [GlobalSino, 2013]. Escape peak arises because the detector is made of silicon that will ionise and fluoresce when the incoming characteristic X-ray photon from the sample has an energy greater than the silicon binding energy (1.74 keV). As a result, the characteristic X-ray photon from the sample loses some energy in ionising the silicon atom. The result is an escape peak in the spectrum with energy of 1.74 keV less than the original characteristic X-ray.

Rayleigh scatter takes place when incoming photons impinge on the X-ray tube target material which in this case is rhodium, causing the electrons to oscillate and emit X-rays at the same frequency as the incident photon. In XRF spectra of cement-based materials, the Rayleigh scattered peaks can be easily identified and removed due to the fact that the presence of rhodium in cement pastes, mortars, or concretes is uncommon. Both Rayleigh Rh K and Rh L peaks will occur in the spectrum if the incoming X-ray energy is equal to or greater than the K edge energy of rhodium which is 23.229 keV. However, Rayleigh Rh L is known to obscure the Cl K peak in the absence of filter during XRF analyses and this needs careful consideration. Compton scatter occurs

when incoming photon collides with a loosely bound outer electron. In this process, the electron recoils from the impact and leaves the atom by carrying a portion of the energy of the incoming photon. As a result, the scattered photon changes direction as it loses its energy. In a spectrum where the X-ray tube target material is rhodium, Compton scattered peak is observed as broad rhodium peak on the lower energy side of each coherently scattered peak [Lachance & Claisse, 1995].

2.4.3 Quantitative XRF analysis

Quantitative analysis refers to the conversion of measured intensities of characteristic X-rays to mass or concentration values. The intensity is equal to the area of a peak in EDXRF or the height of a peak in WDXRF. In order to ensure that the net intensity used for quantitative analysis emanates from the element of interest only, the background spectrum and peak overlaps must be subtracted from the raw spectrum. The background subtraction method employed throughout this research is explained in detail in Chapter 3. The basic procedure for quantitative analysis is to calibrate the spectrometer by measuring one or more reference material of known composition. A calibration graph is then produced which shows a relationship between the measured intensity of a particular characteristic line and the concentration of the corresponding element in the reference material. The calibration graph is then used to determine the composition of the element of interest in unknown samples.

As a result of matrix effects, net intensities measured in XRF are not always linearly related to actual concentration [Lachance, 1993] except in thin samples where matrix effects can be neglected [Markowicz, 2011]. Intensity does not only depend on concentration of the originating element but also on the presence and concentration of other elements in the sample [PANalytical, 2006; Espen, 1998]. This is known as the inter-element or matrix effects, which consist of absorption and enhancement effects. Incoming X-rays penetrate the sample and a portion of which is absorbed by layers of atoms above those of the element of interest. Characteristic X-rays emitted by the ionised atoms must also pass these overlying atoms in order to escape the sample, during which a part of the fluorescence is absorbed. The absorption effect relies on which elements are present and their concentrations. Generally, heavy elements absorb more than light elements.

The emission of characteristic X-rays is not only caused by the primary X-ray beam, but also by characteristic fluorescence X-rays of other atoms. Characteristic X-rays generated by the primary beam is denoted as primary fluorescence. If the primary fluorescence has sufficiently high energy, it can ionise other atoms, induce secondary fluorescence and thus, the observed X-ray intensity will be higher than expected [Espen, 1998]. This is known as the enhancement effect. Figure 2-6 shows how matrix effects can influence the calibration curve of binary systems, i.e. samples with only two elements or compounds. Curve 1 in Figure 2-6 shows an ideal linear relationship between relative intensity and weight fraction (no matrix effects). Curve 2 and 3 indicate positive and negative absorption respectively, while Curve 4 shows the effect of enhancement on the calibration graph.

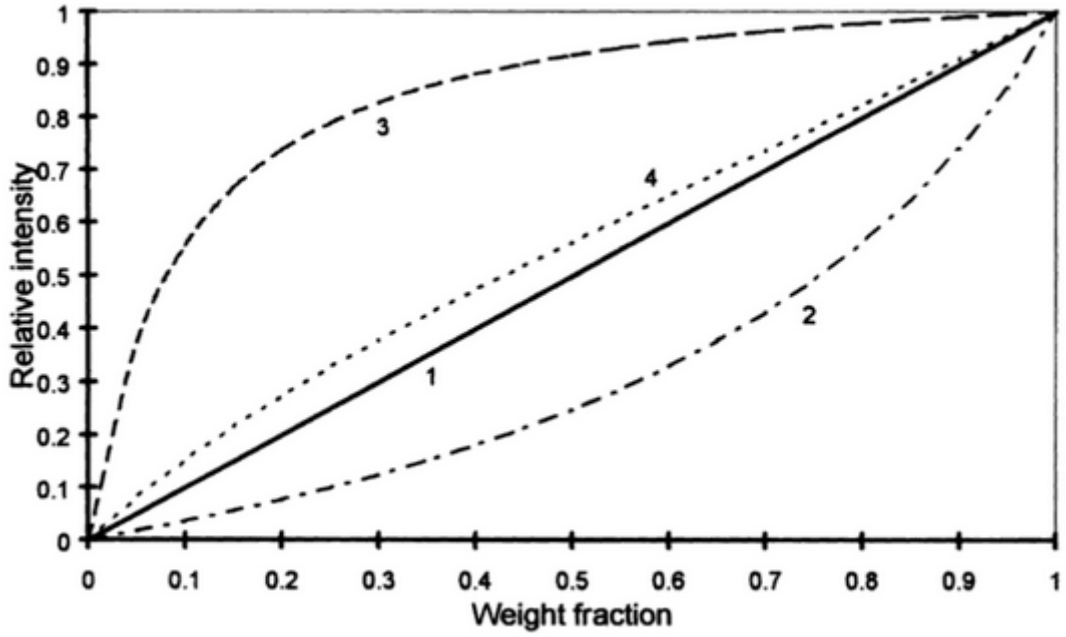


Figure 2-6: Calibration curves for binaries illustrating matrix effects in XRF [de Vries & Vrebos, 2002].

Since the early fifties, many approaches have been proposed to correct matrix effects [Rousseau, 2001]. Two popular methods are the influence coefficients method and fundamental parameters (FP) method [Criss & Birks, 1968]. Influence coefficients are mathematical expressions that quantify the matrix effects of a particular element and their combined net effect in a single value [Lachance, 1993]. These coefficients can be obtained from empirical relationships or theoretical calculations. In contrast, FP is a fully theoretical quantification method which consists of calibration and iteration

steps. Calibration involves calculating intensities relative to that of pure element or multi-component specimen of known composition. Iteration involves the conversion of the calculated relative intensities into concentration. The main limitation of this approach is the need to estimate the composition of each element present in a sample in order to start the iteration procedure and to normalise the concentrations prior to each iteration. The latter generates inaccurate data if light elements are present, which may occur in cement-based materials.

Due to time constraints, no attempt was made in this research to develop a protocol for correcting matrix effects. However, one of the main focus of this thesis was on understanding the effect of sample parameters on the calibration graphs. The parameters that will be studied include w/c ratio, cement type, curing age and sample moisture content (Chapter 5). The obtained calibration graphs were then used to convert chloride and sulphate net intensities into their concentration expressed as percent by mass of cement.

2.5 Micro X-ray fluorescence (μXRF)

μXRF shares the same working principle as conventional X-ray fluorescence as explained in Sections 2.4.1, 2.4.2, and 2.4.3. The primary difference is the X-ray beam spot size. XRF is regarded as a bulk analysis technique since the primary beam has dimensions of millimetres to centimetres [Davis et al., 2009] and this limits its spatial resolution. In contrast, μXRF employs a monolithic poly-capillary optics to focus the X-ray beam to a 30 μm spot size or a collimating X-ray optics to convert a highly divergent beam of X-rays into 1 mm and 2 mm beam size.

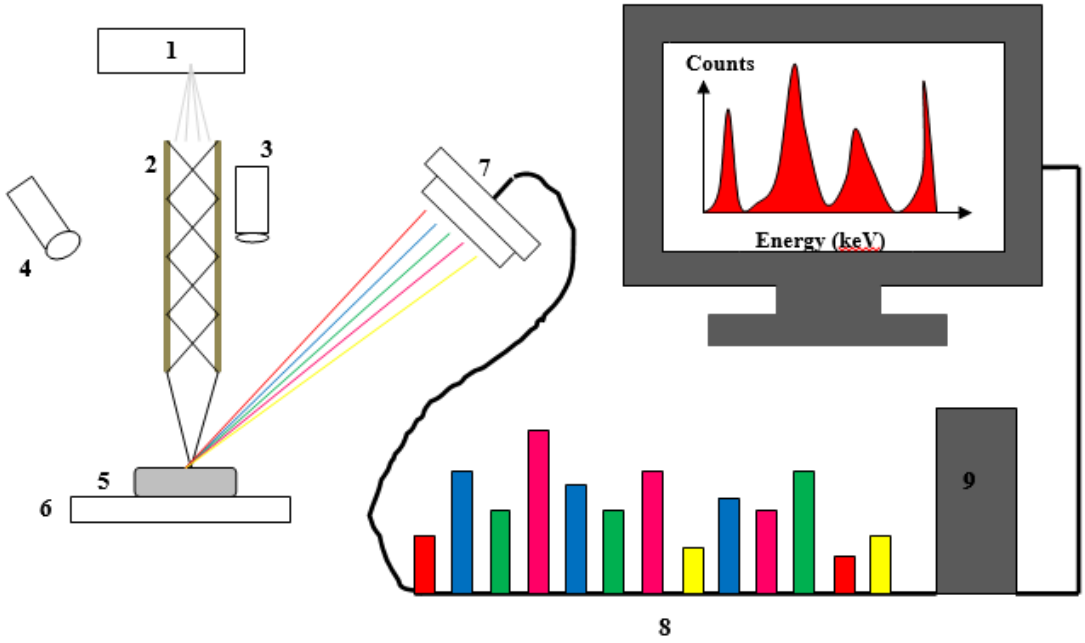


Figure 2-7: Schematic showing the main components of Orbis PC µXRF. 1: X-ray tube, 2: X-ray optics, 3: High magnification camera, 4: Low magnification camera, 5: Specimen, 6: XYZ motorised stage, 7: X-ray detector, 8: Detector signals, 9: Analyser.

Figure 2-7 shows the main components of the Orbis PC µXRF (manufactured by Edax Ametek). This is the main equipment that will be used in this research. Primary X-rays are generated in the X-ray tube which uses rhodium as the target anode. The system is equipped with one high magnification camera (70×) located perpendicular to sample surface and one low magnification camera (10×) located at an angle to sample surface. The motorised stage can be controlled to move in the XYZ directions. The system can analyse irregular shaped samples and fractured surfaces. The largest sample size that can be analysed is 270×270×100 mm. Characteristic X-rays emitted by the sample are detected by a silicon lithium, Si(Li) detector.

In µXRF, there are at least seven operating parameters that might affect quantitative analysis. The parameters are beam voltage, dead time, analysis chamber, filter, acquisition time, time constant, and beam spot size. These parameters are further explained in subsequent sections. Beam current, which is the amount of electrons liberated by the tungsten filament and accelerated towards rhodium target material, also plays an important role. In Chapter 3 for example, beam current was adjusted to

achieve comparable sets of operating condition in order to optimise the μXRF for cement-based materials.

2.5.1 Beam voltage

Beam accelerating voltage is the amount of energy applied to accelerate electrons released by tungsten filament on the cathode side to a high velocity beam that impinges the Rh target on anode side to produce X-rays. The generated X-rays consist of a continuous spectrum (bremsstrahlung radiation) and characteristic X-rays of rhodium. A high beam voltage produces a high energy primary X-ray beam which can then excite and detect heavy elements present in the test sample. For example, a beam voltage of 10 kV can only produce the emission of K characteristic X-rays for elements up to zinc (atomic number 30). If elements heavier than zinc are present, only the less intense characteristic X-ray lines such as the L lines will be emitted. At a higher beam voltage of 20 kV, the K characteristic X-rays of elements up to niobium (atomic number 41) will be emitted. The K characteristic X-rays are commonly the first choice for elements with atomic number lower than 50 because they are more intense compared to the L or M characteristic X-rays [Lachance & Claisse, 1995]. For μXRF, the minimum and maximum beam voltage applicable are typically 10 kV and 50 kV respectively.

2.5.2 Dead time

Dead time of a detector relates to the minimum time interval that two consecutive counts must be separated in order to be recorded as two different events [Bécares & Blázquez, 2012]. Within this time interval, detector will not accept the next incoming photon because the pulse processor is processing the one that has arrived earlier. Dead time between 30 – 50% is deemed acceptable [EDAX, 2009] and exceeding this range produces an artificial pile up or sum peak. For example, Figure 2-8 shows the presence of a calcium K sum peak for a calcareous aggregate in a concrete sample measured at different dead times. The intensity of the sum peak increases with increase in dead time. For this example, beam current, beam spot size, acquisition time, and time constant was 105 μA, 30 μm, 100 s Live, and 12.8 μs respectively. No filter was applied and the analyses were carried out in vacuum.

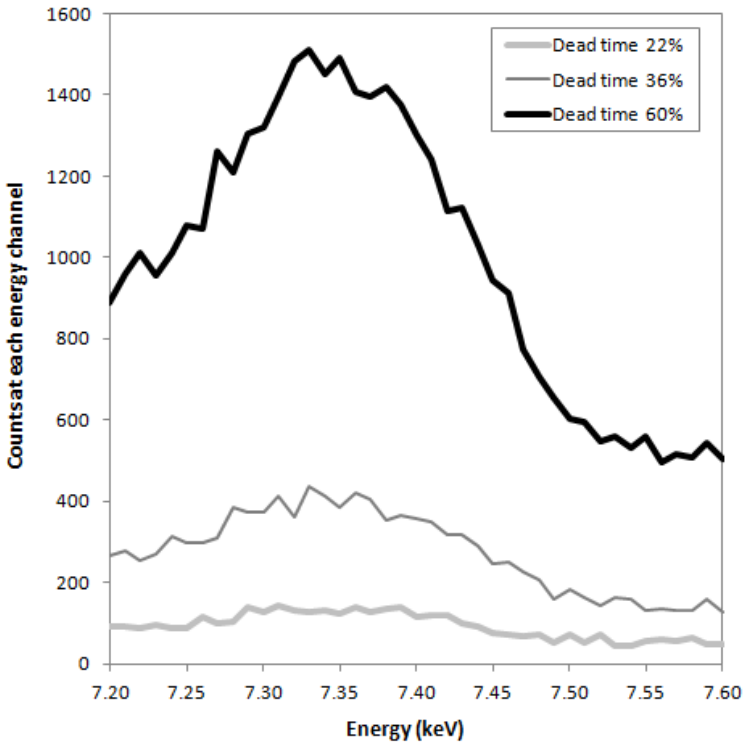


Figure 2-8: Intensity of calcium K sum peak increases with increase in dead time.

The energy of the sum peak formed could either be the summation of two calcium $K_{\alpha 1}$ energies or two calcium $K_{\alpha 2}$ energies. It could also be the summation of calcium $K_{\alpha 1}$ and $K_{\alpha 2}$ energies. In all cases, the combined energy is approximately 7.38 keV as shown in Figure 2-8. Fortunately, the sum peak does not interfere with the sulphate peak (2.22-2.40 keV) and chloride peak (2.53-2.71 keV). Therefore, correcting this artefact is a relatively straightforward procedure.

2.5.3 Analysis chamber

With µXRF, samples can be analysed either in air (ambient) or vacuum environment. The pressure in the vacuum chamber is ~ 0.40 Torr. The main advantage of conducting the analysis in air is that the sample would not require pre-drying, which may be damaging or may influence the distribution of elements of interest. However, the presence of air molecules in the chamber could cause the absorption of fluorescence radiations from light elements, particular sulphur and below [Streli et al., 2003]. Figure 2-9 shows an example of chloride peaks measured from a potassium chloride (KCl) reference standard in air and vacuum. Here, the beam voltage was 11 kV and beam current was adjusted to achieve 30% dead time in both cases. The time constant, beam spot size, and acquisition time was 25.6 µs, 30 µm, and 100 s Live respectively. A 25 µm aluminium filter was also employed. The results highlight the feasibility of conducting chloride analysis in an ambient environment. However, a small decrease in the Cl Kα peak was observed compared to the case when the analysis was conducted in vacuum.

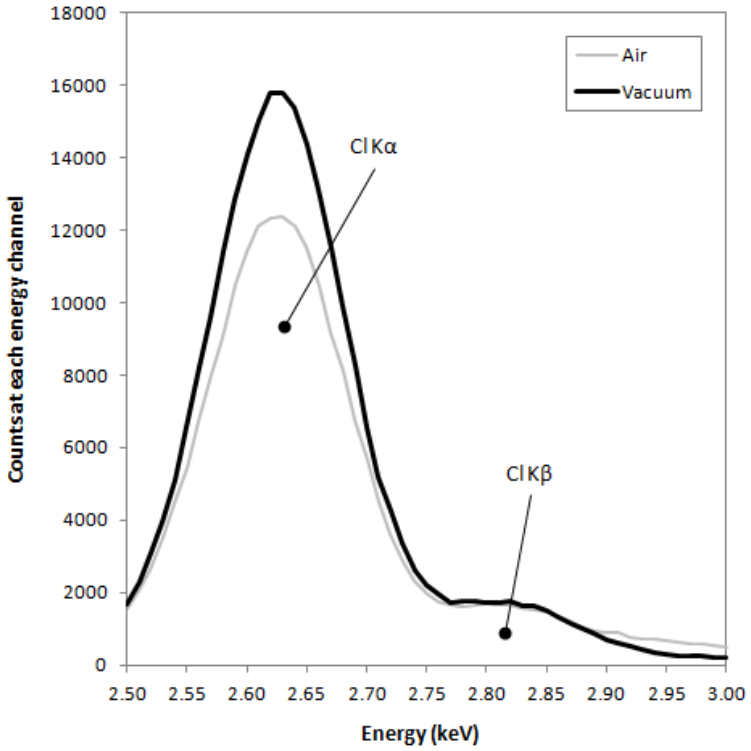


Figure 2-9: Chloride K peaks measured in air and vacuum chamber.

2.5.4 Filter

The filter is a thin foil located right beneath the X-ray tube and before the X-ray focusing optic. There are six selection of filters for the µXRF system used in this study, namely the 25 µm and 250 µm aluminium filter, 25 µm titanium filter, 25 µm nickel filter, 100 µm rhodium filter, and 127 µm niobium filter. The relative location of filter wheel is shown in Figure 2-10.

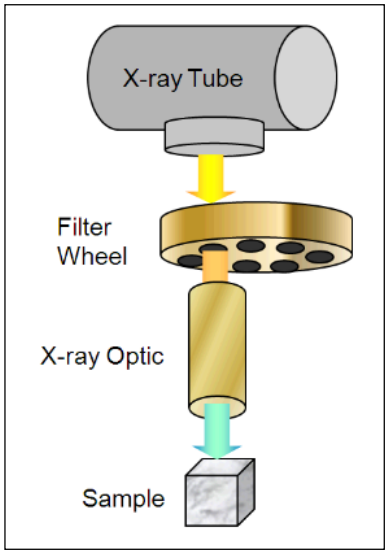


Figure 2-10: Location of beam filter wheel [EDAX, 2010].

Each filter is designed to improve the detection limit of certain elemental range by absorbing bremsstrahlung X-rays as well as some spurious X-ray peaks. As an example, nickel filter will improve the detection limit of zinc, gallium, germanium, and arsenic [EDAX, 2010] since the K characteristic fluorescence energy of each of these elements lies within the bremsstrahlung energy range that will be cleared by the filter. Figure 2-11 shows the effect of different filter condition on the limit of detection (in parts per million) of arsenic trioxide (As_2O_3). In this example, the red spectrum was acquired without the use of filter. The green spectrum was obtained with nickel filter while the blue spectrum was obtained from analysis with thick aluminium filter. As seen in the figure, the limit of detection for As_2O_3 improves with the presence of filter. This is due to the removal of bremsstrahlung radiation which then increases the signal-to-noise ratio for the element of interest.

The application of a filter is possible relevant to this study because an appropriate filter could improve the detection of chloride or sulphate. For example, the K absorption edge for aluminium, titanium, nickel, niobium, and rhodium is 1.562 keV, 4.965 keV, 8.339 keV, 18.985 keV, and 23.229 keV respectively. Based on these values, the 25 µm thick aluminium filter might be an appropriate filter to absorb and remove the Rh L Rayleigh scatter peak from obscuring the Cl K peak. However, the 250 µm aluminium filter might be too thick for this purpose. This will be further studied and discussed in Chapter 3.

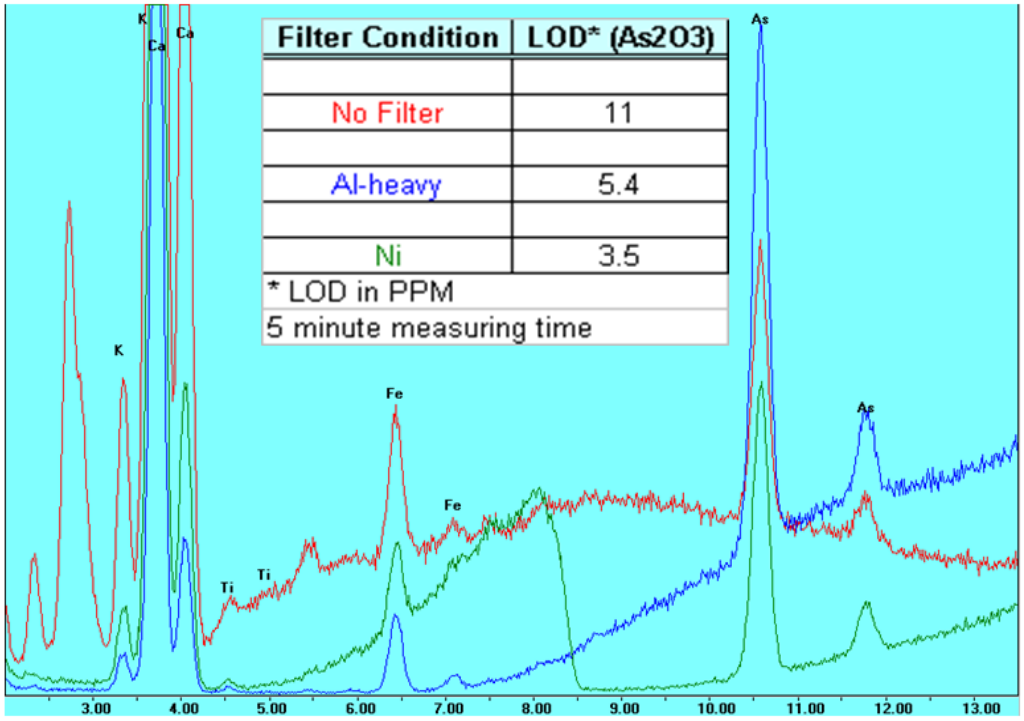


Figure 2-11: Effect of different filters on the detection of arsenic trioxide [EDAX, 2010].

2.5.5 Acquisition time

Acquisition time is the time allocated for collection of characteristic X-ray photons at each analysed spot. Acquisition time can be measured either in clock time or live time. Clock time is the sum of live time and dead time of the detector. Live time is the time when detector is able to receive X-ray photons emitted from the sample, while dead time is a time when detector is "switched off" and unable to accept incoming photons (Section 2.5.2). Generally, a longer acquisition time will produce a cleaner spectrum and a more statistically representative data [EDAX, 2009]. It also improves signal-to-noise ratio and the detection of minor element peaks. An example illustrating the benefit of longer acquisition time is shown in Figure 2-12 for a KCl reference mineral standard. For this example, the beam voltage, time constant, and beam spot size used was 11 kV, 25.6 µs, and 30 µm, respectively. The analyses were carried out in air chamber with the application of 25 µm aluminium filter. Beam current was adjusted to 795 µA to reach dead time of 30%.

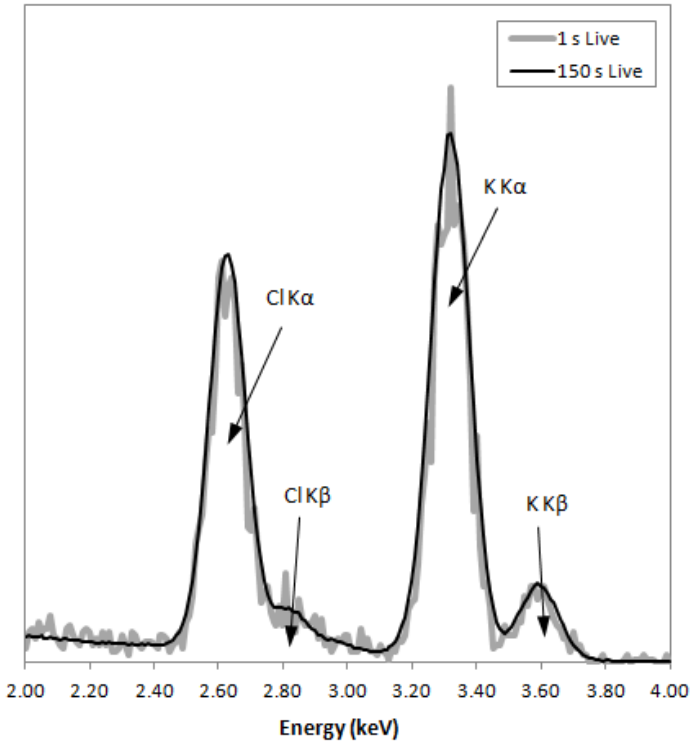


Figure 2-12: Effect of acquisition time on the measured peaks for chlorine and potassium in KCl reference mineral standard.

2.5.6 Time constant

Time constant is the amount of time taken by the detector to process each photon that goes into the detector. This is an important parameter that influences the resolution of the measured spectra. The time constants available with the Orbis μXRF are 1.6, 3.2, 6.4, 12.8, 25.6, 51.2, and 102.4 μs. At short time constants, there is a probability that incoming photons would not be processed accurately, are assigned to less accurate energy channels and hence degrading the resolution of the generated spectrum. In contrast, at longer time constants, the photons would be processed more accurately and thus assigned to the correct energy channels hence improving the resolution of the spectrum produced.

2.5.7 Beam spot size

X-rays exiting the X-ray tube will diverge in all directions as the beam intensities decrease between the tube and sample. The focusing X-ray optics which is placed underneath the X-ray tube window will collect and guide X-rays down to three user-selectable spot sizes which are 1 and 2 mm aperture/collimator and 30 μm poly-capillary. As shown in Figure 2-9, the X-ray optics is positioned underneath the filter wheel which is located below the X-ray tube. The choice of beam spot size will depend on the required spatial resolution and area of the sample to be analysed. For example, using a larger beam spot size facilitates the analyses of large surface areas, but achieves a lower spatial resolution. The effect of beam spot size on elemental spot analysis and mapping of cement-based materials will be investigated in Chapter 3 and 4 respectively.

2.6 Applications of μXRF in cement and concrete research and other fields

μXRF is a relatively new technique for cement and concrete research. Example applications are reviewed here. Davis et al. [2009] used μXRF to measure the intrusion of potassium ion from de-icing salt into concrete. Commercial grade de-icing solution (50% wt. potassium acetate or potassium formate) was applied on the top surface of concrete samples for 3 months at Clemson, USA and 6 months at Weimar, Germany. The concretes were then cored and sectioned for analysis. The size of the Clemson and Weimar sample was 30 mm × 35 mm and 30 mm × 100 mm respectively. Quantitative

analysis was carried out via the fundamental parameter approach with a series of NIST glasses used as empirical standards to minimise matrix corrections. These standards were chosen to provide reference intensities for aluminium, silicon, potassium, calcium, and iron. Analysis was carried out in vacuum using the same set of operating conditions for both standards and specimens. The beam voltage used was 20 kV and beam current was adjusted to reach 30% dead time. Results showed that potassium ions penetrated approximately 15 mm into Clemson sample and the entire length of Weimar sample.

Schlegel et al. [2011] employed μXRF elemental mapping to study changes in phase composition due to sulphate ingress in cement paste. To simulate sulphate attack, four cement paste samples were submerged in sodium sulphate solution (3%) for 3 and 6 months. Based on the observed colour gradient in the element maps, each sample was categorised into three distinct areas. The first area was a region with the highest sulphur concentration which represents secondary phase formation. The second area was a region with lower sulphur concentration which represents the penetration depth of the sulphate solution. The third area was intact bulk cement paste.

Davis et al. [2011] presented a brief case study on the ability of μXRF to perform large area X-ray mapping of heterogeneous sample. A mortar cylinder was submerged in solution composed of potassium chloride (87% wt.) and sodium chloride (13% wt.) for over two months. The sample was then split along the centre line and mapped using μXRF. The authors reported higher chloride and potassium concentrations at the surface exposed to salt solution based on colour gradient of the obtained maps. Sutter et al. [2009] presented an approach to perform chloride profiling by means of μXRF. This was based on locating the analysis points in the paste matrix of mortar sample with the aid of silicon, chloride, and calcium maps. The operating conditions were presented, however there was little discussion on why these were used.

Snyder et al. [2012] studied the effectiveness of three viscosity modifiers to increase viscosity of pore solution and thereby reduce the effective chloride diffusivity in mortars. The viscosity modifiers examined were polyoxyalkylene alkyl ether, polypropylene glycol, and high-molecular mass cellulose ether. Mortar cylinders (100 mm diameter, 1250 mm height) were cast and cured until the age of 28 days. At the

end of curing, samples were submerged in 1-mol/L sodium chloride solution for 24 and 52 weeks. After each exposure period, two mortar cylinders were removed, towel dried, and split longitudinally for μXRF analysis. Chloride analysis was carried out in air chamber to avoid samples drying out in vacuum which might affect results. A 25 μm aluminium filter was employed to remove Rh Lα Rayleigh scatter from overlapping with the chloride peak. The output from μXRF analysis in the form of chloride counts was used to calculate effective diffusivity. The results showed that using viscosity modifiers can reduce chloride diffusivity of concrete.

Müller and Rübner [2006] investigated the effects and performance of municipal solid waste incinerator (MSWI) bottom ash as aggregates in concretes. The bottom ash used consisted of 80% mineral components, 15% bottle glass as well as metals and ceramics, and 2% organic residues. The aim was to study the interactions between the bottom ash aggregate and the cement paste matrix. Three reactions were observed: alkali-silica reaction, formation of aluminium hydroxide and calcium aluminate hydrate, and formation of ettringite and monosulphate from the reaction between aluminate and calcium sulphate. μXRF was employed to map the qualitative distribution of silicon, potassium, and calcium in the concrete samples. However, the μXRF operating condition was not presented. The potassium map of samples exposed to 40^0C and 99.9% RH for 9 months found one sample exhibited an alkali-silica reaction induced crack caused by a large agglomeration of bottle glass fragments fused with steel and other ash compounds.

The feasibility of μXRF for characterising iron sulphides in aggregates was studied by Chinchón-Payá et al. [2013]. Sulphides in aggregates can oxidise in the presence of water to form sulphates and subsequently react with cement hydrations products to form gypsum, ettringite, and thaumasite which causes expansion and cracking of concrete. Concrete cores with aggregates containing iron sulphides were sectioned with diamond saw for μXRF analysis. The analysis was carried out at 10 kV beam voltage and 200 ms dwell time, but no other details were given in particular the quantification method employed. The obtained sulphur and iron maps were overlapped to form a composite image to detect iron sulphides. This composite map was then binarised and further processed using image analysis to quantify the iron sulphides present.

Ho [2013] applied μXRF elemental mapping to quantify the volume fractions of coarse aggregates, fine aggregates, and cement paste matrix for various types of concrete. A parametric study was first carried out to generate good quality elemental maps. Then, an image analysis based method was developed to quantify the volume fractions of different phases in concrete. Elemental maps were generated using optimised operating condition and these were combined to produce a composite image that highlights the phase of interest. Artefacts on the composite image were evaluated and removed. The volume fractions of coarse aggregates, fine aggregates, and paste matrix were calculated based on the area fraction of these phases measured on the composite image using ImageJ. The results obtained by the proposed method were found to be in close agreement to the original mix design and point counting analysis. In another study carried out at the Concrete Durability Group, Imperial College London, Alzyoud et al. [2014, 2016] applied μXRF to study the effect of reinforcement spacers on the ingress of chloride in reinforced concrete. The main advantage of the technique is the speed and ease by which the chloride profiles were obtained compared to other conventional methods e.g. profile grinding and titration.

In other fields such as forensic science, Worley et al. [2006] demonstrated the feasibility of using μXRF for mapping fingerprints that are undetectable by conventional contrast methods. These include fingerprints on challenging substrates such as fibrous papers, textiles, and woods. Fingerprints of prepubescent children as well as fingerprints present on dark or multi-coloured backgrounds can also be difficult to detect by conventional methods. Worley et al. [2006] analysed several types of sebaceous fingerprints such as fingerprints produced after perspiring, applying lotion and saliva, touching the moist interior of a banana and fingerprint on a black paper after applying hand sunscreen. Fingerprints after perspiring were detected in the potassium and chlorine maps while those made after applying saliva were detected from the potassium, chlorine, and phosphorus maps. Latent fingerprints made on a black paper was detected from the titanium map, which indicates the presence of this element in the applied sunscreen.

In archaeology, μXRF has been used, among others, to distinguish Chinese ancient porcelains from fake artefacts [Cheng et al., 2007]. In this study, pieces of Chinese ancient Ru porcelain and Jun porcelain (AD 960-1276) as well as a piece of fake Jun porcelain were analysed. The beam voltage and beam current used was 35 kV and 10 mA respectively. The spectrum showed that the fake Jun porcelain contained higher Ti, Ba, Cu, and Zn and lower Mn and Fe in comparison to that of the ancient Jun porcelain. Elements such as Ba and Zn are crucial in the process of distinguishing ancient porcelains from fake artefacts.

In the field of preservation and restoration of paper records and books, μXRF has been employed in tandem with other techniques to study foxing stains on paper [Bicchieri et al., 2002]. Foxing spots appear on paper as stains of reddish-brown, brown or yellowish colour, generally of small dimensions. Some authors found evidence of bacterial and fungal growth in foxed areas sometimes associated with the presence of iron. In this study, foxing was induced on paper by treatment with small amounts of iron solutions where the iron ions are present in the form of iron (II) and iron (III). After artificial aging, a 350 μm beam spot was used to analyse both the paper and the artificially produced foxing stains. The results show the Fe/Ar ratio increased on foxing stains compared to the unstained paper. The presence of argon was due to the measurements made in ambient environment. The study concluded that μXRF is a useful technique for determining paper composition and the type of degradation mechanism, which is important because these influence the choice of restoration method. For example, deacidification is necessary if the paper contains iron.

2.7 Summary

Chloride-induced reinforcement corrosion and sulphate attack are two major deterioration mechanisms affecting the long-term durability of concrete structures worldwide. A crucial aspect in concrete durability research is the ability to measure the amount, spatial distribution and transport rates of these deleterious species in concrete. The most commonly used methods include titrimetry, atomic spectroscopy, SEM-EDX, and bulk XRF. μXRF is a relatively new and promising technique that has several distinct advantages over conventional methods. However, it is evident from the reviewed literature that little research has been carried out thus far to optimise and

exploit this technique for quantitative analysis of chloride and sulphate in concrete. There are at least seven operating parameters that might affect μXRF analysis and unresolved issues concerning the best approach to convert measured X-ray intensities to mass concentration. For example, the approach based on calibration standards is expected to be influenced by various parameters such as w/c ratio, cement type, moisture content and curing age. Therefore, a major focus of this thesis is to contribute towards understanding the effects of operating and sample parameters on chloride and sulphate analysis in cement based materials.

Chapter 3 Optimisation of μXRF for cement-based materials

This Chapter investigates the effects of seven main operating conditions in μXRF on its sensitivity for chloride and sulphate analysis in cement-based materials. The aim is to understand factors influencing the accuracy of μXRF and to determine its optimum operating conditions. Paste samples with water/cement ratio of 0.4 and chloride content of 0.15%, 0.50%, and 2.00% by mass of cement were employed. Results are reported in the form of signal-to-noise ratio (SNR) and its corresponding limit of detection (LOD). It was found that the SNR for both chloride and sulphur improved at higher beam voltages and longer acquisition times. A higher SNR was also obtained when the analysis was executed in a vacuum chamber using the 30 μm beam spot size. Application of the 25 μm aluminium filter is a requisite for chloride analysis in order to remove overlapping spurious peak from the rhodium target layer in the X-ray tube. However, this filter is not necessary if the element of interest is sulphur. A dead time of 30 – 50% and an amplifier time constant of 12.8 μs are recommended to obtain an optimised set-up. At the optimum operating condition, the LOD for chloride is 0.007% by mass of cement (70 ppm) at 6000 s live acquisition time and the LOD for sulphur is 0.003% by mass of cement (30 ppm) at 3000 s live acquisition time.

3.1 Introduction

The maximum limit for total chloride content is typically 0.2 to 0.4% by mass of cement for steel reinforced concrete structures and 0.1 to 0.2% by mass of cement for pre-stressed concrete structures [BS EN 206, 2013]. The maximum limit for total SO_3 content in concrete is typically set in the range of 3.5 to 4.0% by mass of cement [The Concrete Society, 2014; BS EN 197-1, 2011]. Based on these, it is very important for the μXRF to be able to measure chloride and sulphate at a concentration much lower than the specified threshold values. This can be achieved through optimisation of the measuring conditions. It has been claimed that detection of chloride in reinforced concrete using μXRF can reach as low as 15 ppm [Scruggs et al., 2014], however no details on how this was achieved nor evidence supporting this claim was presented.

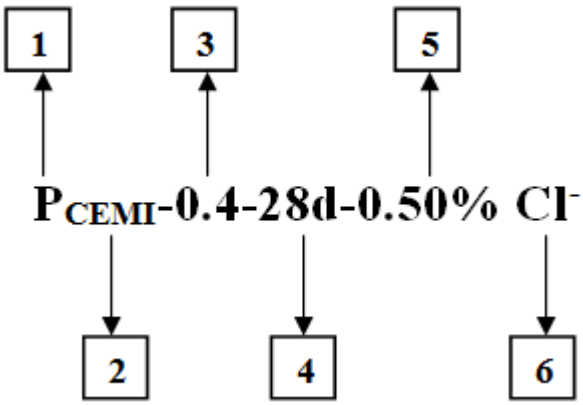
In μXRF analysis, there are at least seven major parameters that affect the accuracy and sensitivity of quantitative analysis of chloride and sulphur in cement-based

materials. These parameters are beam voltage, analysis chamber, filter, acquisition time, time constant, beam spot size, and dead time as reviewed in Chapter 2.5. In the literature, previous studies have focused on employing μXRF for qualitative assessment of penetration of chloride, sulphate, or potassium ions in pastes, mortars or concretes [Davis et al., 2009; Sutter et al. 2009; Schlegel et al., 2011; Davis et al., 2011; Snyder et al., 2012; Alzyoud et al., 2016]. However, quantitative assessment and the optimisation of operating parameters to achieve this were not emphasised or discussed in these studies.

This Chapter aims to fill this gap by understanding the effect of each operating condition on the sensitivity of μXRF to chloride and sulphate in cement-based materials. μXRF cannot distinguish between different chemical species such as sulphates (SO_4^{2-}), sulphites (SO_3^{2-}), and sulphides (S^{2-}). Therefore the sulphur content is assumed to be proportional to the sulphate content as sulphates are the most common sulphur compound in building materials [Weritz et al., 2009].

3.2 Methodology

The samples tested in this Chapter were CEM I cement pastes with water/cement ratio of 0.4 and admixed chloride content of 0.15%, 0.50%, and 2.00% by mass of cement. The sample naming convention that is used throughout this thesis is shown in Figure 3-1.



where:

Number	Definition	Detail
1	Sample type	P is for Paste
2	Binder type	CEM I
3	Water/cement ratio	-
4	Curing age	d is for day
5	Concentration	% by mass of cement
6	Element of interest	Cl^- (chloride) or S (sulphur)

Figure 3-1: Sample naming convention.

3.2.1 Sample preparation

The required amounts of CEM I and water were weighed. The CEM I is known to have an oxide composition of 63.4% CaO, 20.8% SiO_2, 5.4% Al_2O_3, 2.4% Fe_2O_3, 1.5% MgO, 0.7% K_2O, 0.3% Na_2O, and 2.9% SO_3 by mass. The ingredients were mixed using Controls automatic programmable mixer for three minutes which produced a uniform mixture. Tap water was used as the batch water. In mixes containing chloride, the required amount of NaCl (VWR, 98% minimum assay) was weighed and dissolved in the batch water prior to mixing. The mix was then compacted in two equal layers in a plastic cylindrical mould (50 mm diameter, 60 mm height) using a vibrating table. For each layer, the compaction is considered sufficient when no significant air bubbles escaped the surface. The mould was then capped and sealed with waterproof tape to avoid leakage. Subsequently, the mould was fixed to a rotating machine with

adjustable speed and rotated slowly for 24 hour to avoid bleeding and segregation effects.

These steps were repeated to prepare mixes containing different chloride contents (0.15, 0.50, and 2.00% by mass of cement). After the initial 24 hour, some samples still in their plastic containers were wrapped in cling film and sealed in polythene bags at 20^0C until the age of 3 days. Some samples were de-moulded and placed in a fog room at 100% RH, 20°C for curing until the age of 28 day. After the intended curing period, the cylinders were saw-cut into either halves or three equal discs (~50 mm diameter x 15 mm thick) along the transverse axis. The sectioned samples were then freeze dried until constant mass is reached. Freeze drying was chosen as the drying method since it has been reported to be an effective means for preserving the microstructure of samples [Korpa & Trettin, 2006]. The remaining halves or sections were used for other studies.

3.2.2 Freeze drying

Prior to freeze drying, the sectioned samples were weighed using a microbalance that has a precision of 0.0001g. The sectioned samples were then immersed in liquid nitrogen (-196^0C) for approximately 15 to 20 minutes. The rapid freezing of water ensures that microcrystals form in the microstructure instead of large ice crystals that would induce damage. Subsequently, the frozen samples were placed on the tiered sample holder which sits centrally on top of stainless steel chamber of Lyotrap freeze dryer. During operation, the sample holder was concealed with a Perspex cylindrical cover which was topped with a thick round glass plate. The pressure and temperature in the chamber were kept at approximately 0.041 millibar and -50^0C respectively, to remove ice by sublimation. The mass of the sample was monitored using the microbalance and the drying process was terminated when constant mass was achieved. Samples were assumed to have reached constant mass when the mass loss was no more than 0.2% in a 24-hour period. The drying process required around 24 days. Figure 3-2 shows the main components of the Lyotrap freeze dryer.

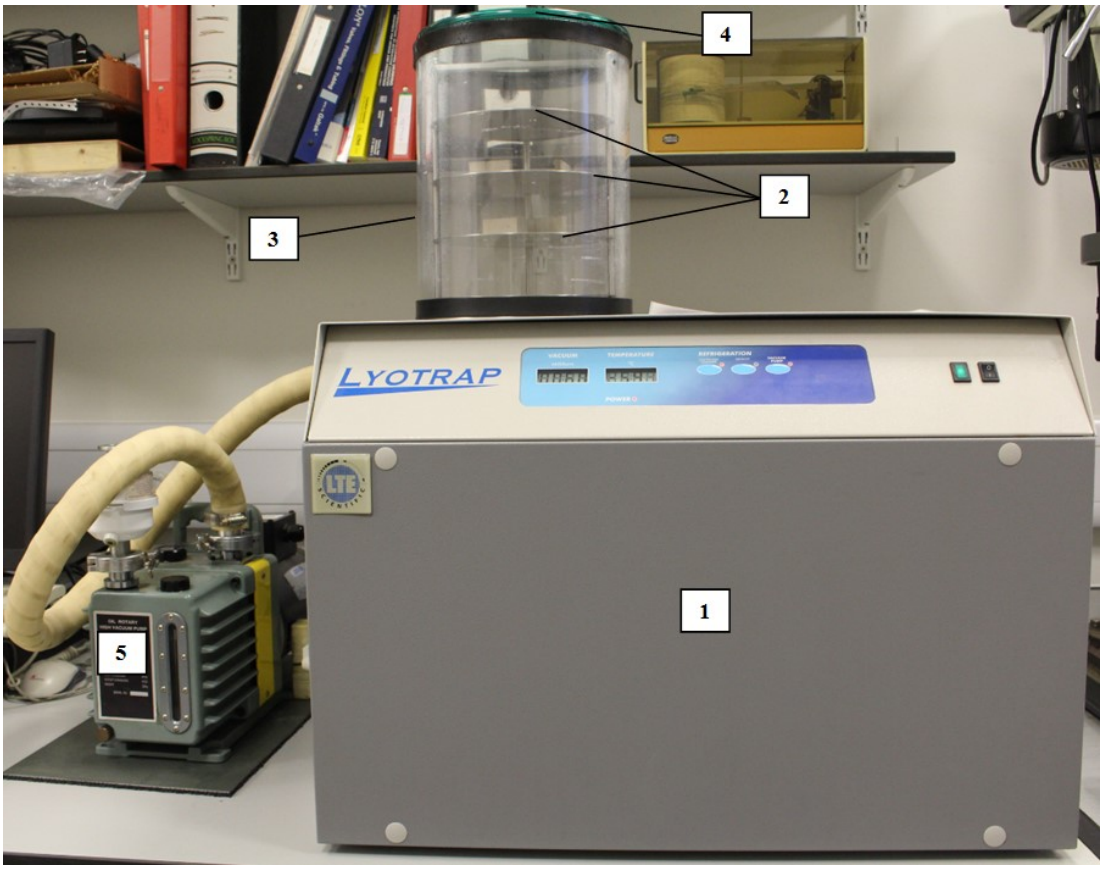


Figure 3-2: The main components of Lyotrap freeze dryer. 1: Stainless steel chamber, 2: Tiered sample holder, 3: Perspex cylindrical cover, 4: Round glass plate, 5: Vacuum pump

3.2.3 Sample surface preparation

At the completion of freeze drying, the saw-cut surface of each sample was ground to produce a flat surface for μXRF analyses. The grinding process was executed using a Struers LaboPol-5 machine with adjustable rational speed. The surfaces were ground using Struers waterproof silicon carbide paper at successively finer grit size starting from 120, and then to 500, 1000, and finally 1200. For each grit size, samples were ground at 100 rpm for approximately 60 seconds and cleaned using compressed air. The ground samples were then sealed in polythene sample bags and placed in a desiccator to prevent carbonation until the time of testing.

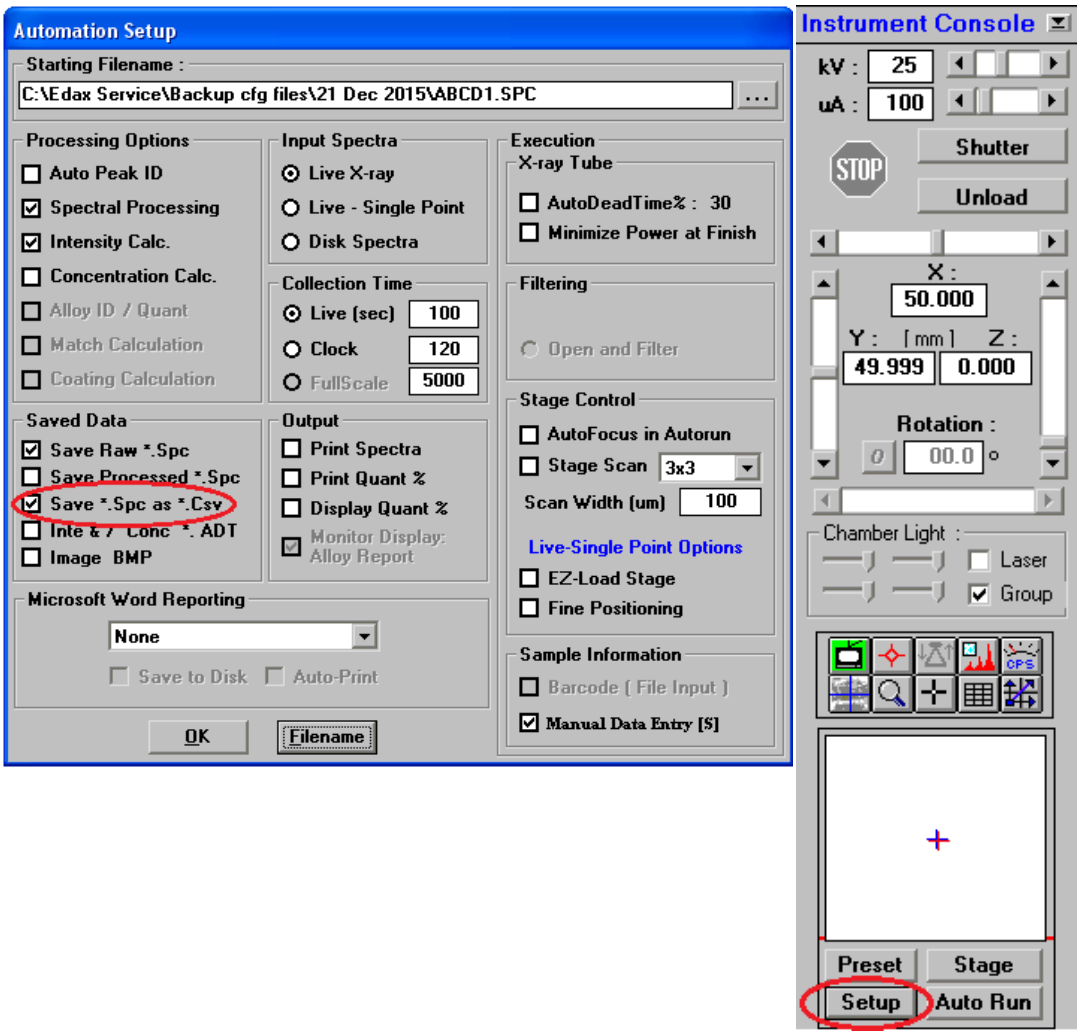
3.2.4 Data acquisition

The procedure for acquiring a raw XRF spectrum using the Orbis PC is summarised here. For each raw data acquisition, sample was first positioned and secured on the plexiglas stage using Blu-Tack. Then, the Z axis of the stage was adjusted so that the sample appears in sharp focus under both low magnification camera (10×) and high magnification camera (70×). Ten to twenty spots on the sample surface were randomly selected using the 'Get Feature' button located on the Instrument Console. Then, the camera image under high magnification view was used to move the sample to the locations of interest. Selection of the locations for spot analysis was done under high magnification view since the image appears clearer and hence inappropriate locations such as large voids or cracks could be avoided. The locations to be analysed were saved on the Orbis Vision Stage Location table, which is accessed via the Stage option on the Instrument Console. Then, the Automation Setup table was setup to save all the generated data during Auto Run analysis. Finally, Auto Run was executed to start data acquisition. Alternative procedures for selection of locations of analysis to saving the generated data are explained in detail in the EDAX Orbis Vision User's Manual [2009]. The operating conditions used to study each parameter are described in the subsequent sections (Chapter 3.3).

3.2.5 Data analysis

To obtain the net X-ray counts for quantitative analysis of a particular element of interest, the measured raw X-ray spectrum must be processed to remove background counts. In this thesis, background subtraction will be based on the method proposed by Ernst et al. [2012]. According to this method the net signal and background count for a peak of an element can be calculated by first designating the energy range or region of interest corresponding to that peak. The peak ranges were determined through a process that considered software default ranges as well as visual inspection of the reference standards and typical soda-lime glass spectra. For each element, the pre-peak and post-peak energy ranges were also specified and set to start 0.05 keV away from the designated region of interest to prevent counts from the element being included in these regions. This method also provides a straightforward approach for estimating signal to noise ratios, limit of detection, and limit of quantification. No attempts however were made to deconvolute overlapping peaks.

To carry out background subtraction, the raw spectrum is saved in the format of comma-separated values (CSV) file. This is done by selecting the 'Save *.Spc as *.Csv' box in the Automation Setup dialog, as highlighted with the red circle in Figure 3-3 (a). The Automation Setup dialog is accessed via the Setup button on the Instrument Console which is located on the right side of the software interface. This is highlighted in Figure 3-3 (b).



(a) **(b)**

Figure 3-3: Setup for generating raw spectra in comma-separated value (CSV) file format, (a) Automation Setup dialog, and (b) Instrument Console.

The default region of interest (ROI) for chloride K peak set in the Orbis Vision software is from channel 253 – 271, which correspond to energy of 2.53 – 2.71 keV. The default ROI for sulphur K peak is from channel 222 – 240 corresponding to energy of 2.22 – 2.40 keV. This means that incoming X-ray photons detected in channels 253 – 271 are considered as chloride characteristic X-rays and those in channels 222 – 240 are categorised as sulphur characteristic X-rays. These two ROIs were adopted throughout this work.

In a typical raw XRF spectrum, photons in these two sets of channels as well as photons in the ROI for other elements are inclusive of background photons. In order to define the background level in the ROI for chloride, three pre-channels (250, 251 & 252) and three post-channels (272, 273 & 274) were selected. These channels were selected as they do not interfere with the ROI for sulphur, which is one atomic number below chlorine and the ROI for argon, which is one atomic number above. Figure 3-4 shows an example of the manual background subtraction method for chloride peak. The average value of the photon counts in the pre-channels and post-channels was then used to define the background baseline for the chloride peak. In the example shown in Figure 3-4, the background baseline was calculated as 1313 (represented by the blue line). The sum of background count was then determined by multiplying the number of channels in the ROI of chloride (19) with the background baseline. Finally, the net count for chloride was calculated by subtracting the background count from the total count registered in channels 253 – 271. In the example shown in Figure 3-4, the net count was calculated as 6765 and this represents the number of detected chloride X-ray photons for the particular sample. Background subtractions were done in Microsoft Excel. Figure 3-5 summarises the steps for manual background subtraction for chloride peak. ‘BG’ in the flowchart represents ‘background’.

The procedure for background subtraction in the ROI for sulphur is identical to that for chloride. The only difference is that the range of pre-channels and post-channels for sulphur were defined as 219 – 221 and 241 – 243 respectively.

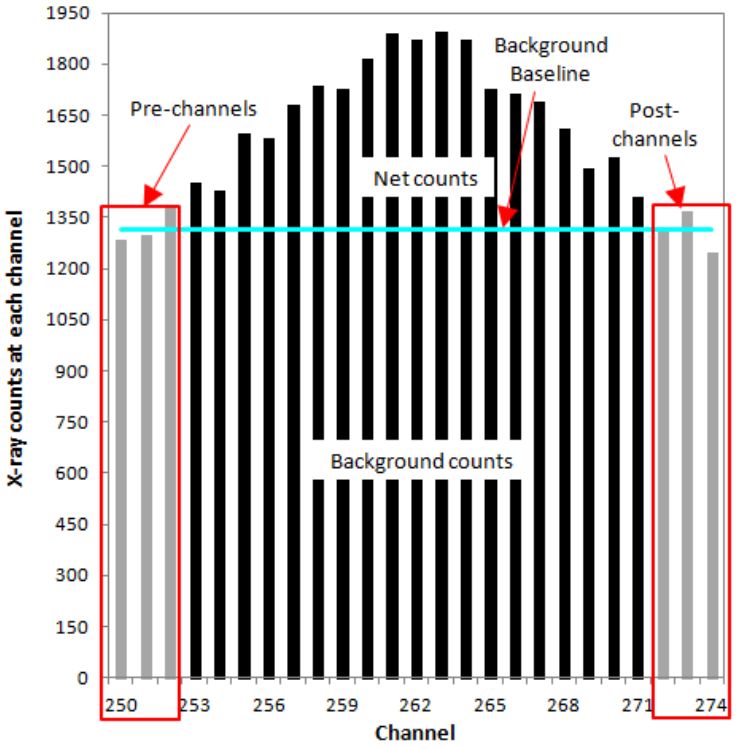


Figure 3-4: Background subtraction to obtain net counts for chloride peak.

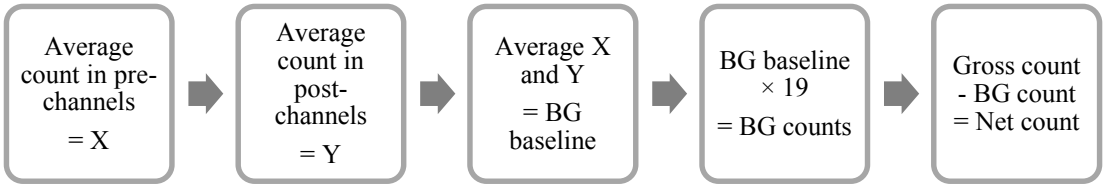


Figure 3-5: Flow chart for background subtraction.

The quality of the measured data was assessed from its signal-to-noise ratio (SNR) and limit of detection (LOD). SNR was calculated using Equation 3-1. Here, the term *Signal* in this equation is equal to the 'net count' that was mentioned in the preceding paragraphs. According to the recommendation given by the American Chemical Society [ACS Committee, 1983], an element is considered to be present and its peak may be labelled in the XRF spectrum if the SNR is three or greater. If this condition is satisfied, then the element is considered to be present at a concentration that is higher than the background noise by a statistically significant amount.

$$SNR = \frac{Signal}{\sqrt{Background}} \qquad \textbf{Eq. 3-1}$$

The limit of detection (LOD) was calculated using Equation 3-2. According to the American Chemical Society [ACS Committee, 1983], the LOD is defined as the lowest concentration of an element of interest that can be determined to be statistically different from a blank sample. In Equation 3-2, c is the known concentration of the element of interest. As an example, if c is 0.15% chloride by mass of cement and the measured SNR is 6, then the LOD is 0.08% chloride by mass of cement.

$$LOD = \frac{3 \times c}{SNR} \qquad \textbf{Eq. 3-2}$$

The sulphur present in the cement was used for the calculation, which means no additional sulphur was added for the purpose of this study. The percentage of sulphur in sulphur trioxide (SO_3) was calculated by dividing the molar mass of sulphur (32.064 g/mol) by the molar mass of sulphur trioxide (80.061 g/mol). The value was then multiplied by 100 to obtain the percentage which is 40.05%. The sulphur content of the cement was then obtained by multiplying 40.05% by 2.9% sulphur trioxide content of the cement. The sulphur content in the cement was therefore 1.16% by mass and was used to calculate the LOD of sulphur using Equation 3-2.

Note that the results presented will be an average of several repeat measurements. Variation is presented as the standard error ($S.E = \frac{\sigma}{\sqrt{n}}$), where σ is the standard deviation and n is the number of analysed spots.

3.3 Results and discussions

Results are reported in the form of SNR and LOD to help in understanding the effects of various operating parameters on quantitative μXRF analysis. This will also assist in determining which operating condition can improve the sensitivity of μXRF to both chloride and sulphur analyses.

3.3.1 Beam voltage

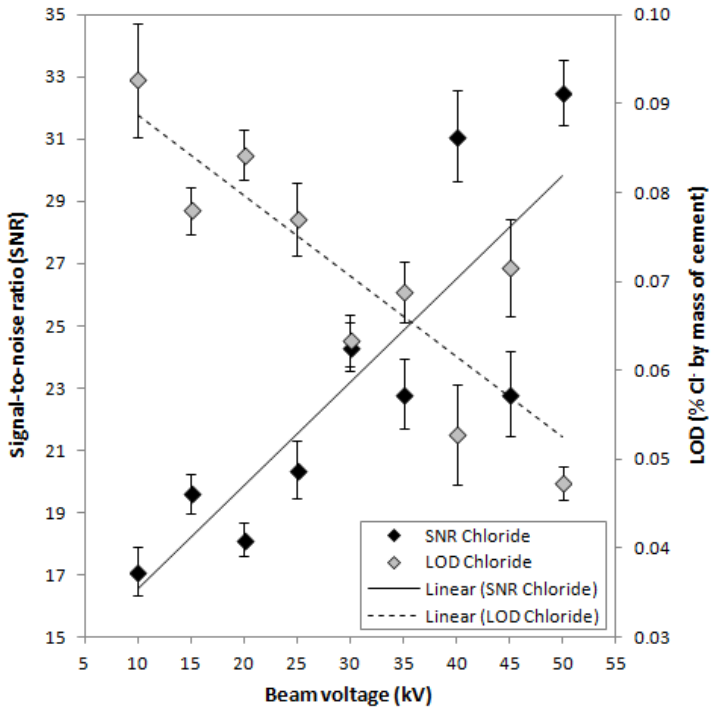
Table 3-1 shows the operating condition employed for the study on the effect of beam voltage on the SNR and LOD for chloride and sulphur in P_{CEMI}-0.4-28d-0.50% Cl^-. The investigated beam voltage were between 10 and 50 kV. This range was selected because it spans the minimum and maximum beam voltage applicable for the Orbis μXRF.

Table 3-1: Operating condition for the study on the effect of beam voltage.

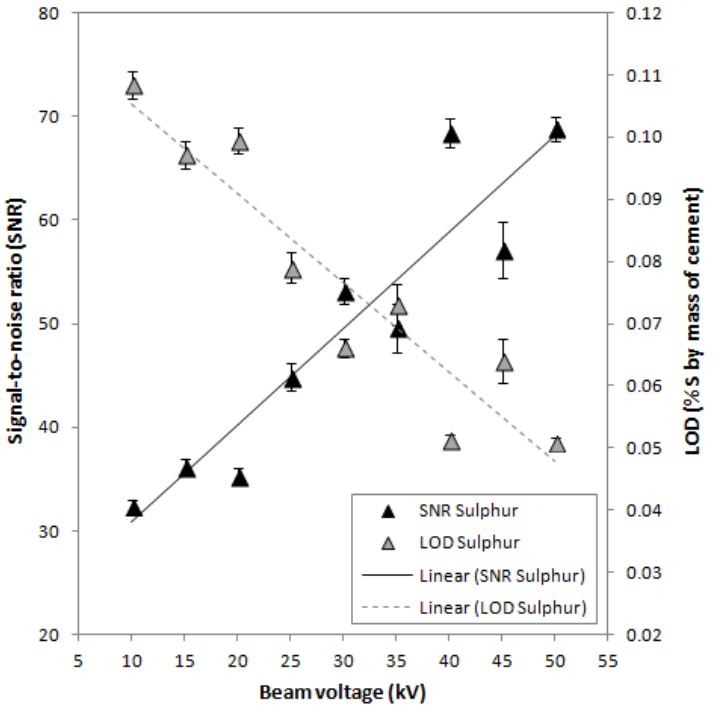
Dead time: 30%, Time constant: 12.8 μs, Beam: 30 μm, Chamber: Vacuum, Filter: 25 μm Al, Acquisition time: 200 s live	
Beam voltage (kV)	Beam current (μA)
10	570
15	260
20	180
25	140
30	120
35	105
40	95
45	90
50	80

As seen in the table, beam current has to be adjusted at each beam voltage under investigation in order to obtain a 30% dead time. If the beam current is fixed to one value, the dead time will inevitably vary when beam voltage is adjusted.

The effect of beam voltage on the SNR for chloride and sulphur is shown in Figure 3-6. Each point is an average of twenty measurements. The error bars represent the standard error of the mean value.



(a)



(b)

Figure 3-6: Effect of beam voltage on the (a) SNR and LOD for chloride, and (b) SNR and LOD for sulphur in P_{CEMI}-0.4-28d-0.50% Cl^-.

As seen in Figure 3-6 (a) and (b), the SNR for all measurements were much greater than 3, which confirms the analysis detected presence of chloride and sulphur in the sample. It can also be observed that increasing the beam voltage increases the measured SNR for both chloride and sulphur and improves the LOD. This is expected since LOD is inversely proportional to SNR (Eq. 3.2).

Figure 3-6 (a) shows that the LOD of chloride is approximately 0.09% by mass of cement when a beam voltage of 10 kV was used. This is equivalent to 900 ppm. At 50 kV beam voltage, the LOD of chloride improves to approximately 0.05% by mass of cement, which is equivalent to 500 ppm. This suggests that even at the lowest beam voltage, μXRF is able to detect chloride concentration below the threshold value for initiation of reinforcement corrosion, which is typically in the range of 0.2 – 0.4% by mass of cement for reinforced concrete structures and 0.1 – 0.2% by mass of cement for pre-stressed concrete structures.

Figure 3-6 (b) shows that the LOD of sulphur is approximately 0.11% by mass of cement when a beam voltage of 10 kV was used. This shows that the LOD achieved is comfortably below the threshold for sulphate attack risk (typically 4% by mass of cement), even at the lowest beam voltage. At 50 kV beam voltage, the LOD of sulphur improves to 0.05% by mass of cement.

It is also observed that the standard errors for SNR are smaller at lower beam voltages for both chloride and sulphur. Based on the email discussion in January 2015 with Paul Wright and Andrew Lee both from Edax-Ametek, the minimum beam current for μXRF application was set at 50 μA to give good reading stability. Table 3-1 shows that the beam current at 10 and 50 kV was 570 and 80 μA respectively. The readings at 10 kV were therefore more stable since these were obtained at higher beam current, thus leading to smaller standard errors. Another possible explanation for the lower standard errors is due to the smaller X-ray sample interaction volume when analysed at lower beam voltages.

The observed trends can probably be explained by considering the effects of beam voltage on the position of the bremsstrahlung (background) radiation. At low beam voltages, the bremsstrahlung will be centred at relatively low energies while at high

beam voltages the bremsstrahlung will be more intense, but centred at higher energies [Horiba, 2016]. Both the chloride and sulphur peaks are located at ROI of 2.53 – 2.71 keV and 2.22 – 2.40 keV respectively, which are considered to be in the low energy range. As such, both peaks will be significantly obscured by the bremsstrahlung radiation at low beam voltages and thus leading to lower SNR. At a high beam voltages, the chloride and sulphur peak are more pronounced since the background radiation is centred at higher energies. This results in a greater SNR and lower LOD. This effect is shown Figure 3-7.

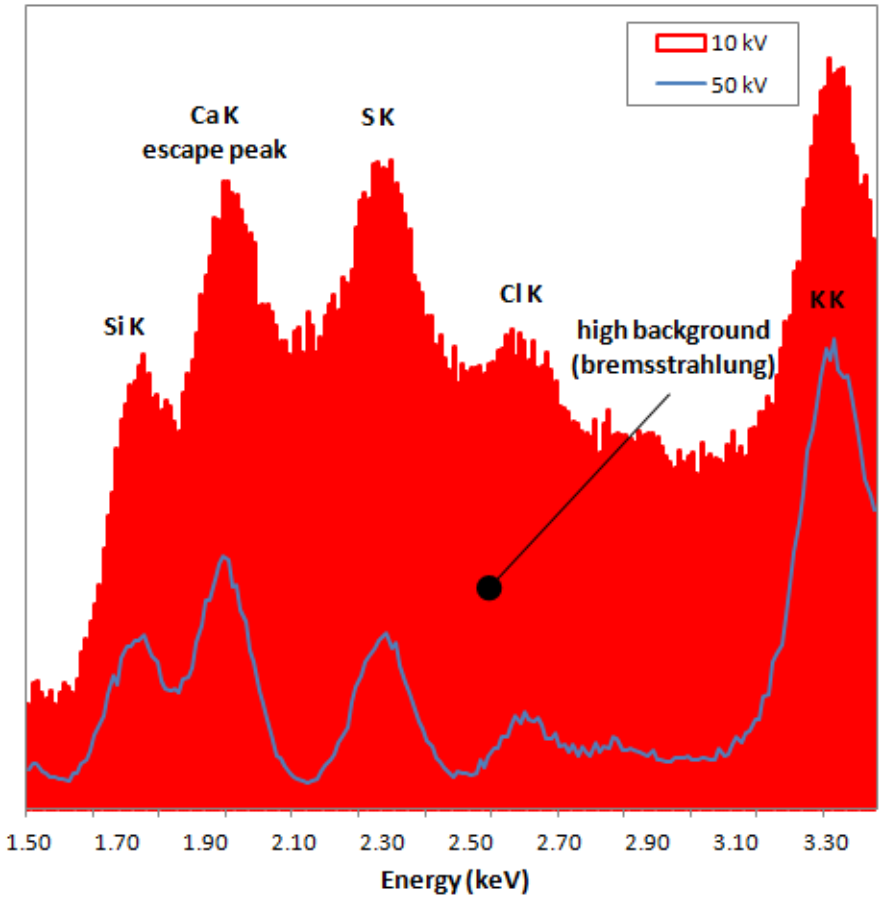


Figure 3-7: Effect of beam voltage on the intensity of bremsstrahlung radiation and visibility of elements at low energies.

3.3.2 Analysis chamber

The μXRF analysis can be carried out in a sample chamber that is under a high vacuum condition (11 Pa) or at ambient (air) pressure. Figure 3-8 shows the effect of analysis

chamber environment on the SNR and LOD for chloride and sulphur in P_{CEMI}-0.4-3d-2.00% Cl^-. For this set of experiment, the beam voltage used was 15 kV and the beam current was adjusted to reach 30% dead time. The acquisition live time, time constant, and beam size was 100 s, 12.8 µs, and 30 µm respectively. The analysis was carried out on 20 different locations (points) and with the application of a 25 µm Al filter.

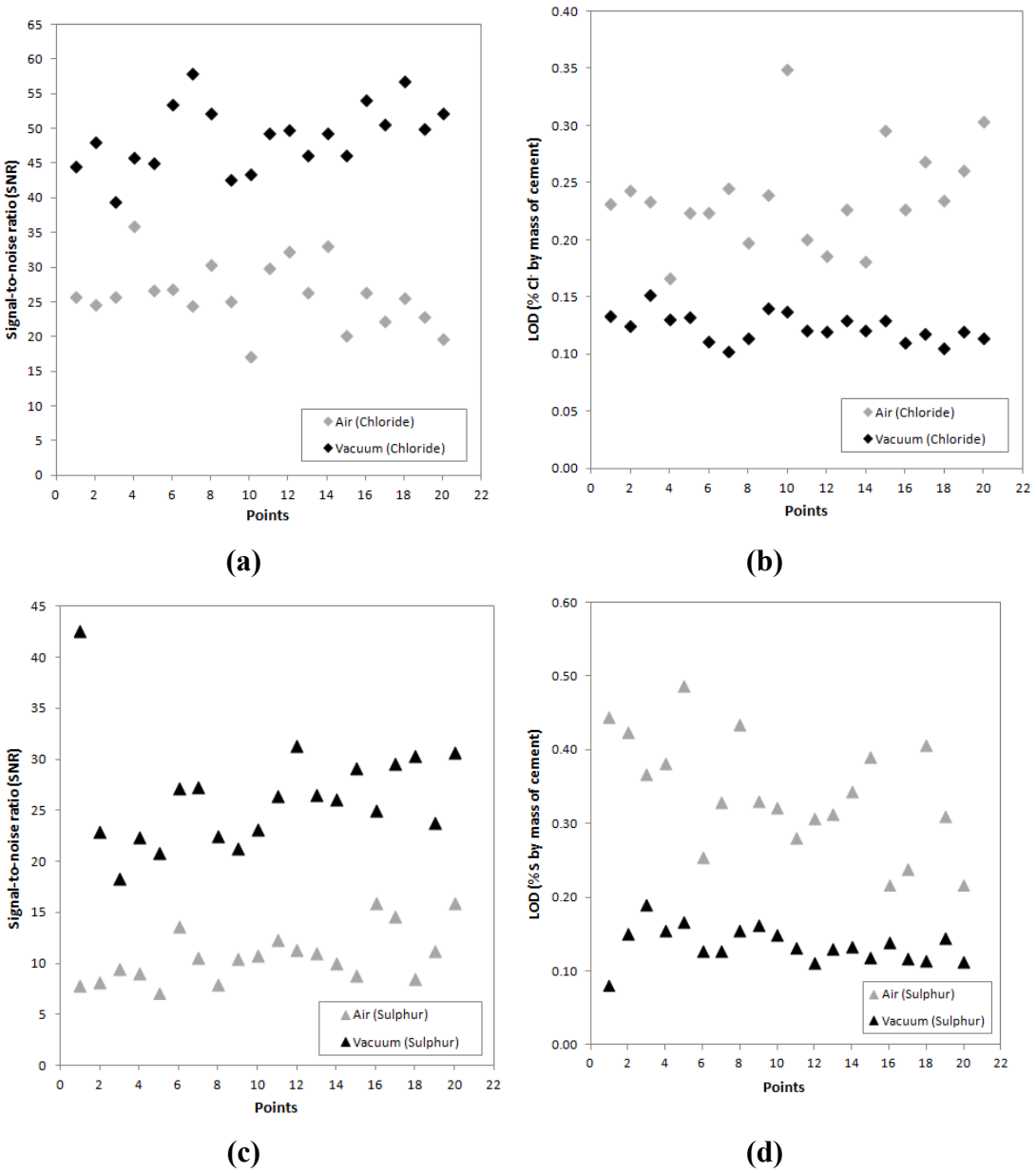


Figure 3-8: Effect of analysis chamber on the (a) SNR for chloride, (b) LOD for chloride, (c) SNR for sulphur, and (d) LOD for sulphur in P_{CEMI}-0.4-3d-2.00% Cl^-.

Figure 3-8 shows that both chloride and sulphur were detectable when the analysis was conducted in an ambient environment (air chamber). However, the SNR and LOD improved significantly when the analysis was conducted in a vacuum chamber. This shows that the chloride and sulphur fluorescence radiations were attenuated by the presence of gas molecules (mainly nitrogen, oxygen) in the air thus leading to lower SNR for both peaks in air chamber. For this particular example, the LOD for chloride was approximately 0.24% by mass of cement when measured in air chamber. This improved to approximately 0.12% by mass of cement when the analysis was carried out in a vacuum chamber. These are higher than the threshold value for corrosion initiation for pre-stressed concrete structures which is 0.1 to 0.2% by mass of cement [BS EN 206, 2013]. In this example, chloride concentrations < 0.12% by mass of cement could not be detected because the analyses were carried out at low beam voltage (15 kV) and short acquisition time (100 s). At these settings, the chloride peak was partially obscured by the bremsstrahlung radiation leading to lower SNR and greater LOD (Section 3.3.1). The effect of acquisition time on the SNR and LOD for chloride and sulphur is discussed in Section 3.3.4. The LOD for sulphur was approximately 0.34% by mass of cement when measured in air chamber. This improved to approximately 0.14% by mass of cement when the analysis was carried out in vacuum chamber.

3.3.3 Filter

The main function of the 25 μm Al filter is to remove the Rh L artefact peak. This is beneficial because the Rh L peak has default ROI energy range of 2.60 – 2.78 keV that overlaps with that of the chloride peak (2.53 – 2.71 keV) in the collected spectra. Therefore, applying the 25 μm Al filter should improve the sensitivity for chloride analysis. This effect is shown in Figure 3-9. The sample used was P_{CEMI}-0.4-28d-0.50% Cl^-. The analysis was carried out at a beam voltage of 35 kV and beam current was adjusted to reach 30% dead time. The acquisition live time, time constant, and beam size was 200 s, 12.8 μs, and 30 μm respectively. The analysis was carried out in a vacuum chamber.

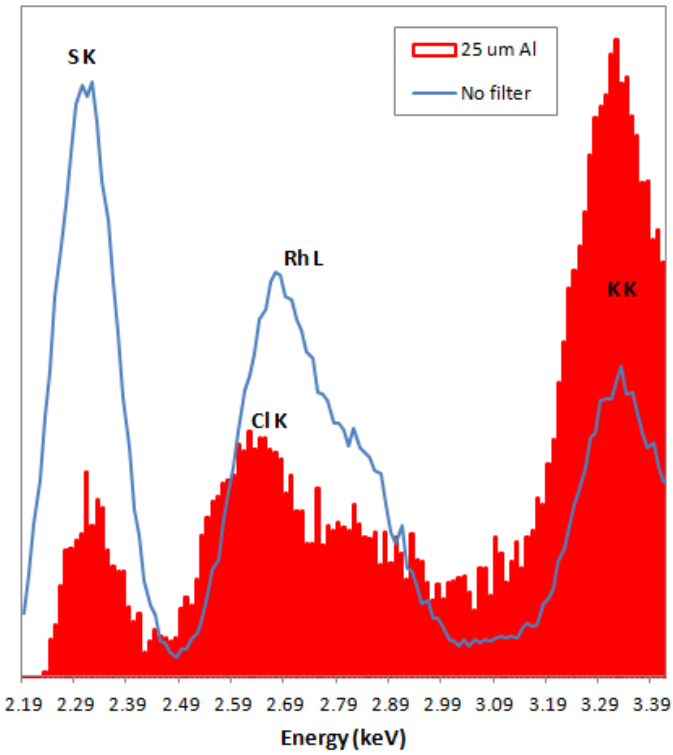


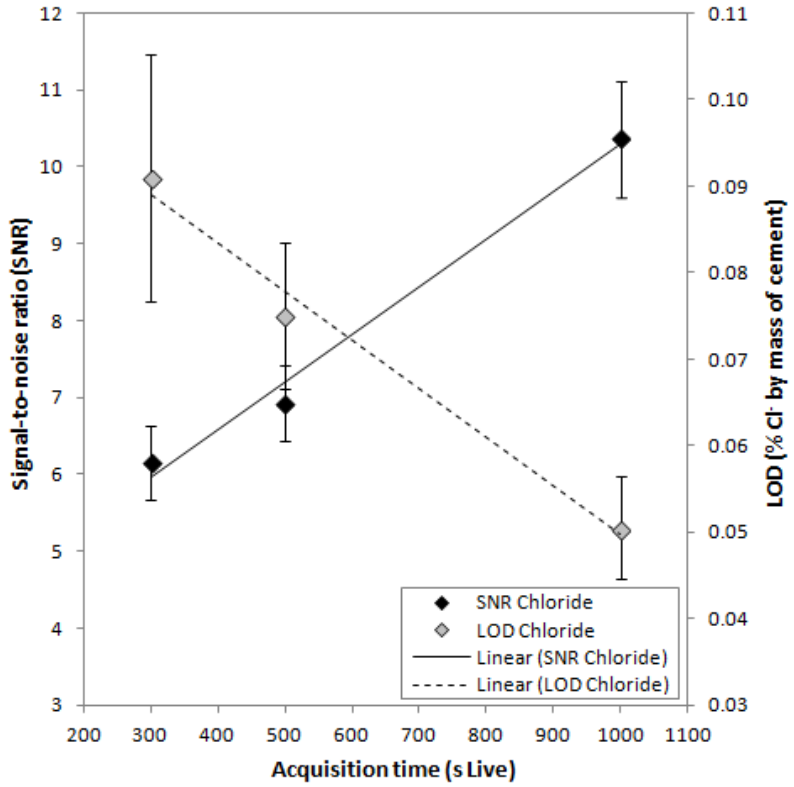
Figure 3-9: Removal of Rh L peak using 25 µm Al filter to improve detection of chloride.

The results show the chloride and Rh L peaks merge if the analysis was carried out without filler. With the application of 25 µm Al filter, Rh L peak is removed and the chloride peak is more pronounced. However, it should be noted that the default ROI for sulphur peak (2.22 – 2.40 keV) does not overlap with the Rh L spurious peak. Furthermore, the application of the 25 µm Al filter decreases the collected signal intensity for sulphur because of the attenuation of the low energy characteristic X-rays of sulphur (2.22 – 2.40 keV) by the filter. Therefore, the application of Al filter would not be recommended for sulphur analysis.

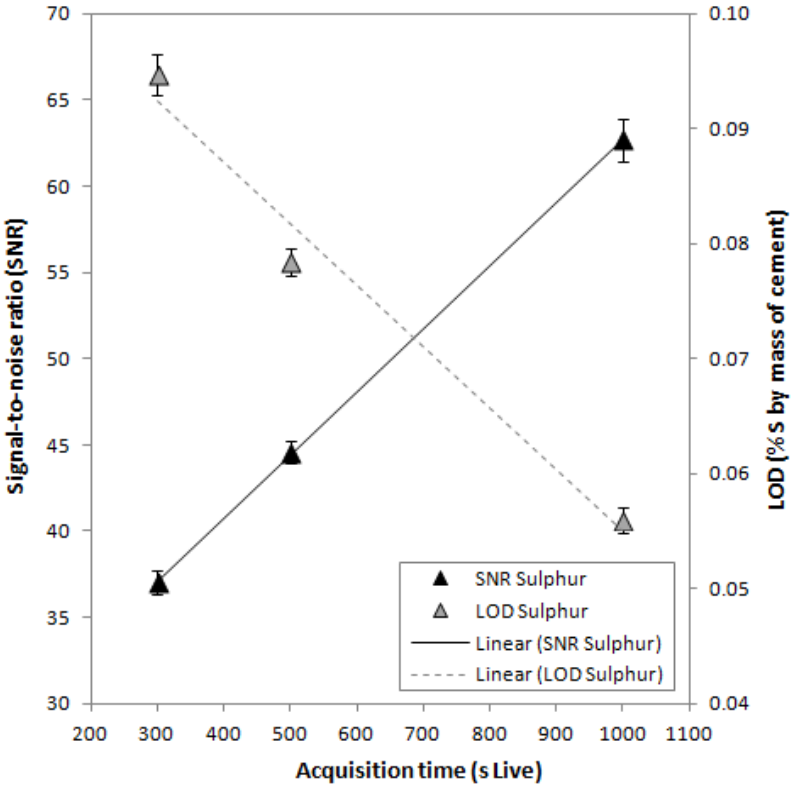
3.3.4 Acquisition time

The effect of acquisition time on the SNR and LOD for chloride is shown in Figure 3-10 (a) and its effect on the SNR and LOD for sulphur is shown in Figure 3-10 (b). The sample used in this experiment was P_{CEMI}-0.4-28d-0.15% Cl^-. The beam voltage was 11 kV and beam current was adjusted to 200 μA to achieve 30% dead time throughout. The analyses were conducted under vacuum and with the application of 25 μm Al filter. Time constant and beam spot size was 25.6 μs and 30 μm respectively.

It can be observed that increasing the acquisition time results in improvements in both the SNR and LOD for chloride and sulphur peaks. The greater the SNR, the lower will be the LOD of chloride in the sample. For example, at 300 s acquisition time, the SNR and LOD for chloride was 6 and 0.09% by mass of cement respectively. When the acquisition time was increased to 1000s, the SNR and LOD improved to 10.5 and 0.05% by mass of cement respectively. Therefore, chloride contents lower than the threshold value for corrosion initiation (0.1 to 0.4% by mass of cement) can be detected even at short acquisition times. This is important since an ideal condition for most analyst is to achieve a sufficiently low LOD within a short analysis time. For sulphur, the SNR and LOD at 300 s acquisition time was 37 and 0.09% by mass of cement respectively. At the acquisition time of 1000 s, the SNR and LOD improved to 63 and 0.06% by mass of cement respectively. This improvement occurs because total signal increases with increase in collection time, while the noise level varies with the square root of collection time [Ernst et al, 2012].



(a)



(b)

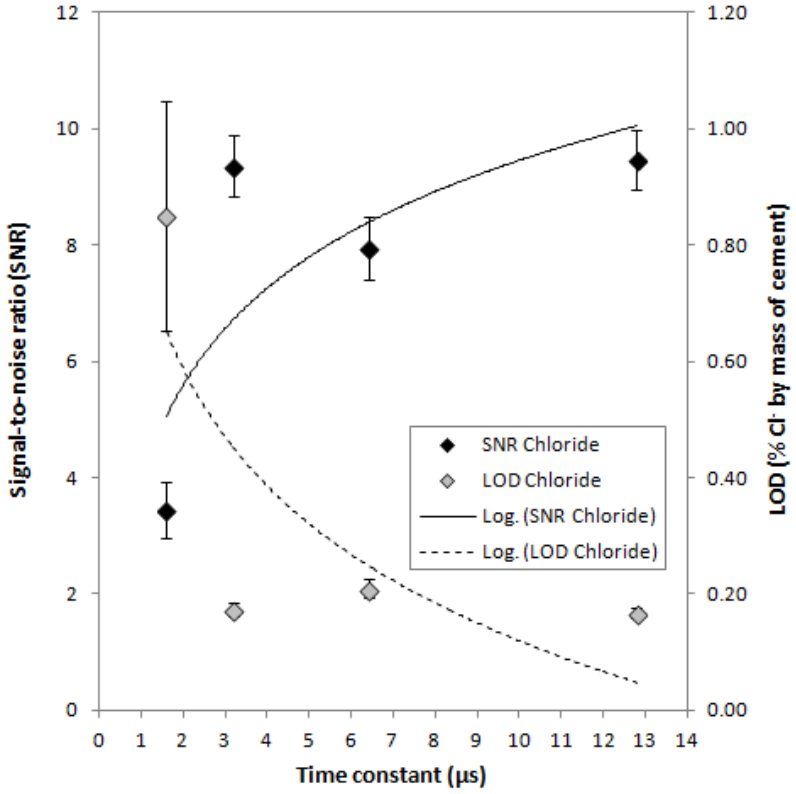
Figure 3-10: Effect of acquisition time on the (a) SNR and LOD for chloride, and (b) SNR and LOD for sulphur in P_{CEMI}-0.4-28d-0.15% Cl^-.

3.3.5 Time constant

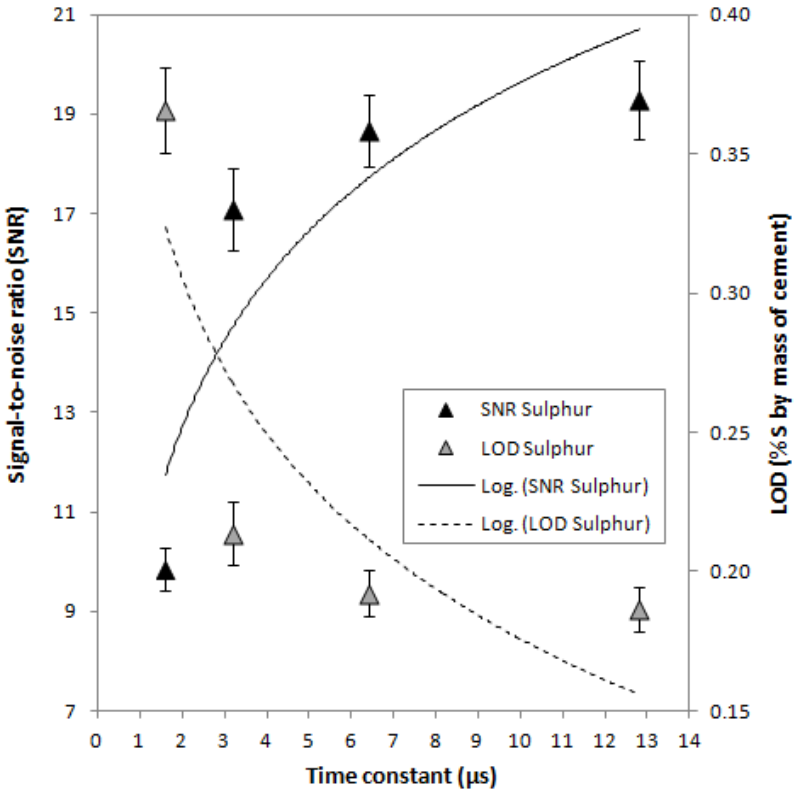
Two sets of operating conditions were used to study the effect of time constant. This is due to the fact that one set of operating condition alone cannot achieve the same dead time for all the seven different time constants (1.6, 3.2, 6.4, 12.8, 25.6, 51.2, and 102.4 µs). The analysis was carried out on P_{CEMI}-0.4-28d-0.50% Cl^-.

The first set of operating condition was used to study the effect of time constants 1.6, 3.2, 6.4, and 12.8 µs. Beam voltage employed was 25 kV and beam current was adjusted to achieve 20% dead time. Beam size was 30 µm and the analyses were conducted in vacuum chamber with the application of 25 µm Al filter. The acquisition live time was 100 s. The effect of time constant on the SNR and LOD for chloride is shown in Figure 3-11 (a) while on the SNR and LOD for sulphur is shown in Figure 3-11 (b). Each point is an average of twenty measurements except the first point for both SNR and LOD for chloride, which was an average of nineteen measurements. The error bars represent the standard error of the mean value.

As seen in Figure 3-11 (a), the SNR for chloride increased from approximately 3 at 1.6 µs to 9 at 3.2 µs, and stayed relatively constant at 6.4 µs and 12.8 µs. The corresponding LOD for chloride improved when the time constant was increased from 1.6 µs to 3.2 µs, and remained relatively constant beyond 3.2 µs. Therefore, the general trend is that both the SNR and LOD for chloride improved at higher time constants. A similar trend is observed for sulphur as seen in Figure 3-11 (b).



(a)



(b)

Figure 3-11: Effect of time constants 1.6, 3.2, 6.4, and 12.8 µs on the (a) SNR and LOD for chloride, and (b) SNR and LOD for sulphur in PCEMI-0.4-28d-0.50% Cl⁻.

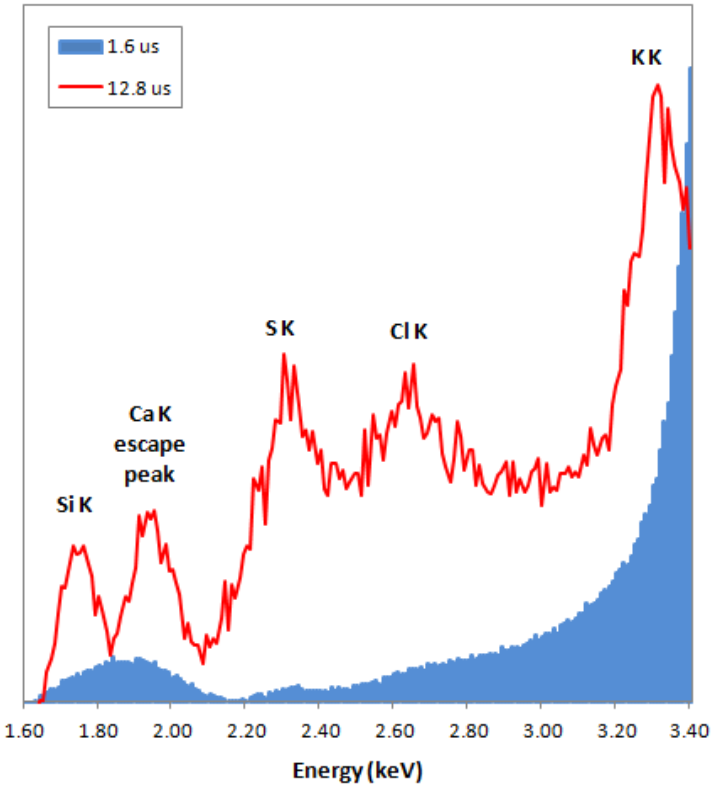


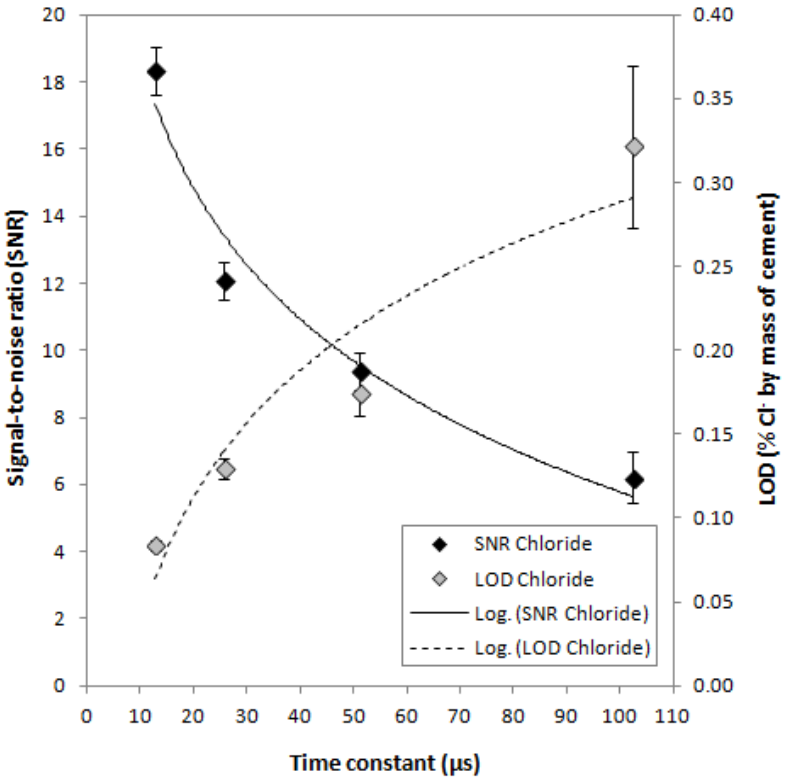
Figure 3-12: Effect of time constant (1.6 and 12.8 µs) on the resolution of elemental spectrum

The results show indicate that the resolution of elemental spectrum degrades at lower time constants and improves at higher time constants as observed by New & Tily [1994]. At short time constants, there is a higher probability that the photons emitted by sample would not be processed accurately and therefore assigned to less accurate energy addresses. This degrades the resolution of the obtained spectra and may cause peak to overlap. At a longer time constants, the photons would be processed more accurately and assigned to the correct energy addresses. Therefore the resolution of the peaks improved with higher time constant. This is shown in Figure 3-12 where it can be seen that the peaks for Si K (ROI 1.65 – 1.82 keV) and Ca K escape peak have merged when a low time constant (1.6 µs) was used. Similarly, the peaks for S K (ROI 2.22 – 2.40 keV) and Cl K (ROI 2.53 – 2.71 keV) were not detectable, but appeared as a broad shoulder to the K K peak (ROI 3.22 – 3.41 keV). When a longer time constant of 12.8 µs was used, all the element peaks were individually more pronounced and therefore leading to improved SNR and LOD.

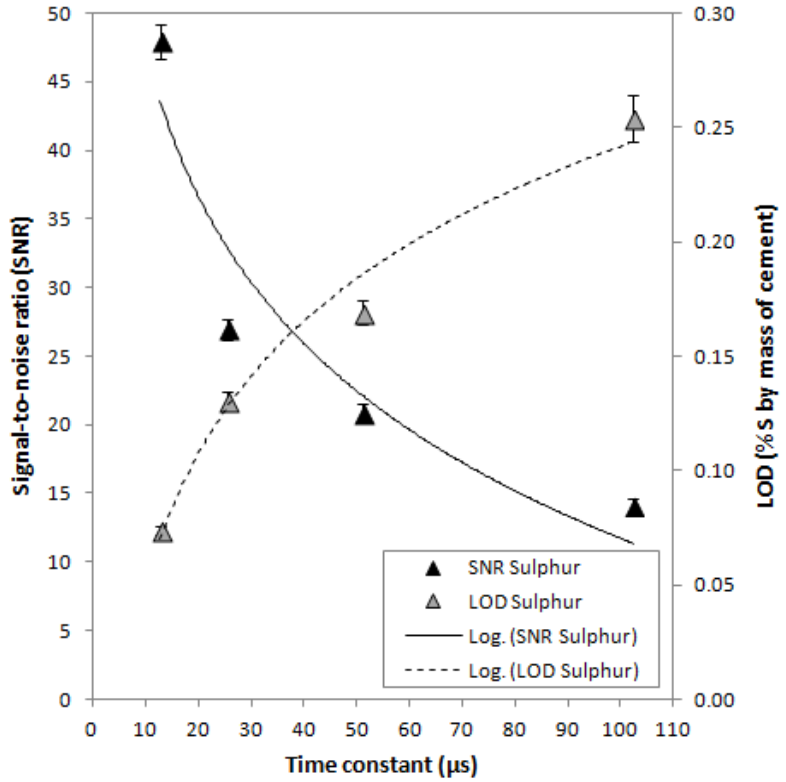
A second set of operating condition was used to study the effect of time constants 12.8, 25.6, 51.2, and 102.4 μs. Beam voltage was 15 kV and beam current was adjusted to reach 50% dead time. The rest of the operating parameters were identical to those in the first set. The effect of time constant on the SNR and LOD for chloride is shown in Figure 3-13 (a) while on the SNR and LOD for sulphur is shown in Figure 3-13 (b). Each point is an average of twenty measurements except the last point for both SNR and LOD for chloride, which was an average of nineteen measurements. The error bars represent the standard error for the mean value.

Interestingly, the results show a very different trend to that obtained in the first set of measurements. The SNR for chloride and sulphur were the highest at time constant of 12.8 μs and then degraded at the longer time constants. The corresponding LOD showed a similar pattern where it was the lowest at 12.8 μs and degrading at longer time constants.

This was rather unexpected because the first set of measurements suggested that the SNR and the corresponding LOD will improve at higher time constants due to an improvement in the resolution of the peaks. However this was not the case. According to Newbury [2009], although the resolution of elemental peaks improves at longer time constants, beyond a certain value the output count rate decreases and this could degrade the SNR and LOD for a particular element. This is supported by the data from this study showing that the net output count rate for chloride after background subtraction decreased from 26 to 4 counts per second (CPS) when the time constant was increased from 12.8 to 102.4 μs. For sulphur, the net output count rate decreased from 56 CPS at 12.8 μs to 10 CPS at 102.4 μs. As mentioned previously, beam current was adjusted to reach 50% dead time at each time constant under investigation. As an example, beam current was 520 and 55 μA at time constant of 12.8 and 102.4 μs respectively. If the beam current is fixed at one value, the dead time will be higher at longer time constant. The decrease in beam current explains the decrease in the count rate of chloride and sulphur at longer time constants.



(a)

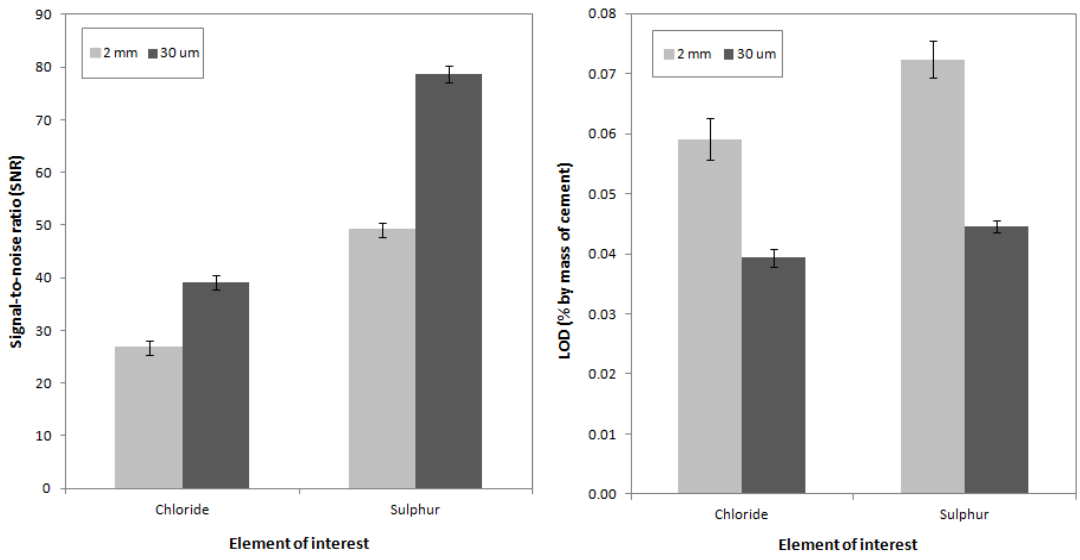


(b)

Figure 3-13: Effect of time constants of 12.8, 25.6, 51.2, and 102.4 µs on the (a) SNR and LOD of chloride, and (b) SNR and LOD of sulphur in P_{CEMI}-0.4-28d-0.50% Cl^-.

3.3.6 Beam spot size

The effect of beam spot size on the SNR for chloride and sulphur is shown in Figure 3-14 (a) while on the LOD for chloride and sulphur is shown in Figure 3-14 (b). The sample used was P_{CEMI}-0.4-28d-0.50% Cl^-. Beam voltage employed was 35 kV and beam current was adjusted to reach 30% dead time. Time constant and acquisition time was 12.8 µs and 200 s respectively. The analyses were carried out in vacuum chamber and with the application of 25 µm Al filter. Each column is an average of twenty measurements. The error bars represent the standard error for the mean value.



(a) **(b)**

Figure 3-14: Effect of beam spot size (30 µm, 2 mm) on the (a) SNR for chloride and sulphur, and (b) LOD for chloride and sulphur in P_{CEMI}-0.4-28d-0.50% Cl^-.

The results show that the SNR and LOD for both chloride and sulphur improved when a smaller beam spot size (30 µm) was used. This finding can be explained by considering the design of the X-ray optics itself. The Orbis µXRF used in this study employs collimating X-ray optics to convert highly divergent beam of X-rays into 1 or 2 mm beam size. X-rays entering the tube will reflect off the inner surface of the brass guide and at each reflection point, X-rays will lose some energy. Lower energy photons will be too weak to transmit efficiently through the entire tube without getting attenuated at each reflection point. Energetic photons will transmit more efficiently since less total energy is lost at each reflection. These collectively lead to a low X-ray flux and thus lower SNR. In contrast, the 30 µm spot size in Orbis utilises a poly-capillary that consists of a bundle of fibres of 3 – 5 µm diameter. These capillaries

adopt total internal reflection (TIR) based on Snell's law to guide X-rays in the optic, which gives minimal energy loss since almost all energy is conserved at each reflection. The poly-capillary optics for the 30 μm beam in Orbis produces high X-ray flux and this leads to greater SNR. Nevertheless, the LOD for chloride obtained using the 2 mm beam size is 0.06% by mass of cement, which is still comfortably below the threshold level for corrosion initiation. Similarly, the LOD for sulphur at 2 mm beam size is 0.07% by mass of cement, which is also below the threshold for sulphate attack.

Figure 3-15 shows the beam sizes available for application in the Orbis μXRF superimposed on to a concrete sample for comparative purpose. Note that the actual size of the 30 μm beam is too small to be shown and therefore the red spots in Figure 3-15 (a) do not represent the actual scale of the 30 μm beam. However, the red circle in Figure 3-15 (b) and (c) represents the actual size of the 1 and 2 mm beam respectively. These three images were collected with the high magnification camera (70×).

As seen in the figure, the 30 μm beam is able to precisely pinpoint the paste regions in concrete, thus giving a higher spatial resolution. However, the beam sizes of 1 and 2 mm are too large for analyses at the micro scale as these would inevitably include aggregate particles or defects such as cracks and air voids. Thus, these beam sizes are not appropriate for the purpose of identifying paste regions in concretes. However, if the purpose of the analysis is to obtain macro-scale composition over a larger sample volume, then the use of the 1 and 2 mm beam size may be more appropriate. The identification of cement pastes and aggregate regions in concretes using μXRF will be further explored in detail in Chapter 4.

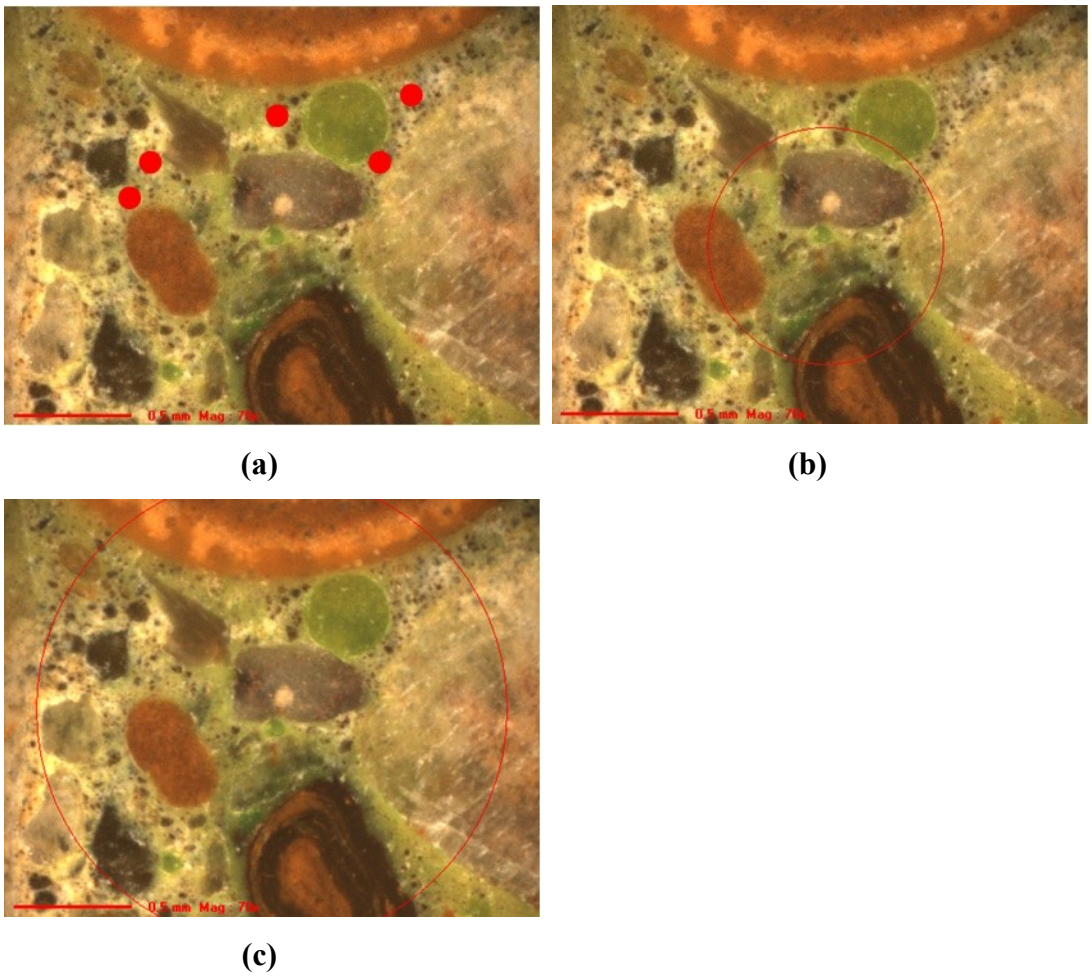


Figure 3-15: Beam sizes available for µXRF analysis, (a) 30 µm, (b) 1 mm, and (c) 2 mm. Note that the 30 µm beam is too small to be shown on (a), thus the red spots are not to scale.

3.3.7 Dead time

Dead time of a detector is defined as the minimum time interval that two consecutive counts must be separated in order to be recorded as two different events. Within this time interval, detector will not accept the next incoming photon because the pulse processor is processing the one that has arrived earlier. According to the Orbis µXRF manufacturer, the optimal dead time for application is between 30 – 50% [EDAX, 2009]. Exceeding this range might lead to pile up peak or sum peak. Sum peak occurs when two photons arrive simultaneously at the detector so that it cannot recognise them as two events. Therefore the new peak created and measured is the sum of two X-ray energies. At dead times below this optimal range, low backlog of photons will

occur that is the low accumulation of photons emitted by sample and are waiting to be processed by detector. This condition is inefficient and therefore not desired.

3.3.8 LOD at optimum operating conditions

The sample used was P_{CEMI}-0.4-28d-0.50% Cl^-. For the determination of the LOD of chloride, the beam voltage was 40 kV. Time constant and beam size was 12.8 µs and 30 µm respectively. The analysis was carried out in vacuum chamber with the application of the 25 µm aluminium filter. Beam current was adjusted to 150 µA to reach a dead time of 40%. Figure 3-16 shows the SNR and LOD for chloride at 50, 500, 3000, and 6000 s live time. Each point is an average of ten measurements except the point at 6000 s for both SNR and LOD for chloride which is an average of eight measurements. The error bars represent the standard error for the mean value.

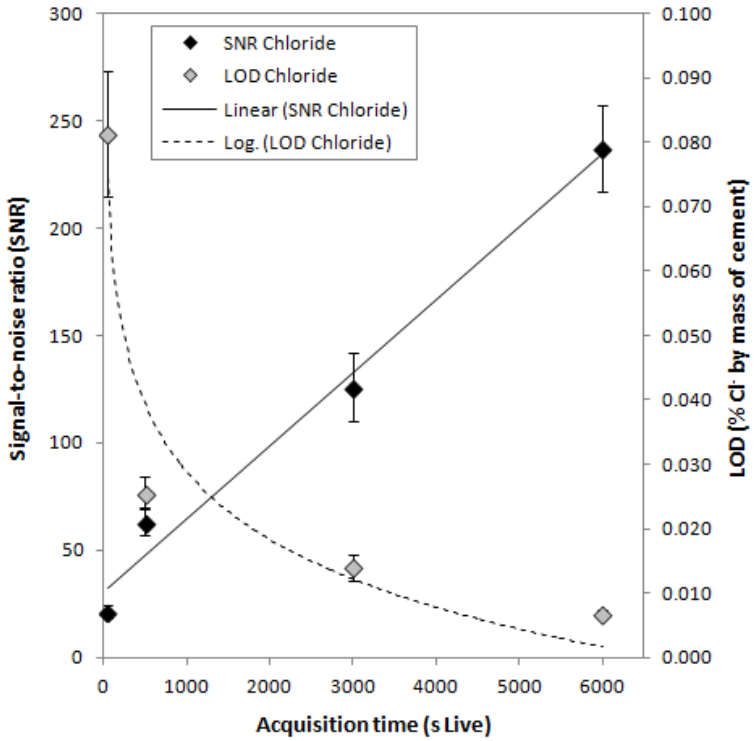


Figure 3-16: SNR and LOD of chloride at optimum operating conditions in P_{CEMI}-0.4-28d-0.50% Cl^-.

As seen in Figure 3-16, increase in the acquisition time results in an increase in the SNR for chloride peak. The greater the SNR the lower will be the LOD of chloride in

the sample. Due to time constraints, the experiment was ended at 6000 s live time. At 6000 s, the LOD of chloride is 0.007% by mass of cement which is equivalent to 70 ppm. This is in close agreement with the LOD of chloride reported by Labutin et al. [2014] which was 50 ppm using double-pulse laser-induced breakdown spectroscopy (LIBS) under ambient conditions. Using the same technique, Wilsch et al. [2005] achieved a limit of detection of 0.15% chloride by mass of cement which is equivalent to 1500 ppm. Silva et al. [2013] reported a limit of detection <0.05% by mass of cement (<500 ppm) using laser ablation inductively coupled plasma mass spectrometry (LA-ICP-MS).

For the determination of the LOD of sulphur, filter was not employed since sulphur peak does not overlap with rhodium Rayleigh scatter peak. Beam current was adjusted to 75 μA to achieve a dead time of 40%. The rest of the operating parameters were identical to those employed for the determination of the LOD of chloride. Figure 3-17 shows the SNR and LOD for sulphur at 50, 500, and 3000 s live time. Each point is an average of ten measurements. The error bars represent the standard error for the mean value.

Due to time constraints, the experiment was ended at 3000 s live time. At 3000 s, the LOD of sulphur is 0.003% by mass of cement which is equivalent to 30 ppm. This is significantly lower than the LOD of sulphur by double-pulse laser-induced breakdown spectroscopy (LIBS) which was 1500 ppm [Labutin et al., 2014].

Therefore, the sensitivity of μXRF to chloride and sulphur greatly improves with longer acquisition time. However, this comes at the cost of longer analysis period. For example, at an acquisition time of 50 s Live, the time needed to complete a single spot analysis is approximately 2 minutes. At 3000 s Live and 6000 s Live, the corresponding time required is 1.5 and 2.5 hours respectively. It is therefore at the discretion of the analyst to decide what level of sensitivity and corresponding acquisition time is appropriate for a particular application. For example, the LOD for chloride content should be comfortably below the threshold value for corrosion initiation, which is typically 0.1 to 0.4% by mass of cement. Based on Figure 3-16, an LOD for chloride content of 0.05% by mass of cement can be obtained at an acquisition time of approximately 250 s.

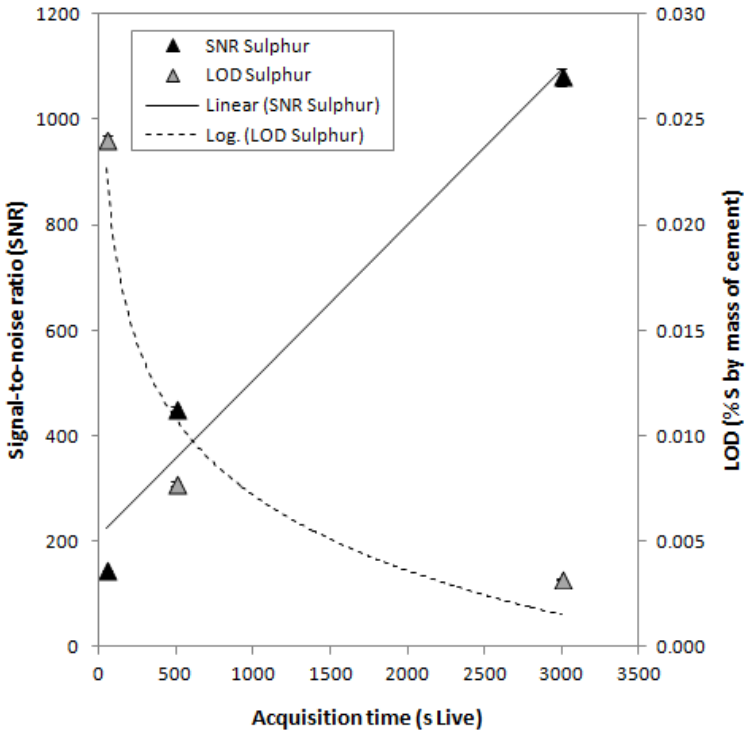


Figure 3-17: SNR and LOD of sulphur at optimum operating conditions in PCEMI-0.4-28d-0.50% Cl^-.

3.4 Conclusions

There are at least seven main operating conditions in μXRF that affect its sensitivity to chloride and sulphate analysis in cement-based materials. The operating parameters are beam voltage, analysis chamber (air or vacuum), filter, acquisition time, time constant, beam spot size, and dead time. In this Chapter, paste samples with water/cement ratio of 0.4 and chloride contents of 0.15%, 0.50%, and 2.00% by mass of cement were analysed using a range of operating conditions to understand their effects and to establish the optimal set-up.

The results showed that the SNR for both chloride and sulphur were greater at higher beam voltages, particular in the range of 25 – 50 kV. This is due to a shift of the bremsstrahlung radiation to higher energies at these beam voltages, and thus giving a more pronounced chloride and sulphur peaks in the collected spectrum. At lower voltages (10 – 20 kV), the bremsstrahlung radiation shifts to lower energies, obscuring the chloride and sulphur peaks, and therefore degrading the SNR and LOD. Although

analysis can be carried out in ambient environment, it produces a low SNR for chloride and sulphur because the presence of gas molecules in the chamber attenuates the emitted characteristic X-ray fluorescence. Therefore, analysis in vacuum would be recommended to obtain the best SNR and LOD. However, this requires sample pre-drying, which might not be ideal for some applications. For chloride analysis, use of the 25 μm aluminium filter is necessary to remove overlapping rhodium spurious peak that originates from the X-ray tube. However, this filter is not a requisite for sulphur analysis as its ROI does not overlap with that of the rhodium peak.

Another parameter that improved the SNR and LOD for chloride and sulphur analysis was the acquisition time. The results in this Chapter showed that a longer acquisition time gave better SNR and LOD in all cases. It was also observed that a time constant of 12.8 μs was optimum. At this time constant, the chloride and sulphur peaks were sufficiently well resolved and the output count rates were adequate to produce good results. A beam spot size of 30 μm was found to be superior to 1 or 2 mm in terms of improving the SNR and LOD for both chloride and sulphur. This is probably due to the design of the 30 μm poly-capillary which utilises a bundle of 3-5 μm fibres that produces a higher X-ray flux. The optimum dead time for application is 30 – 50%.

The optimum operating condition for the analysis of chloride and sulphur in cement-based materials is summarised in Table 3-2. At the optimum operating condition, the LOD for chloride is 0.007% by mass of cement (70 ppm) at 6000 s live acquisition time and the LOD for sulphur is 0.003% by mass of cement (30 ppm) at 3000 s live acquisition time.

Table 3-2: Optimum operating conditions for the analysis of chloride and sulphur.

Parameter	Detail	Notes
Beam voltage (kV)	25 – 50	
Chamber	Vacuum	Drying of sample would be required if analysis is carried out in vacuum.
Filter	25 μm aluminium for chloride, No filter for sulphur	
Acquisition time (s Live)	Highly variable * 6000s for LOD of 70 ppm (Cl^-) 3000s for LOD of 30 ppm (S)	Dependent on beam voltage, chamber, and filter.
Time constant (μs)	12.8	
Beam spot size	30 μm	For high spatial resolution analysis.
Dead time (%)	30 – 50	Manufacturer's recommendation.

* Sensitivity of μXRF to chloride and sulphur improves with longer acquisition time. However, longer acquisition time may result in a very long analysis period which might be impractical for the typical size of concrete sample for laboratory analysis. It is therefore on the discretion of the analyst whether to focus on high sensitivity which requires longer acquisition time or to focus on short analysis period which degrades the sensitivity.

Some of the findings from this study are consistent with those reported in the literature. For example, analysis in vacuum to minimise absorption of characteristic X-ray fluorescence by gases in the chamber and the use of 25 μm aluminium filter to remove the rhodium spurious peak are in agreement with those reported by Moradllo et al. [2017] and Sudbrink et al. [2017]. However, analysis in vacuum may cause the sample to dry and this could lead to erroneous results for some applications [Snyder et al., 2012]. Longer acquisition time is also reported elsewhere [Ernst et al., 2012] to

improve the SNR and LOD of the element of interest. However, the findings from this Chapter as shown in Figure 3-16 and 3-17 provide the data to enable selection of acquisition time to achieve the required limit of detection for chloride and sulphur based on the intended application.

One of the most interesting findings is the improvement of SNR and LOD for chloride and sulphur at higher beam voltages due to the shift of the bremsstrahlung peak to higher energy levels. Another interesting finding is the optimum time constant at 12.8 μs. Finally, it should be noted that although operating conditions are often presented in the literature [Sutter et al., 2009; Schlegel et al., 2011; Moradllo et al., 2017; Sudbrink et al., 2017], no justification is given on why these values were chosen. This Chapter provides a more comprehensive understanding of the effects of operating conditions on the sensitivity of μXRF, thus enabling its optimisation for analysis of chloride and sulphate in concrete.

Chapter 4 Identification of cement paste and aggregate regions

This Chapter presents a new approach for identifying cement paste regions in mortars and concretes. The method is based on exploiting the changes in dead time when a 30 μm beam samples cement paste or aggregate regions. Using one set of operating condition, the dead time achieved in aggregate particles abundant in silicon, calcium, and iron were in the range of 15-16%, 34-36%, and 41-44% respectively. The dead time achieved in cement pastes with different w/c ratio and curing age were in the range of 28-32%. The paste regions identified using this approach was comparable to those identified by conventional elemental mapping. However, the proposed method is much quicker and easier to implement compared to elemental mapping. This Chapter also investigates the effects of four operating parameters (beam spot size, beam voltage, amplifier time constant, and dwell time) on the quality of elemental mapping. A beam spot size of 30 μm was superior to 1 or 2 mm in terms of producing well-resolved elemental maps. Beam voltage and amplifier time constant had insignificant effects, however there was a slight improvement in the clarity of calcium and silicon maps at higher dwell times (> 200 ms).

4.1 Introduction

Aggressive species such as chloride and sulphate penetrate concrete mainly through the pore structure inherent in the hydrated cement paste and cracks caused by tensile stresses [Müller, Breiner, & Anders, 2013]. Transport occurs predominantly through the paste matrix since it envelops aggregate particles and it is an interconnected phase that has high porosity [Buenfeld et al., 1998]. Aggregates in normal weight concrete are relatively dense compared to cement paste and so do not hugely contribute to the transport process [Wong et al., 2009; 2012; Zheng et al., 2009].

Therefore, the cement paste region is of most interest in studying transport processes using μXRF. Furthermore, aggregates may or may not contain naturally occurring chloride. Therefore, the inclusion of aggregates in μXRF analysis will lead to uncertainties and potential errors in the determination of chloride ingress or chloride content in a sample. By avoiding the aggregates, these effects could be minimised. Based on these, the ability to identify and separate cement paste regions from

aggregate particles in concrete during μXRF analysis is important as it will aid the analyst to locate sampling points to avoid interference of signals from aggregate particles and allow measurements to be made solely on cement paste or aggregate particles.

One potential way to achieve this is through elemental mapping [Sutter et al., 2009]. Essentially, this produces a series of images that shows the spatial distribution of the elements present on the sample surface. These element maps can then be used to differentiate the various phases in concrete. For example, calcium is present in abundance in the cement paste matrix. If the concrete is made of siliceous aggregates, then mapping the distribution of calcium and silicon would aid in identifying paste and aggregate regions in the sample. However, this approach is very time-consuming if one wishes to analyse a large area and may be difficult to implement for concretes that contain calcareous aggregates or complex multi-mineral aggregates.

The aim of this Chapter is to develop a simple approach for identifying cement paste regions in concrete. Two methods will be assessed. The first method is based on conventional elemental mapping followed by image processing and analysis to enhance the contrast between different features (coarse and fine aggregates, cement paste) in a sample. This work was carried out in collaboration with an MSc student [Ho, 2013]. The second method is a new approach based on measuring dead time. The advantages and disadvantages of both methods will be assessed.

4.2 Elemental mapping

4.2.1 Acquisition of elemental maps

Three concrete samples with different aggregate types were tested. Sample 1 had limestone aggregates (5 - 10 mm) as the coarse aggregate, while Sample 2 and 3 had Thames Valley gravel (4.75 – 12 mm) and lightweight aggregate (Lytag 8/12 and 4/8) respectively. All samples were made with the same binder type (CEM I) at the same water/cement ratio (0.5). Silica sand was used as the fine aggregate. Total aggregate volume fraction for all samples were about 70%. Sample 1 and 3 contained one reinforcing steel of 10 mm diameter.

For each mapping, the sample was positioned on the plexiglas stage and secured using blu-tack. The stage Z-axis was then adjusted so that the sample is in sharp focus under the low magnification (10×) and high magnification cameras (70×). Subsequently, a suitable beam spot size, beam voltage, amplifier time and dwell time is selected (Chapter 4.2.2). The value of the optimum dead time (Dtm) is adjusted by varying the beam current so that the recommended optimal dead time range (30-50%) is achieved. Several spot analyses were carried out on aggregates particles and cement paste regions in order to identify all elements present in the sample to facilitate mapping. Subsequently, all peaks in the generated spectrum were identified using the peak identification function in the Orbis Vision software and false peaks (escape, sum) removed. Finally, the area to be mapped was defined and the mapping process was carried out. Typically, maps were generated for the following elements: sodium, magnesium, aluminium, silicon, sulphur, chloride, potassium, calcium, manganese, and iron. Mapping an area of 11.4 x 8.9 mm using a 30 μm beam usually required about 5 hours for completion.

Each elemental peak has its own region of interest (ROI). As an example, the ROI for silicon and calcium are channels 165 – 182 and 359 – 379 respectively. Photons within channels 165 – 182 are categorised as silicon characteristic X-ray fluorescence and thus forming silicon peak while those in channels 359 – 379 are considered as calcium characteristic X-ray fluorescence and thus forming calcium peak. This is the principle of the peak identification function provided in the software. The steps for peak identification are explained in the EDAX Orbis Vision User's Manual [2009]. However not all peaks are elemental peaks. In X-ray measurements, there are several artefact peaks which might present in the spectrum besides the elemental peaks. Sum peak and escape peak are two false peaks which originate from the detection process while Rayleigh and Compton scatter are false peaks which arise from the X-ray tube source. Sum peak occurs when two photons arrive simultaneously at the detector so that the detector could not recognise them as two different events. Escape peak is a peak with energy of 1.74 keV less than its original energy. In the Orbis Vision software (Ver. 2.101), the theoretical locations of possible sum peaks can be identified with a marker but could not be corrected. The software however is capable of identifying and subtracting escape peaks from the spectrum. Rayleigh and Compton scatter peaks can be identified and Rayleigh Rh L to mention the least can be removed from the spectrum

by means of the thin aluminium filter. These four spurious peaks were explained in detailed in Chapter 2.

4.2.2 Parametric study

A parametric study was carried out to determine the optimal μXRF operating conditions needed to produce good quality elemental maps. The main parameters investigated were beam spot size (30 μm, 1 mm, and 2 mm), beam voltage (10, 20, 30, 40, and 50 kV), amplifier time constant (1.6, 3.2, 6.4, and 12.8 μs), and dwell time (30, 50, 100, 200, 300, and 400 ms). A randomly selected area of 11.4 mm × 8.9 mm from a concrete sample containing Thames Valley gravel was chosen for the parametric study. The selected area is shown in Figure 4-1 and this was obtained by aligning and merging 5 × 5 images captured using the high magnification camera (70x).

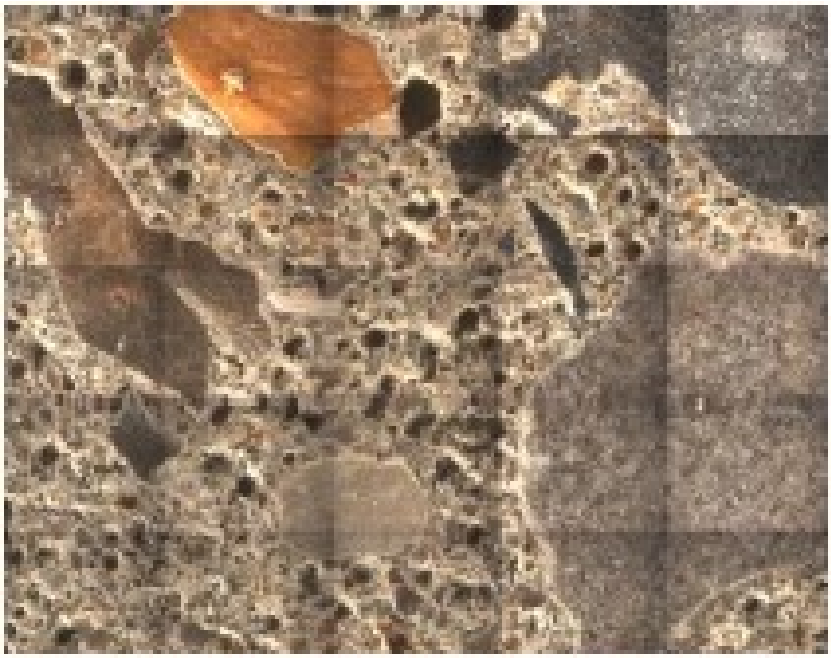
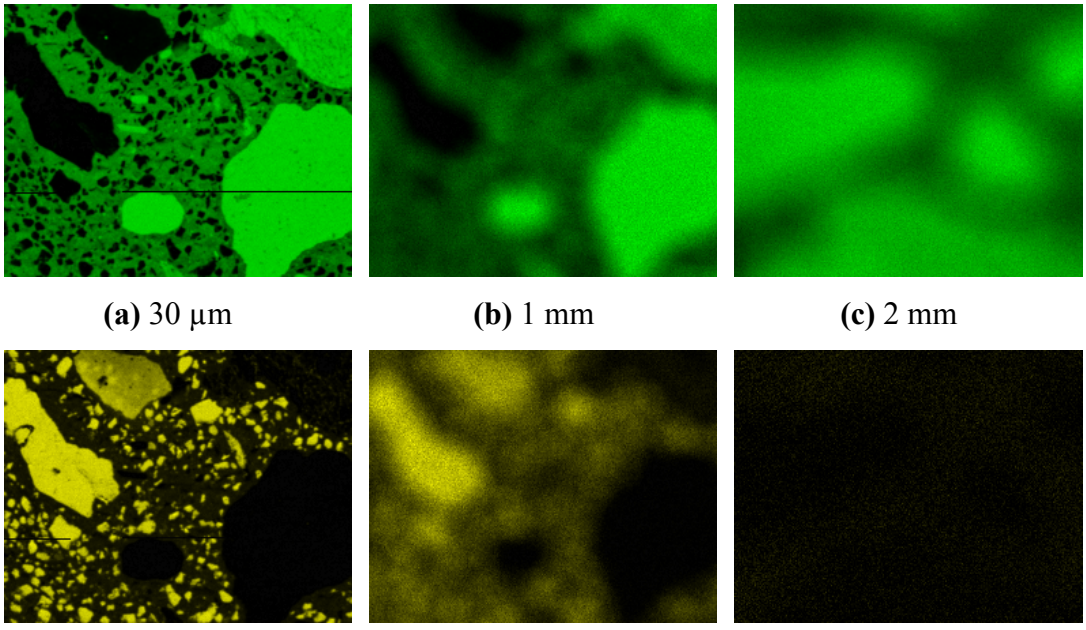


Figure 4-1: Randomly selected area of a concrete sample for parametric study (Field of view: 11.4mm×8.9mm).

a) Beam spot size

Figure 4-2 shows the effect of beam spot size on the quality of the obtained calcium and silicon maps of the area shown in Figure 4-1. Beam voltage and beam current used was 25 kV and 100 µA respectively. The analyses were run in vacuum chamber with the time constant of 12.8 µs, dwell time of 300 ms and matrix size of 256×300 pixels. Spot analyses was carried out to identify the elements present prior to mapping using an acquisition time of 100 s live.



(a) 30 µm **(b)** 1 mm **(c)** 2 mm

(d) 30 µm **(e)** 1 mm **(f)** 2 mm

Figure 4-2: Effect of beam spot size on the captured calcium map (a, b, c) and silicon map (d, e, f) of the concrete sample shown in Fig 4-1.

As seen in Figure 4-2, the highest spatially resolved calcium and silicon maps were obtained when the 30 µm beam spot was employed. The quality of elemental mapping degraded at larger beam sizes (1 mm and 2 mm) with loss in spatial resolution, feature contrast and signal quality. This is partly because a larger beam size increases the possibility of sampling more than one phase and therefore blurring of phase boundaries. Furthermore, the Orbis µXRF uses collimating X-ray optics to convert highly divergent X-rays to form the 1 or 2 mm beam. X-rays entering the collimating tube reflect off the inner surface and lose energy at each reflection point. Therefore, highly energetic photons will transmit, but lower energy photons will be attenuated due to energy lost at each reflection. These collectively lead to a lower X-ray flux for

the 1 and 2 mm beam and poor signal to noise ratio as seen in Figure 4-2 (b), (c), (e), and (f). In contrast, the Orbis μXRF uses poly-capillary optics that consists of a bundle of fibres of 3-5 μm diameter to achieve the 30μm beam spot. It adopts the principle of total internal reflection (TIR) based on Snell's law to guide X-rays with minimal loss of energy, therefore producing high X-ray flux and clearer elemental maps as shown in Figure 4-2 (a) and (d).

b) Beam voltage

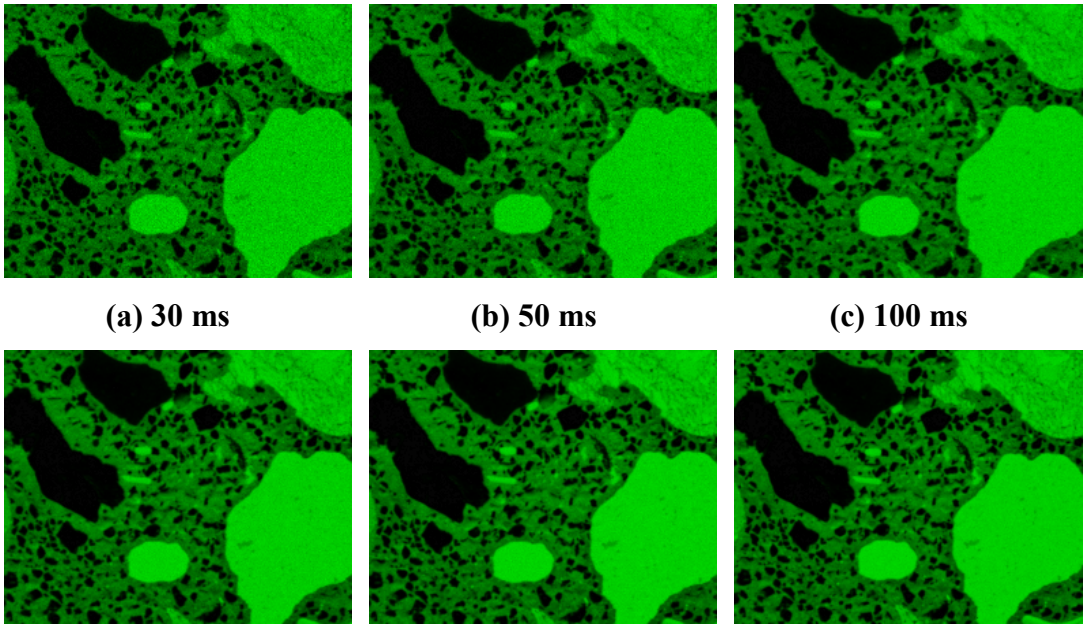
Varying the beam voltage between 10 and 50 kV had an insignificant effect on the quality of the calcium and silicon elemental maps. Here, the beam spot size was 30 μm and all other operating parameters employed were identical to that in section 4.2.2a. This is because the smallest beam voltage used (10 kV) is already more than sufficient to excite the elements present to cause the emission of characteristic X-ray fluorescence. The K-edge energy, which is the energy required to eject an electron from the K shell of an atom to emit its characteristic X-ray, is 4.034 keV and 1.840 keV for calcium and silicon respectively. As mentioned in Chapter 3, the bremsstrahlung radiation will be centred at lower energies for beam voltages < 15 kV and at higher energies for beam voltages > 40 kV. Regardless of the location of the bremsstrahlung radiation, it would not obscure these strong elemental peaks. Therefore, the use of beam voltages in the range of 10-50 kV does not have obvious effect on the quality of the maps.

c) Time constant

Similarly, the quality of calcium and silicon maps appeared to be similar for all values of time constants tested (1.6 to 12.8 μs). This appears to contradict findings from Chapter 3 showing that chloride peak was better resolved with higher SNR at 12.8 μs time constant compared to at 1.6 μs. However, the chloride content in the sample was only 0.50% by mass of cement which is very low relative to that of calcium or silicon. Since calcium and silicon are presence in abundant quantities in paste matrix, calcareous aggregates and siliceous aggregates, their peaks are well resolved even at very short time constant of 1.6 μs. The use of higher time constants therefore had insignificant effect on the quality of the calcium and silicon maps.

d) Dwell time

Dwell time is defined as the time spent at one location for detecting characteristic X-ray signals and so it is identical to acquisition time (Section 2.5.5). The main difference is that the dwell time is the term used for mapping, while acquisition time is used for spot analyses. Figure 4-3 shows that increasing the dwell time had little effect on the quality of calcium map. When viewed at higher magnifications, it can be seen that longer dwell times (such as 200, 300, and 400 ms) improved the clarity of the calcium maps slightly compared to those obtained at shorter dwell times (30 and 50 ms). This is because the longer the time spent for detecting X-ray photons at one spot, the greater will be the SNR for the element (Chapter 3) and hence clearer maps. However, the improvement is small for elements that are present in abundance, such as calcium and silicon. Furthermore, the use of large dwell time will incur a penalty of very long mapping time, which is impractical for routine analysis of concrete samples.



(a) 30 ms **(b) 50 ms** **(c) 100 ms**

(d) 200 ms **(e) 300 ms** **(f) 400 ms**

Figure 4-3: Effect of dwell time on the obtained calcium map for the concrete sample shown in Fig 4-1.

In summary, the parametric study found that a 30 μm polycapillary beam produced the best quality element maps. However, beam voltage, amplifier time constant and dwell time did not significantly influence the mapping within the range of values investigated. Beam voltage should be sufficiently large to excite the elements present (i.e. greater than the K-edge energy of each element). Dwell time should be selected to consider a compromise between the size of the sample to be mapped, the obtained SNR and total analysis time. Generally, a dwell time of 100ms is appropriate for a concrete sample to give a good balance between quality and the amount of time spent.

4.2.3 Composite element map via image analysis

The obtained elemental maps from each sample were combined to produce a composite image via image analysis by applying suitable morphological and mathematical operations. The purpose of this was to improve the contrast between the coarse aggregates, fine aggregates and cement paste matrix, and to facilitate feature segmentation. This was carried out using the image analysis software ImageJ.

For each sample, two composite elemental maps were created. The first type of composite map was produced using the 'Merge Channels' function in ImageJ. This function combines the element maps in RGB in such a way to produce a false colour RGB image with enhanced contrast between the different phases in the sample where each is represented by a different colour. The approach was named as the simple overlay approach. A good contrast is achieved when the different phases of concrete which are coarse aggregates, fine aggregates, paste matrix, as well as any additional materials such as reinforcing bars or spacers can be differentiated based on the different colour of each of the phase.

The second approach is called the composite map approach using the combination of key and trace elemental maps. In this approach, the key elemental maps and trace elemental maps were first identified. In concretes, silicon is the key element in siliceous aggregates while calcium is the key element in both calcareous aggregates and cement paste matrix. Trace element such as manganese may be one of the elemental components in aggregates. An example of manganese elemental map is shown in Figure 4-4.

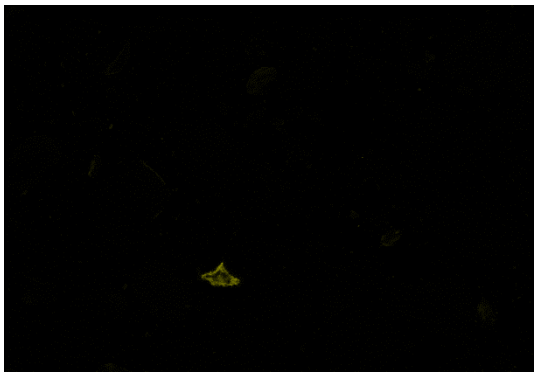


Figure 4-4: Example of manganese trace elemental map.

The first composite map was then created by overlapping silicon maps with trace elemental maps. Figure 4-5 shows a flowchart demonstrating the steps to obtain the first composite image. Subsequently, second composite image was created by subtracting the first composite map from calcium map. Figure 4-6 shows a flowchart demonstrating the steps to obtain the second composite image.

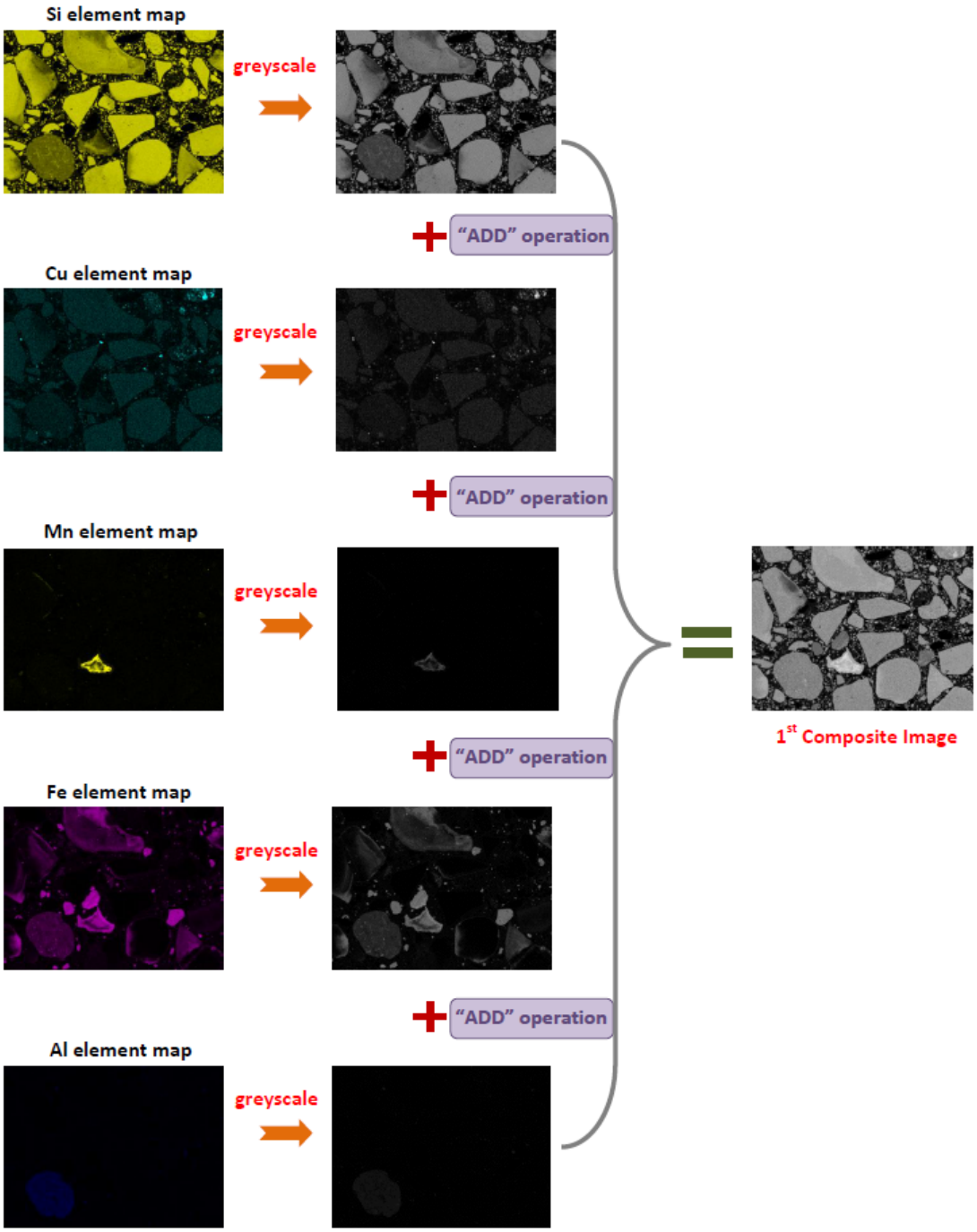


Figure 4-5: Flowchart demonstrating the steps to obtain the first composite image [Ho, 2013].

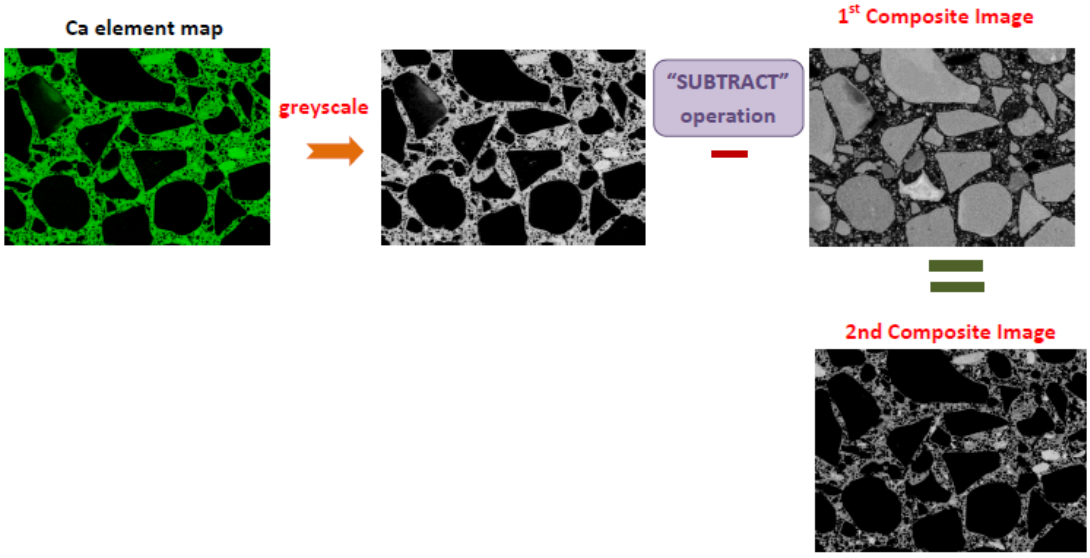
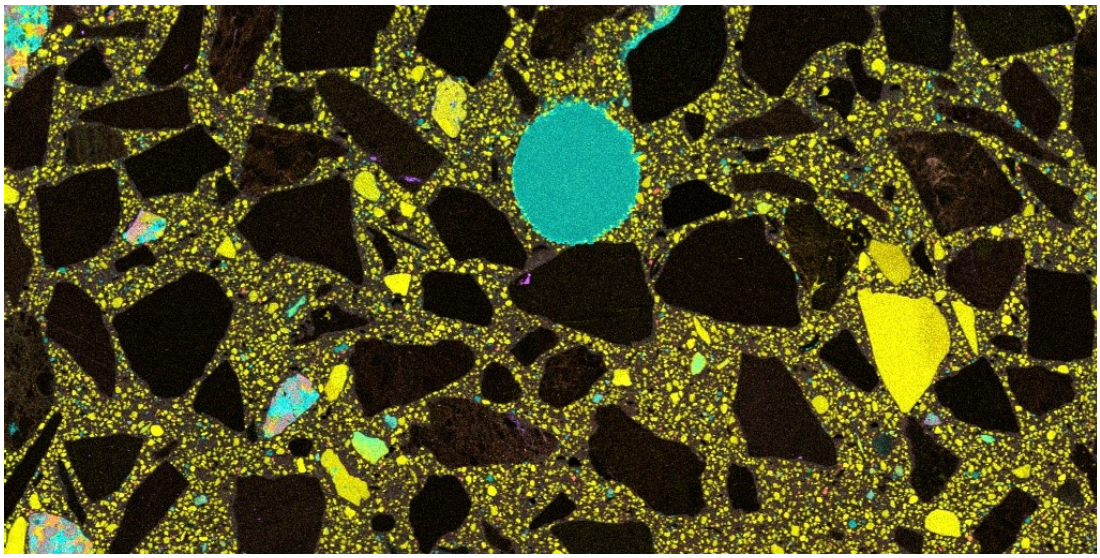


Figure 4-6: Flowchart demonstrating the steps to obtain the second composite image [Ho, 2013].

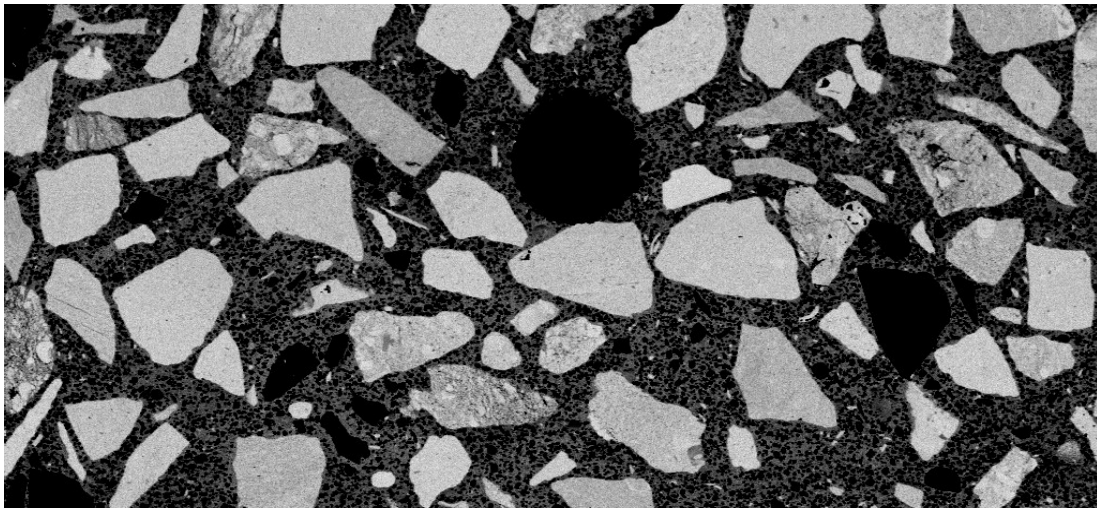
4.2.4 Results

Figure 4-7 shows the composite images obtained for Sample 1 (limestone coarse aggregates). The analysis was carried out in vacuum chamber using 25 kV beam voltage, 30 µm beam spot size, 25.6 µs time constant and 100 ms dwell time. The matrix size was 1024×512 pixels. Figure 4-7 (a) shows the results of the simple overlay "merge channel" approach. Here, the silicon and iron maps were overlaid to produce a composite image where the black particles represent coarse aggregates, bright yellow particles represent the siliceous fine aggregates, multicolour particles represent aggregates with complex mineralogy, the cyan circle represents the rebar and the grey matrix represents the cement paste.

Figure 4-7 (b) shows the result obtained using the second approach of combining key and trace element maps. Here, the greyscale maps of Si, Fe, Cl, Mn, K and Ti were first added and the result of that was then subtracted by the Ca map. This produces a composite image where bright particles represent the coarse aggregates (limestone), black particles represent the rebar and fine aggregates (silica sand), and the grey matrix represents the cement paste.



(a)

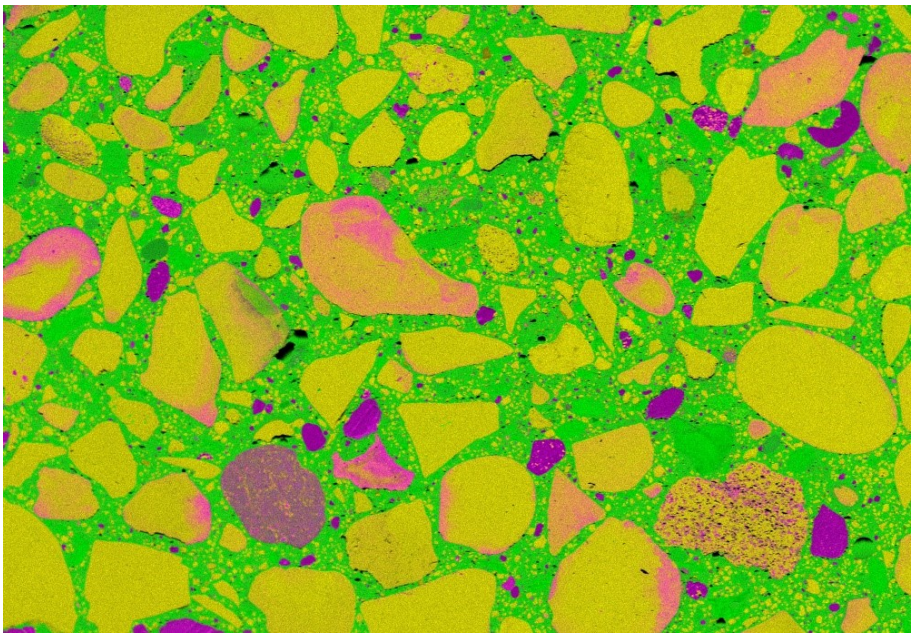


(b)

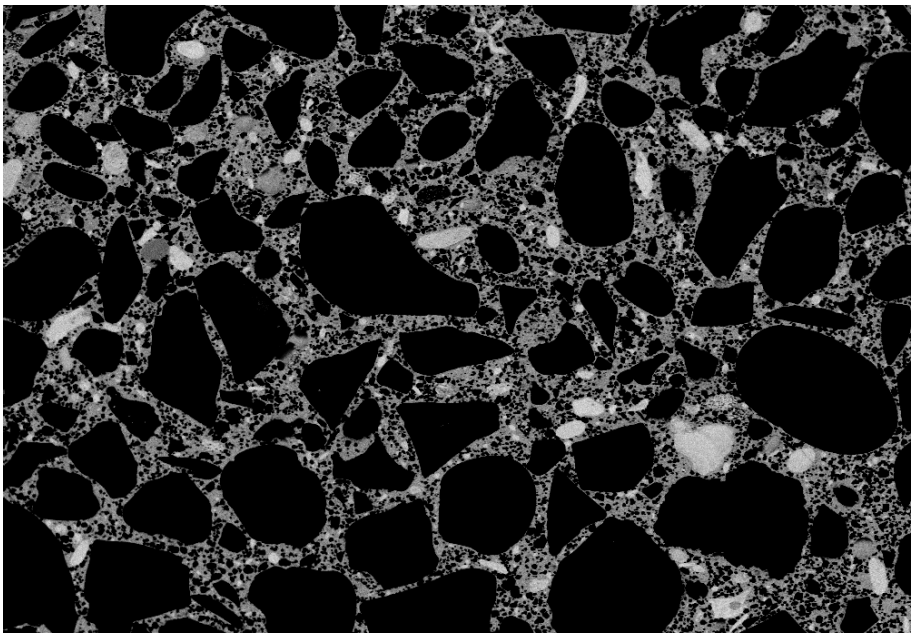
Figure 4-7: Concrete sample 1 with limestone coarse aggregates: (a) simple overlay approach using "merge channels" function, and (b) composite map approach using combination of key and trace element maps. Field of view = 95.11 mm × 42.72 mm.

Figure 4-8 shows the composite images obtained for Sample 2 (Thames Valley aggregates). The operating condition employed was identical to the one used for Sample 1 except that a matrix size of 1000×691 pixels was used for a smaller sample. The image analysis procedures used are also essentially the same as in Sample 1, but a slightly different set of elements were used to enhance contrast. Figure 4-8 (a) was obtained by merging the maps for Al, Si, Ca, Fe, K and Mn. The composite image show the siliceous aggregate particles represented by yellow pixels, while iron rich aggregates are represented by purple pixels and cement paste matrix by green pixels. Figure 4-8 (b) shows the result obtained by combining the greyscale maps of Si, Fe,

K, Mn, Ti, Al and Cu, and then subtracting with the Ca map. The resultant composite image shows siliceous aggregates represented by black pixels, calcareous aggregates represented by the bright light grey pixels and cement paste represented by the dark grey pixels.



(a)

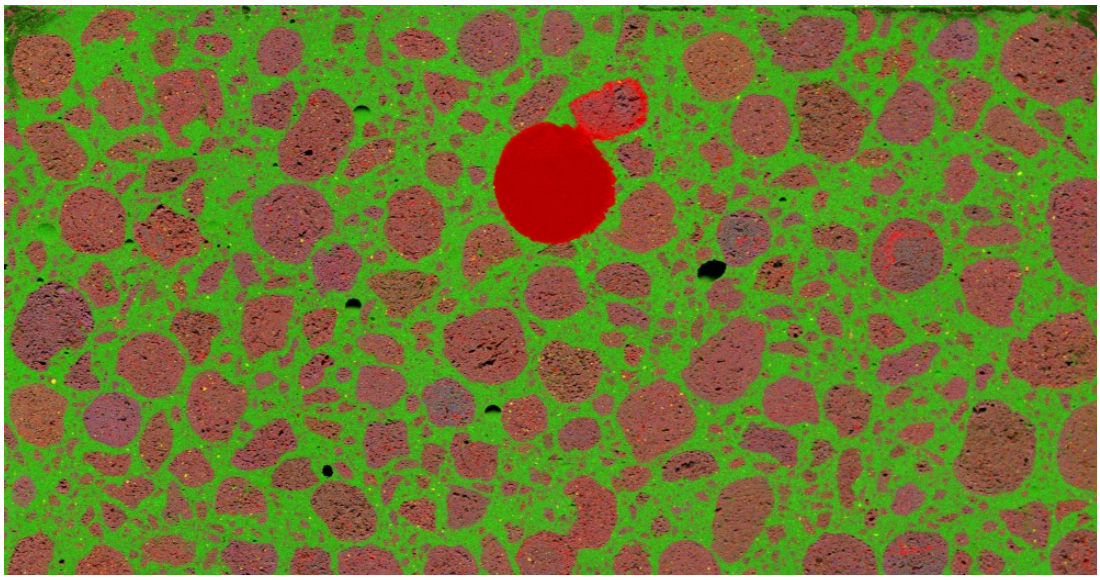


(b)

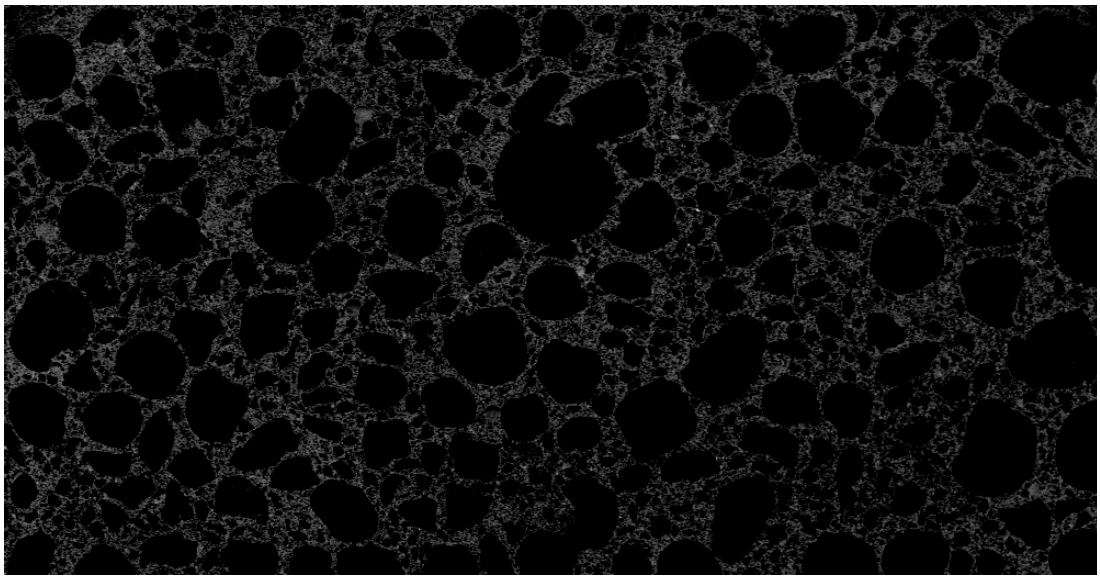
Figure 4-8: Concrete sample 2 with Thames Valley aggregates: (a) simple overlay approach using "merge channels" function, and (b) composite map approach using combination of key and trace element maps. Field of view = 80.14 mm × 55.40 mm

Figure 4-9 shows the composite images obtained for Sample 3 containing Lytag lightweight coarse and fine aggregates, using image analysis procedures very similar to those employed on Sample 1 & 2. In this example, element maps were collected in vacuum using 30 kV beam voltage, 30 μm beam spot size, 6.4 μs time constant and 100 ms dwell time. The matrix size was 1000×549 pixels. Figure 4-9 (a) shows the composite image obtained using the simple overlay approach of merging calcium and iron maps. The purplish-pink pixels represent lightweight aggregates, while the light green pixels represent cement paste and red circle represents the rebar. Figure 4-9 (b) shows the result obtained by combining the greyscale maps of Si, Cr, Cu and Fe, and then subtracting with the Ca map. The resultant composite image shows the lightweight aggregate particles represented by black pixels and cement paste represented by the light grey pixels.

The results show that satisfactory contrast between the different phases in concretes can be achieved by combining the element maps using either the simple overlay "merge channels" approach or the composite map approach using combination of key and trace element maps. However, mapping a representative size of concrete sample is a time-consuming process. Furthermore, the post-processing of the element maps also takes time and requires a somewhat trial-and-error approach in selecting the suitable set of element maps to achieve a good contrast between the phases of interest. Therefore, a new approach for identifying cement paste and aggregate particles based on dead time is developed in the subsequent section. This approach is substantially quicker than element mapping and possibly less prone to errors.



(a)



(b)

Figure 4-9: Concrete sample 3 with Lytag lightweight aggregates: (a) simple overlay approach using "merge channels" function, and (b) composite map approach using combination of key and trace element maps. Field of view = 99.63 mm × 51.70 mm

4.3 Dead time method

4.3.1 Background

In μXRF, the detector receives a series of incoming characteristic X-ray photons from the sample, processes and classifies each photon according to its energy level. This process is schematically represented in Figure 4-10. The dead time of a detector is defined as the time interval after the receipt of an X-ray photon that the detector is unable to record another X-ray photon. It can also be defined as the time interval that two consecutive X-ray photons must be separated in order to be recorded as two different events [Bécares & Blázquez, 2012]. Within this time interval, the detector will not accept another incoming photon because the pulse processor is processing the one that has arrived earlier. Dead time is often expressed as a percentage of rejected X-ray photons over the total incoming photons. This is shown in Equation 4-1, where R_{in} and R_{out} are the input and output count rates respectively.

$$Dead\ time\ in\ \% = (1 - \frac{R_{out}}{R_{in}}) \times 100\% \qquad \textbf{Eq. 4-1}$$

For a particular system and operating condition, the magnitude of dead time is a function of the input count rate [Potts, 2004]. Dead time increases with increase in input count rate because as more X-rays enter the detector, a higher proportion of the incoming X-rays is rejected. However, the input count rate depends on the type and quantity of elements analysed. Generally, input count rate increases with increase in atomic number. This is because X-rays are attenuated as they pass through matter and the degree of attenuation depends on the depth of penetration. The higher the atomic number, the shallower the X-ray penetration depth and less attenuation occurs.

As such, dead time is also expected to be dependent on the elements that are present in a particular phase and it should increase with increase in atomic number. It is this feature that we will exploit in order to detect and differentiate cement paste regions from aggregate particles. The development and validation of this approach will be presented in the following sections.

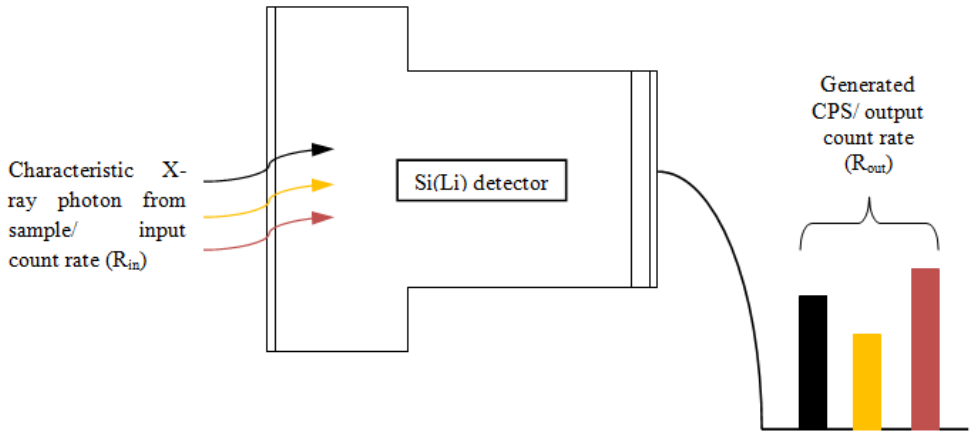


Figure 4-10: Schematic showing input count rate (R_{in}), detector, and output count rate (R_{out}).

4.3.2 Samples

Two series of samples were prepared using ordinary Portland cement complying with BSEN 197-1-CEM I. The Blaine specific surface area and specific gravity of the cement were 342 m^2/kg and 3.15 respectively.

Series I consists of five neat cement pastes with w/c ratios of 0.25, 0.30, 0.35, 0.40, and 0.50. Mixing was done using a bowl mixer. Samples were cast in plastic cylindrical moulds (58 mm diameter, 49 mm height) and compacted in two equal layers using a vibrating table. For each layer, the compaction was considered sufficient when no significant air bubbles escaped the surface. The moulds were then capped and sealed with waterproof tape to avoid leakage. Subsequently, the moulds were rotated continuously for 24 hours to avoid bleeding and segregation effects. Then, the samples still in their plastic containers, were wrapped in cling film and sealed in polythene bags at 20^0C until the ages of 3, 7, 28, and 90 days.

Series II consists of three concretes mixes with free w/c ratios of 0.3, 0.4, and 0.5. These contained Thames Valley gravel (5 – 12.7 mm) and sand (< 5 mm) with specific gravity of 2.63 and 2.53 respectively. The total aggregate volume fraction was 70%. The amount of water required to bring the aggregates to saturated, surface-dry condition was determined and added to the batch water to achieve the target free w/c

ratio. A sulfonated naphthalene-based super-plasticiser was employed to improve the workability of mixes with low w/c ratio. The batch water was also corrected for additional water brought in by the admixture. The mixing was done using a pan mixer. The mix was then compacted in three layers in cylindrical moulds (100 mm diameter, 250 mm height) using a vibrating table. The samples were then covered with plastic sheets and wet hessian for the initial 24 h to prevent evaporation. Subsequently, the samples were demoulded and sealed in cling film and polythene bags at 20^0C until the ages of 3, 7, and 90 days.

After reaching the required curing age, the cylindrical sample was sectioned at mid-height using a diamond saw to produce a rectangular block sample (40×20×8 mm) for microscopy. The blocks were then freeze dried to remove pore water and impregnated with low viscosity epoxy (pre-heated to 50^0C and mixed with toluene) using the methodology described by Wong and Buenfeld [2006]. The epoxy impregnated blocks were cured for several days at room temperature to allow adequate hardening of the epoxy. Subsequently, the blocks were ground and polished with diamond at successively finer grit size to a 1/4 μm finish. Cleaning of samples during the grinding and polishing stages was carried out using acetone in an ultrasonic bath.

4.3.3 Dead time measurements

Spot analysis was carried out following the procedures explained in Chapter 3.2.4. The main difference however was in the number of points selected per sample. For neat cement pastes, twenty spots were randomly selected and analysed on each sample. For concrete samples, twenty spots were randomly selected per sample on regions that visually appear to be the cement paste matrix.

In addition, five spots were randomly selected on siliceous, calcareous, and ferrous aggregate to study the effect of aggregate composition on dead time. Spot analyses were also carried in a line scan pattern across aggregate particles and cement paste in order to study on effect of the aggregate-paste interfaces on dead time. Typically, fourteen spots were selected and analysed across each aggregate-paste interface. The distance between two consecutive spots measured from centre to centre was 15 μm,

which is equal to the radius of the X-ray beam. The dead time achieved at each point was then recorded.

The μ-XRF was operated at 15 kV beam voltage, 100 s (Live) acquisition time and 12.8 μs time constant. The analyses were carried out using a 30 μm beam in vacuum chamber with no filter. A dead time of approximately 30% was achieved when this operating condition was applied on pure paste samples. The μXRF measuring condition is presented in Table 4-1. It is important to note that the measured dead time is dependent on the operating parameters. Therefore, it is crucial to employ a consistent set of operating condition throughout this study to ensure changes in dead time is solely due to changes in phase composition and not due to variation in the operating parameters.

Table 4-1: The μXRF measuring condition.

Operating condition	Detail
Beam voltage (kV)	15
Beam current (μA)	105
Chamber	Vacuum
Filter	No filter
Acquisition time (s Live)	100
Time constant (μs)	12.8
Beam spot	30 μm

4.3.4 Data analysis

Dead time fluctuates within a range during the 100 s live acquisition time at each analysed spot. This is because dead time is a function of the input count rate [Potts, 2004] which can fluctuate with time even for the same analysed spot. As such, the midrange dead time was calculated and this was taken to be representative at each location. The midrange value was calculated using Equation 4-2.

$$Midrange\ dead\ time = \frac{Minimum\ dead\ time + Maximum\ dead\ time}{2} \quad \textbf{Eq. 4-2}$$

In some sections, results is reported in the form of dead time and the corresponding net output and net input counts per second (CPS). The net output counts were obtained using the manual background subtraction method as explained in Chapter 3.2.5. The net output count rate for each element was then calculated by dividing the net output counts with the acquisition time (100 s). Finally, the net input count was calculated using Equation 4-1.

4.3.5 Results

The dead times of neat cement paste, cement paste in concrete, aggregate particles and aggregate-cement paste interfaces are presented in this section.

Neat cement paste

Figure 4-11 shows examples of the analysed spots on neat cement pastes. The red circle on each image indicates the sampling point and the size of the 30 μm beam. Figure 4-12 shows the effect of w/c ratio and curing age on the measured dead time for neat cement paste. For each sample, twenty points were measured and the midrange dead times for all points were then plotted. The results show that dead time fluctuated marginally in the range of 28-32% when these samples were analysed.

As seen in Figure 4-12, dead time was mildly affected when pure pastes were analysed and was independent of the w/c ratios and curing ages.

As mentioned previously, dead time is primarily a function of the input count rate. The higher the input count rate the higher will be the dead time and conversely when the input count rate is lower, so is the dead time. X-rays are attenuated to a different degree as they pass through matter. In cement pastes, calcium is the key element and therefore the penetration depth of X-rays from the X-ray tube in paste matrix will probably be almost constant provided the set of measuring condition employed remains the same for all samples. The characteristic X-rays for calcium with energy in the range of 3.688-4.013 keV might also escape each of the paste samples at a constant rate. These equally means the X-rays attenuation in the neat paste samples under study was approximately at the same degree and hence resulted in dead time value centred at 30%.

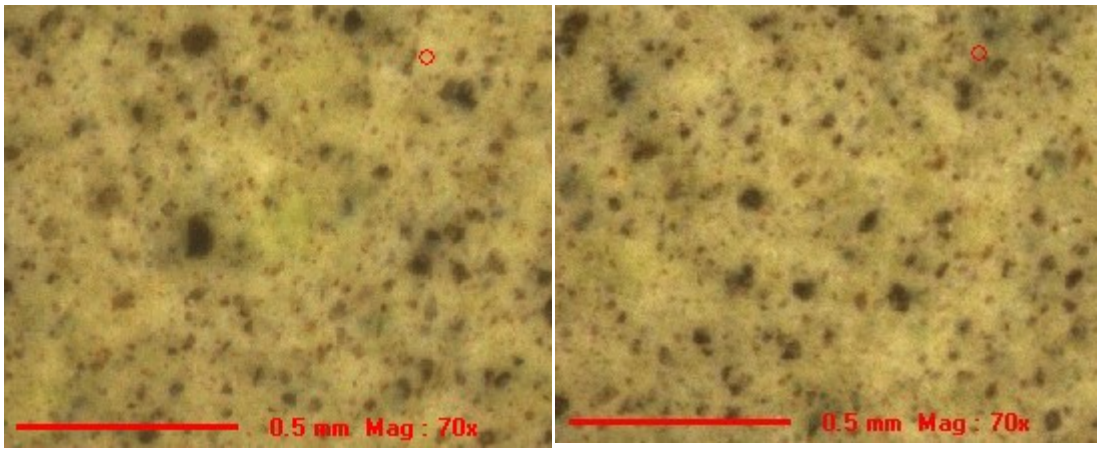
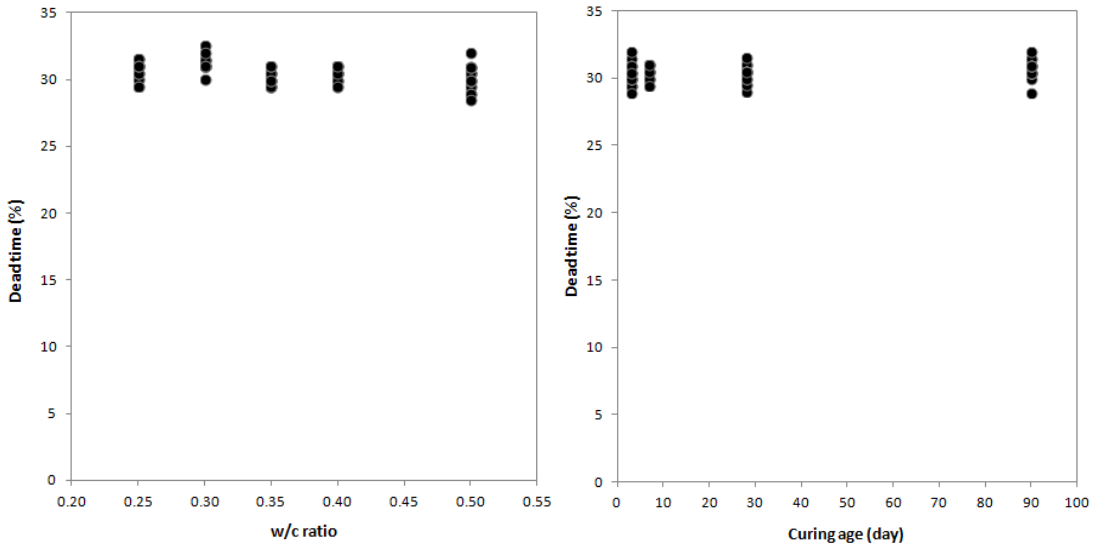


Figure 4-11: Examples of the analysed spots on pure paste samples.



(a) at 7 day curing **(b) at w/c ratio of 0.4**

Figure 4-12: Effect of (a) w/c ratio and (b) curing age on the dead time measured on neat cement pastes.

Cement paste in concrete

The small red circles shown in Figure 4-13 mark examples of analysed points that were selected based on their visual appearance as paste regions in concretes.

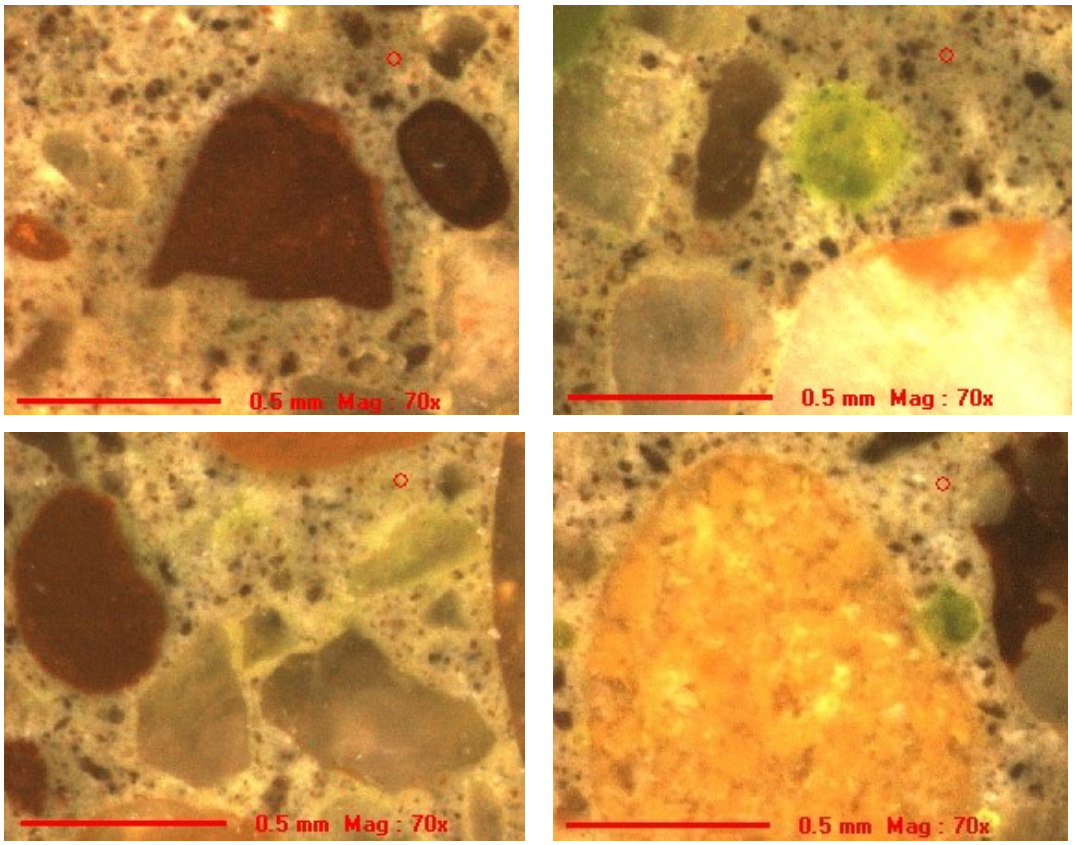
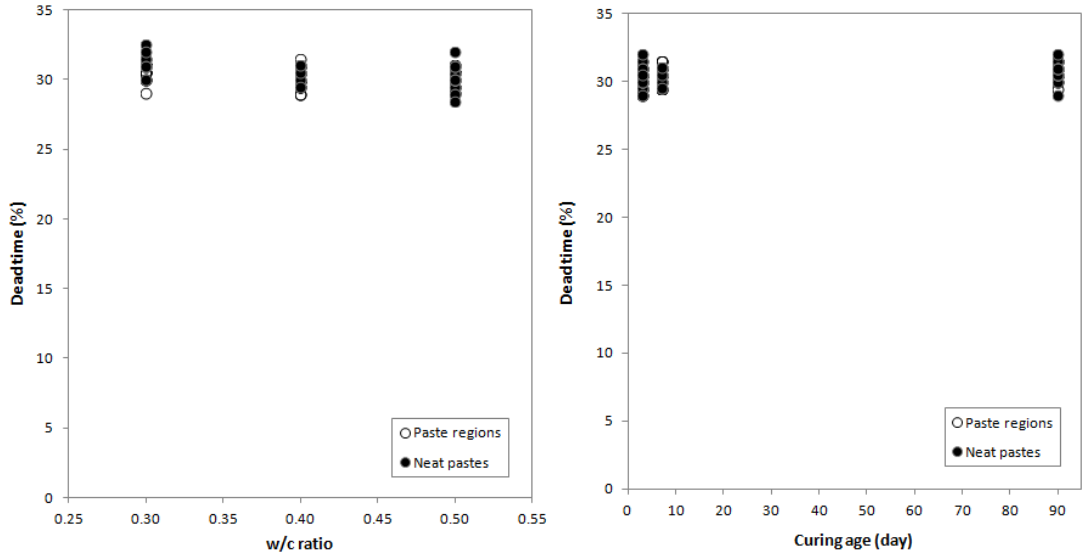


Figure 4-13: Examples of analysed paste matrix in concretes.

The twenty midrange dead times that were measured on concrete samples C_{CEMI}-0.30-3d, C_{CEMI}-0.40-3d, and C_{CEMI}-0.50-3d, were plotted with those achieved in paste samples P_{CEMI}-0.30-7d, P_{CEMI}-0.40-7d, and P_{CEMI}-0.50-7d, respectively. This is shown in Figure 4-14 (a). As seen in the figure, the dead times achieved in paste regions of the concretes were in close agreement with those achieved in neat paste samples. The same results pattern is also observed in samples with different curing age. The twenty midrange dead times achieved in sample C_{CEMI}-0.40-3d, C_{CEMI}-0.40-7d, and C_{CEMI}-0.40-90d were overlapped with those achieved in sample P_{CEMI}-0.40-3d, P_{CEMI}-0.40-7d, and P_{CEMI}-0.40-90d, respectively. This is presented in Figure 4-14 (b).



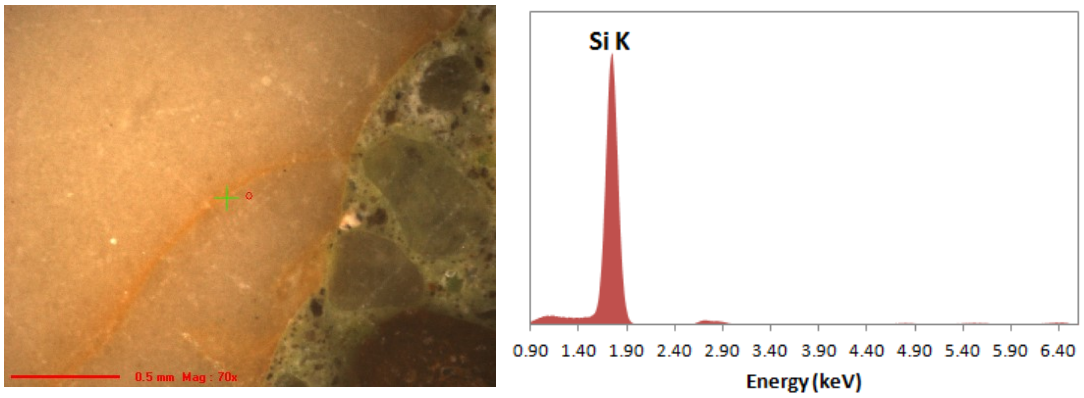
(a) (b)

Figure 4-14: Dead times in neat pastes and paste regions in concretes at different (a) w/c ratio, and (b) curing age.

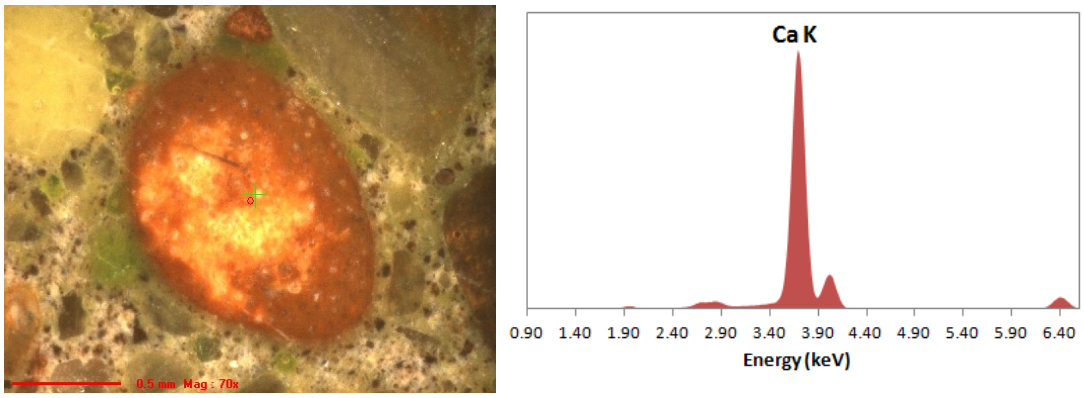
The results thus far show that the dead times achieved in the paste regions of concretes were in close agreement with those achieved in pure paste samples. Therefore the identification of cement paste regions in concretes is possible by means of applying the same set of operating condition used on pure paste samples on the locations visually appeared to be paste matrix in concrete. The locations generating the same dead times as those in pure pastes can then be classified as paste region which contributes to the transport of the deleterious species in concretes.

Aggregate particles

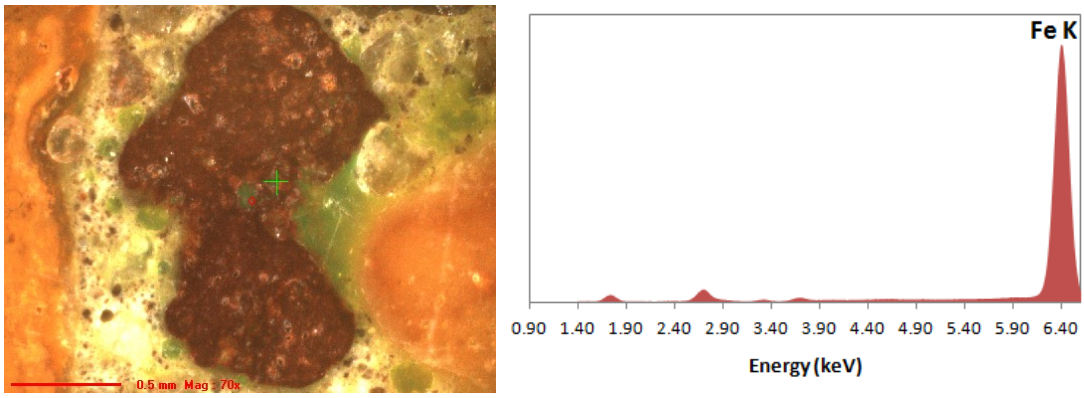
Three types of aggregates were analysed in this study. Aggregates abundant in silicon, calcium, and iron were named siliceous, calcareous, and ferrous aggregates, respectively. Figure 4-15 shows the image and the corresponding spectrum for each aggregate type. Both the tiny red circle and the green crosshair in each image of Figure 4-15 mark a spot in the aggregate under study. The energy range on the x-axis of each spectrum is 0.90-6.60 keV which covers elements from sodium to iron.



(a)



(b)



(c)

Figure 4-15: Image and the corresponding spectrum of (a) siliceous, (b) calcareous, and (c) ferrous aggregate.

From the analyses thus far, dead time of 15-16% was achieved when siliceous aggregates were analysed, dead time of 34-36% was achieved when calcareous aggregates were analysed, and dead time of 41-44% was achieved when aggregates high in iron were analysed. As mentioned previously, dead time is reported in the form of range since it was fluctuating within this range throughout the 100 s live acquisition

time. The atomic number for silicon, calcium, and iron is 14, 20, and 26 respectively. Thus, silicon is the lightest element while iron is the heaviest element in this study according to the periodic table. It is also important to mention the K-edge energy for each of the elements. K-edge energy is defined as the energy required to eject an electron from the K shell of an atom in order for the atom to emit its characteristic X-ray photons. The K-edge energy for silicon, calcium, and iron is 1.840, 4.034, and 7.112 keV respectively.

Figure 4-16 shows the effect of analysing these different aggregate types on the dead times and their corresponding intensities which refers to net output count rate (CPS). Each column is an average of five measurements. The error bars represent the standard error for the mean value.

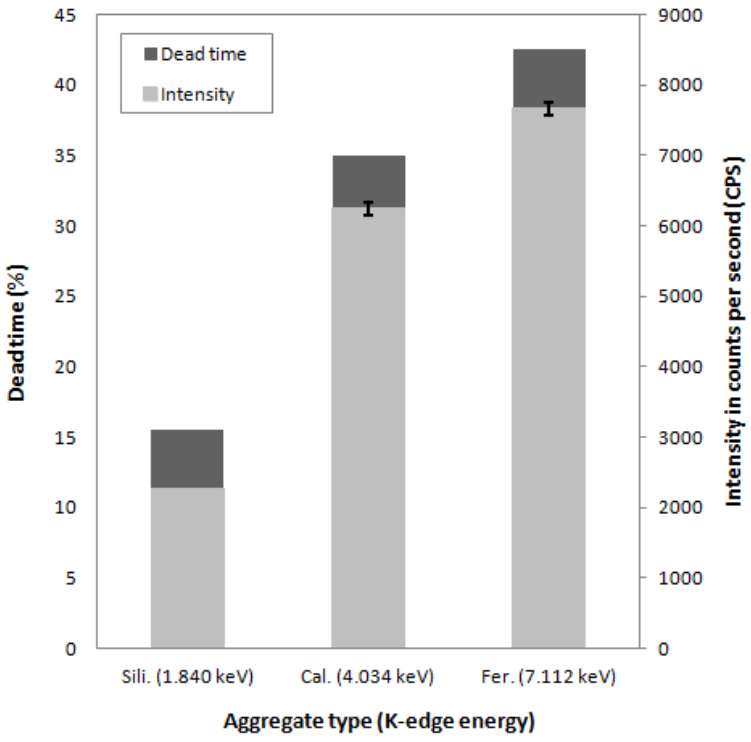


Figure 4-16: Effect of aggregate type on dead time and its corresponding intensity.

The results show that the standard error for dead time is zero for all aggregate type, which is lower than that for neat cement pastes as shown in Figure 4-12. This is due to the fact that the aggregates used in this study are more homogeneous than the cement pastes, thus leading to more consistent measurement of dead times. As seen in Figure

4-16, the higher the K-edge energy of the abundant element in the aggregates, the higher the dead time achieved and output intensity generated. At 1.840 keV which is also referring to silicon in siliceous aggregates, the dead time achieved is between 15-16% and the mean silicon intensity generated is 2275 CPS. At 4.034 keV which is corresponding to calcium in calcareous aggregates, the dead time achieved is between 34-36% and the mean calcium intensity generated is 6246 CPS. At 7.112 keV which is referring to iron in ferrous aggregates, the dead time achieved is between 41-44% and the average iron intensity generated is 7663 CPS. Attenuation of X-rays in matter probably is the explanation for this results pattern.

X-rays are attenuated to a different degree as they pass through matter. This means the intensity of the emergent X-radiations, denoted as I_X, is always less than the intensity of the incoming X-radiations, denoted as I_O. The degree of attenuation of X-rays in matter depends, in part, on the depth of penetration. When X-rays generated by 109 cadmium radioisotope, ^{109}Cd, with an energy of 22.1 keV impinged a piece of pure iron, the penetration depth is equal to 0.07 mm. The same incoming X-ray energy penetrates a piece of aluminium and lead to a depth of 1.65 mm and 0.014 mm respectively [Mercuro et al., 2005]. It can be concluded that the higher the atomic number of an element, the shallower will be the penetration depth of the incoming X-rays.

In Figure 4-16, the higher the atomic number (or K-edge energy) of an element, the higher the count rate generated. Based on the conclusion in the previous paragraph, the penetration depth of X-rays with energy of 15 kV used in this study is the deepest in siliceous aggregates and shallowest in ferrous aggregates. The characteristic X-ray energy for silicon is very low, which is in the range of 1.739 – 1.836 keV. Since the penetration depth of X-rays in siliceous aggregates is the deepest compared to calcareous and ferrous aggregates, both the incoming X-rays from the X-ray tube and the low energy characteristic X-rays for silicon underwent absorption process to a certain degree and therefore reducing the input count rate for silicon detected by the Silicon Lithium, Si(Li) detector. This in turn explains the reason for the dead time achieved while analysing the siliceous aggregates to be the lowest that is between 15-16%.

Data on the input count rate (R_{in}) is not available for μXRF user. However an estimate amount of R_{in} for the abundant element in each of the aggregate type was calculated by plugging in the known dead time and output count rate (R_{out}) values as presented in Figure 4-16 in Equation 4-1. For each aggregate type, the midrange dead time was used for calculation. From the calculation, the input count rate for silicon was approximately 2692 CPS which was relatively low. The detector therefore was switched off less frequently and thus leading to a lower dead time. As mentioned previously, detector will be switched off to allow the pulse processor to analyse each photon separately.

The characteristic X-ray energy for iron is relatively the highest that is in the range of 6.391 – 7.058 keV. Since the penetration depth of X-rays in ferrous aggregates is the shallowest, the incoming X-rays from the X-ray tube underwent less absorption process compared to that in siliceous aggregates. The comparatively more energetic characteristic X-rays for iron also able to escape the sample more easily leading to a high iron input count rate which was approximately 13 327 CPS. This in turn explains the reason for the dead time achieved while analysing ferrous aggregates to be the highest. High input count rate of iron caused the detector to close down more frequently therefore leading to a higher dead time.

Interface between aggregate particles and paste regions

As mentioned in the methodology section, fourteen points were selected in a line pattern across paste region and a siliceous aggregate. However in this results section, only the dead time and corresponding intensity of five points were plotted to produce Figure 4-17. Since few points were located in the same phase and thus generating the same dead times, only one point was selected to represent the analysed phase. In this study, points 1-3 were located in region visually appeared to be paste matrix. The dead times generated at all three points were in the range of 29-30%. To avoid repetition, only data at point 1 was used to plot Figure 4-17. Points 10-14 were located in siliceous aggregate. The dead times generated at these points were in the range of 15-16%. Only data at point 14 was used to plot Figure 4-17. Point 5, 7, and 8 were named Interface 1, 2, and 3, respectively. The dead time achieved at Interface 1, 2, and 3 was in the range of 27-28%, 22-23%, and 18-19%, respectively. Figure 4-17 shows the effect of different regions of concrete on dead times and their corresponding intensities. The

midrange dead time of each region was used to plot the figure while intensity in this context refers to the total net input count rate or the summation of the input count rate of all elements present in each region. Figure 4-18 shows the different regions of concrete and their corresponding spectrum.

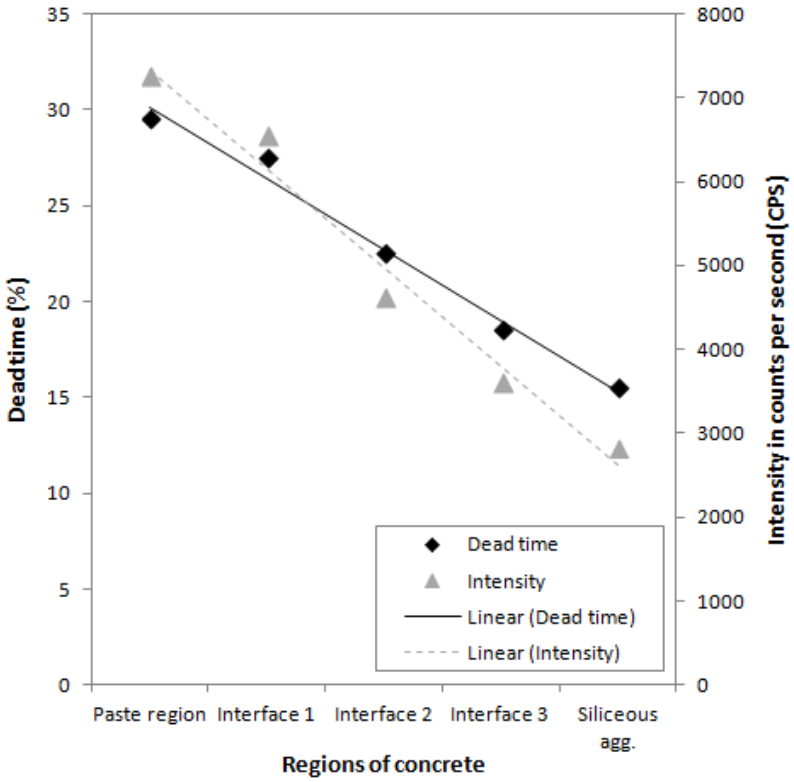


Figure 4-17: Effect of different regions of concrete on dead times and their corresponding intensities.

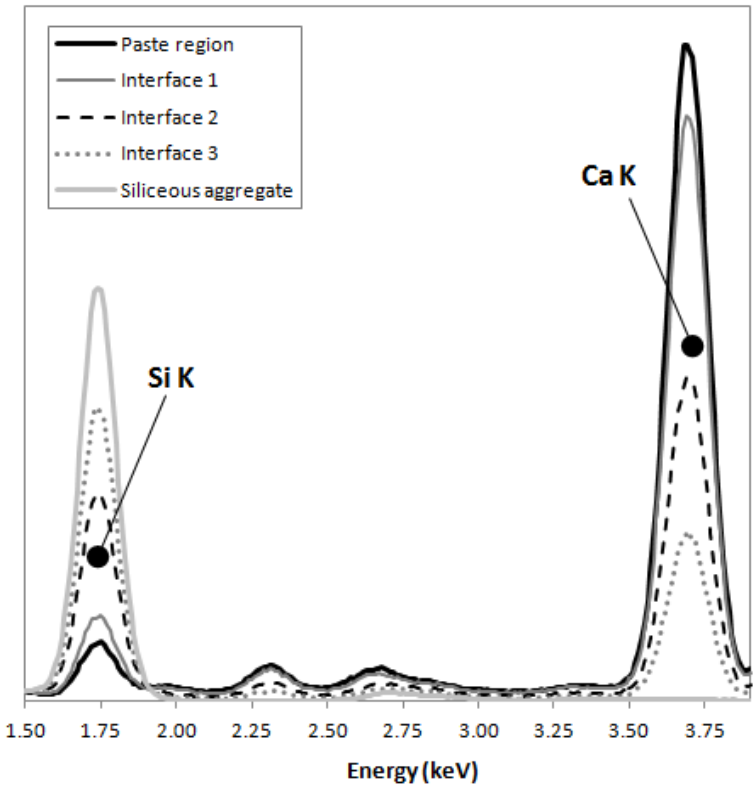
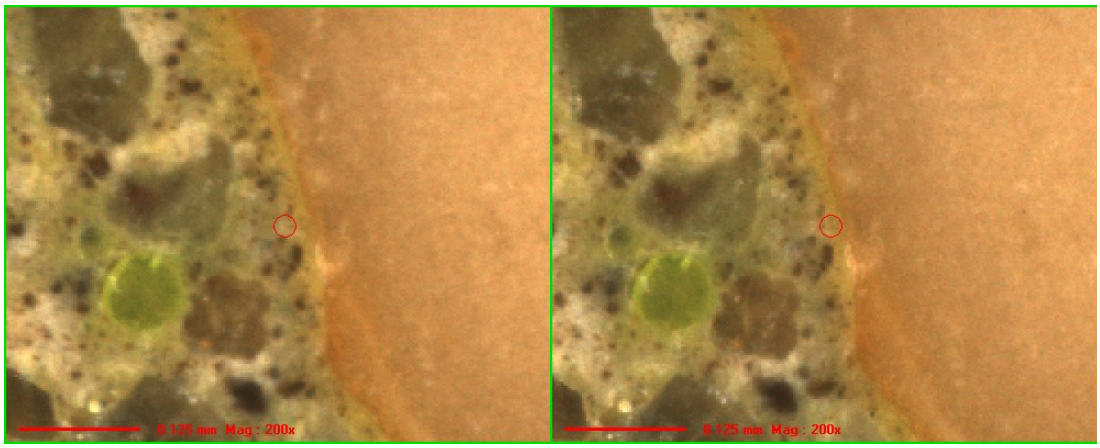


Figure 4-18: Spectra of different regions of concrete.

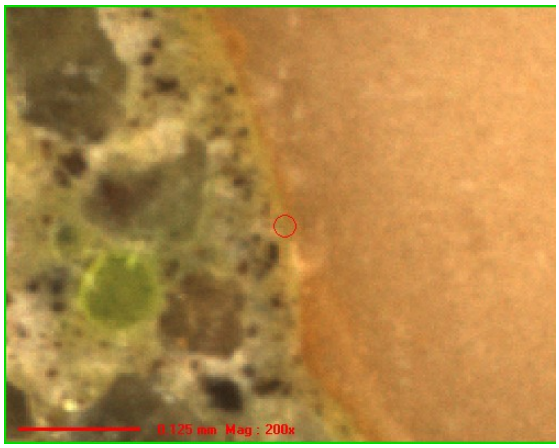
As seen in Figure 4-17, paste region has the highest dead time and total input count rate when compared to the interfaces and siliceous aggregate region. The dead time and total input count rate in the paste region is 30% and 7257 CPS respectively. Calcium is the abundant element in cement paste and the input count rate for calcium alone is 6332 CPS. As shown in Figure 4-18, calcium K peak is the highest in paste region when compared to the interfaces and siliceous aggregate. The characteristic X-ray energy for calcium is higher when compared to that of silicon, which is in the range of 3.688 – 4.013 keV. As explained previously, the comparatively more energetic characteristic X-rays for calcium able to escape the sample more easily leading to a high calcium input count rate and eventually high total input count rate. Total input count rate refers to the summation of the input count rate of all elements present. In cement paste region, other elements include aluminium, silicon, sulphur, potassium, and iron. These explain the reason for the dead time achieved while analysing paste region to be the highest. High total input count rate of the paste region caused detector to close down more often leading to a higher dead time.

Following the same principle and also shown in Figure 4-17, the dead time and total input count rate in siliceous aggregate is the lowest which is 16% and 2829 CPS respectively. Silicon is the abundant element in siliceous aggregates and the input count rate for silicon alone is 2804 CPS. Since the total input count rate is comparatively lower in siliceous aggregate, the detector switched off less frequently and therefore leading to a lower dead time. In Figure 4-18, silicon K peak is the highest in siliceous aggregate when compared to the interfaces and the paste region.

The dead time and total input count rate at the interfaces lie between that of pure paste region and siliceous aggregate. Interface 1 refers to a location where the beam spot is approximately 40 μm away from the cement paste-aggregate interface. As shown in Figure 4-17, the dead time and total input count rate at Interface 1 are 28% and 6556 CPS respectively. Calcium is still the abundant element with an input count rate of 5458 CPS however this value is slightly lower than that in pure paste region which is 6332 CPS. The input count rate for silicon at Interface 1 is 631 CPS which is slightly higher than that in cement paste region which is 415 CPS. These also can be seen in the form of spectrum as shown in Figure 4-18. These indicate the mixing of signals from these different regions of concrete started to occur and eventually affecting both the dead time and total input count rate. This condition is also observed at Interface 2 and 3. Interface 2 refers to a location where the edge of the circular beam spot is approximately touching the cement paste-aggregate interface. The dead time and total input count rate is 23% and 4623 CPS respectively. Interface 3 refers to a location where the beam spot is at the cement paste-aggregate interface. The dead time and total input count rate at this location is 19% and 3606 CPS respectively. Figure 4-19 shows the relative location of the three interfaces. The red circles in the figure are the beam spots. These results suggest that the spatial resolution of the μXRF technique is approximately of the order of the size of the X-ray beam size (30 μm).



(a) **(b)**



(c)

Figure 4-19: (a) Interface 1-beam spot approximately 40 µm away from the aggregate, (b) Interface 2-the edge of the beam is just touching the cement paste-aggregate interface, and (c) Interface 3-beam spot is right on the interface.

From the study thus far, it can be concluded that dead time and total input count rate at the interfaces vary between that of pure cement paste and aggregate region. If the atomic number of the abundant element in the aggregate is lower than calcium, the dead time achieved at interfaces will be higher than that achieved in the aggregate or equally lower than that achieved in the paste region.

4.4 Comparison between elemental mapping and dead time method

4.4.1 Procedure

The sample used for this study was C_{CEMI}-0.40-7d. The operating condition for spot analyses prior to mapping as well as for mapping was as shown in Table 4-1. As explained previously, a few spot analyses were necessary to identify the elements present in a sample. The area to be mapped was then defined following the simplest way as explained in the EDAX Orbis Vision User's Manual [2009]. The size of the area to be mapped was 2.32 mm × 1.79 mm. The matrix used was 128×100 pixels which means the spacing between two consecutive beam spots was approximately 18 μm in both X and Y directions. The dwell time was 1000 ms. With these settings, the mapping time was approximately 4 hour. The area selected for mapping is shown in Figure 4-20. After the mapping acquisition process completed, five spots were randomly selected in regions a, b, c, and d in Figure 4-20 for the dead time approach. The operating condition employed was also that as shown in Table 4-1.

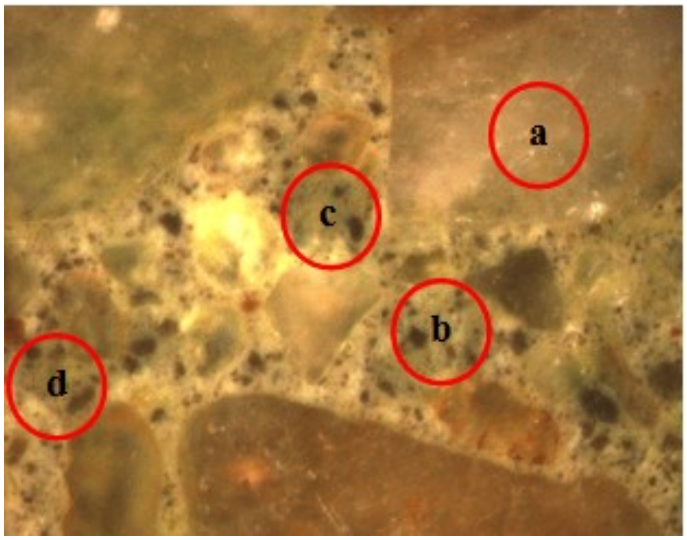


Figure 4-20: Regions selected for mapping on sample C_{CEMI}-0.40-7d (2.32mm×1.79mm).

4.4.2 Results

Figure 4-21 shows a composite elemental map obtained using the simple overlay approach which was explained previously under the methodology section. The area in cyan indicates the area where calcium presented in abundance while the blue particles represent the siliceous aggregates. Composite elemental map like this could be used to aid in locating the paste regions in mortars or concretes as part of the process of constructing chloride or sulphur profile.

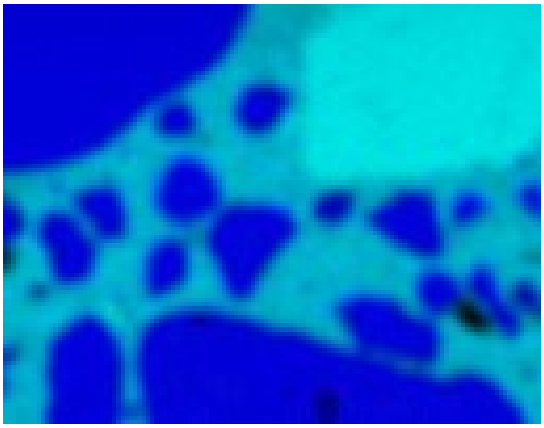


Figure 4-21: Different phases in sample C_{CEMI}-0.40-7d.

Figure 4-22 shows the composite elemental map as well as the four regions analysed using spot analysis. Based on the map, regions a-d are abundant in calcium and therefore these regions are the possible paste regions. Region "a" however was expected to be an aggregate since the cyan colour within this region was slightly brighter and hence differentiating the aggregate from the paste region.

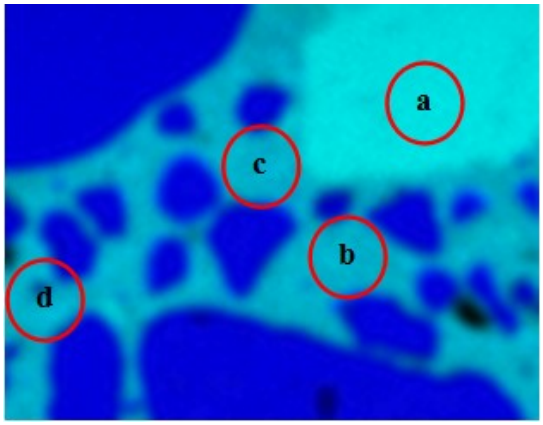


Figure 4-22: Comparison between elemental mapping and dead time approach.

Figure 4-23 presents a schematic which shows the different phases of concrete based on the dead time approach. As in the previous sections, dead time in this section refers to the midrange dead time. Also shown in the figure is the typical dead time achieved in pure cement paste. The pure paste sample used was P_{CEMI}-0.40-7d. Based on this schematic, any points in the green strip will be classified as ferrous aggregates. Points in the yellow and blue strip will be categorised as calcareous and siliceous aggregates, respectively while points in the orange strips are paste matrix. The grey regions have not yet been defined in this research.

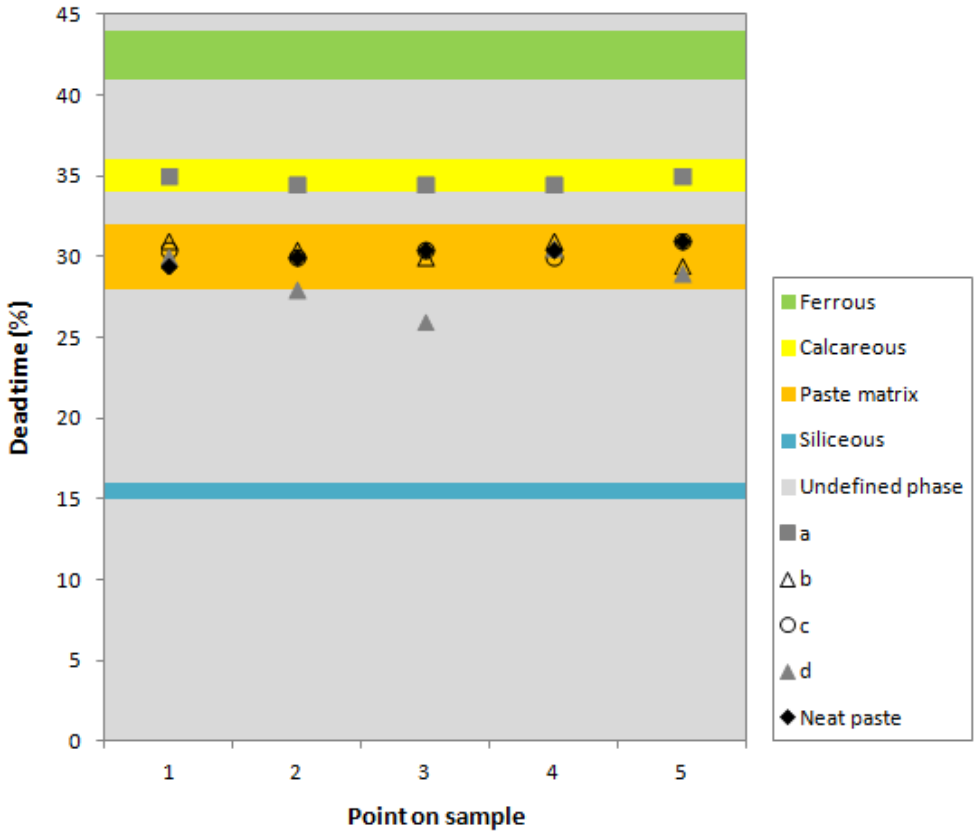


Figure 4-23: Schematic showing different phases of concrete based on dead time.

Based on Figure 4-23, all points in region "a" were located in an aggregate high in calcium. This is in agreement with the mapping approach (Figure 4-22). All points in region "b" and "c" can be categorised as paste matrix. This is also in agreement with the mapping approach. As expected with the mapping approach, points 1, 4, and 5 of region "d" were also categorised as paste matrix with the dead time approach.

Dead time achieved at point 2 and 3 of region "d" was in the range of 27-29% and 25-27% respectively. At these two locations, a slight reduction in calcium intensity and a slight gain in silicon intensity might occur due to mixing of signals from the different phases (aggregate and cement paste). This results in a lower total input intensity and hence lower dead time. Based on the dead time approach, point 2 and 3 in region "d" could not be classified as paste matrix. This is also in agreement with the mapping approach since region "d" (Figure 4-22) appears to contain a silicon-rich particle. This suggests point 2 and 3 of region "d" might be at the interface between siliceous aggregate and paste matrix.

From the study thus far, elemental map particularly calcium might aid the analyst to locate points in the paste regions of mortars or concretes for chloride or other elemental profiling. However this approach is subjective since one needs to rely on the colour to locate the paste regions in samples. Mapping approach is also tedious since analyst has to first acquire a set of elemental maps of the whole sample surface. After the post-processing for creating a composite map, the analyst then has to refer to the map and the real camera image in an alternating way for the paste region selection. It can also be tricky when dealing with calcareous aggregates for example since calcium presents in abundance in both the aggregates and the paste matrix. If the calcareous aggregates are coarse and hence obvious, analyst can still avoid from locating point in these regions. However if the calcareous aggregates are fine, then the paste regions selection could be erroneous.

4.5 Conclusions

Aggressive species particularly chloride and sulphate penetrate concrete through the porous cement paste matrix. Elemental mapping is one approach for locating cement paste regions in concrete for chloride and sulphur profiling. The effect of four operating parameters on the clarity of calcium and silicon elemental map was investigated. The parameters were beam spot size, beam voltage, amplifier time constant, and dwell time. The 30 μm beam size produced sharp calcium and silicon maps in comparison to the 1 or 2 mm beam size. This is due to the design of the 30 μm poly-capillary where it utilises a bundle of fibres of 3-5 μm diameter and thus producing high X-ray flux leading to sharp mapping images. Beam voltage and time

constant had insignificant effects on the clarity of calcium and silicon elemental maps. The longer the time spent for detecting characteristic X-ray photons at each location, the greater the SNR and hence clearer mapping images. Longer dwell time marginally improved the clarity of the elemental maps.

A new approach for identifying cement paste regions in concrete was presented. This is based on monitoring the change in dead time when a 30 μm beam samples cement paste or aggregate regions. Dead time is mainly affected by the input count rate, which is the characteristic X-ray photons from an analysed spot waiting to be detected by the detector. This study showed that the dead time achieved in siliceous, calcareous, and ferrous aggregates were in the range of 15-16%, 34-36%, and 41-44% respectively. The dead time achieved in pure paste samples was in the range of 28-32% regardless of the w/c and curing age. The dead time achieved at the interfaces varied between that of pure cement paste and aggregate regions. These results show that cement paste can be differentiated from aggregate particles on the basis of dead time. Therefore, identification of cement paste regions in concrete using the new approach for chloride and sulphate profiling is promising.

The main advantage of the dead time approach over elemental mapping is speed and ease of use. Elemental mapping is very time consuming since the whole sample surface has to be analysed before the generated set of maps could be used as guidance for locating cement paste regions. The elemental mapping approach is also subjective since the operator solely relies on the colour of the maps to locate paste regions. Therefore, it is prone to errors. For example, some of the points that appeared to be paste regions based on the calcium map were actually aggregate regions when these were cross-checked using the proposed dead-time approach.

Chapter 5 Calibration graphs for quantitative analysis of chlorine and sulphur

This Chapter presents the development of calibration graphs for quantitative analysis for chloride and sulphate in cement-based materials. This is done by analysing a range of cement paste samples containing known amounts of admixed chloride (or sulphate) and examining the strength of the correlation between measured X-ray intensities and actual amounts. The function of calibration graphs is to enable the conversion of measured X-ray intensities (in counts per second) into actual chloride or sulphur mass concentration. However, there are several sample parameters that might affect the measured X-ray intensities. These parameters include w/c ratio, binder type, curing age and moisture content. Therefore, the aim of this chapter is to establish whether a strong correlation exist between measured X-ray intensities and actual amounts of chloride (or sulphate) for a wide range of sample type and to understand the effects of w/c ratio, binder type, curing age and sample conditioning (drying prior to analysis) on the correlation. This will facilitate the development of μXRF for quantitative analysis of cement-based materials.

5.1 Introduction

Micro-XRF detects and measures characteristic X-rays emitted from a sample when it is irradiated by the primary X-ray beam. The characteristic X-rays are then processed and classified according to their energy levels. This determines the types of element present while the measured intensities indicate the amount of each element in the sample. The greater the measured characteristic X-ray intensity, the greater the amount present. For many applications, it is more meaningful to be able to determine and express the amount in terms of absolute mass or concentration. In concrete durability research for example, this ability enables one to ascertain whether the element of interest (e.g. chloride, sulphate) is within a recommended allowable limit or below a threshold value to ensure protection against degradation. This process of converting measured characteristic X-ray intensities to absolute mass or concentration values is known as quantitative analysis.

However, converting X-ray intensity to mass concentration is not a straightforward procedure, particularly for polychromatic excitation sources and multi-phase heterogeneous materials such as cement-based materials. This is due to the complex mathematical corrections required for matrix effects that include absorption and secondary fluorescence (enhancement) effects as explained in Chapter 2.4.3. There are several models available to do this, such as the influence coefficients and fundamental-parameters approach. However, it is well known these models cannot account for all variations in the instrument parameters and sample conditions. It is also necessary to calibrate these models with actual measurements made on samples with known compositions to improve their accuracy.

For some applications, quantitative analysis may be possible through the use of empirical calibration curves that plot measured net intensities (uncorrected for matrix effects) against known concentrations of standard samples. The calibration curve is then used on unknown samples to convert the intensity of the element of interest (such as chloride and sulphate) into mass concentration. This relies on the hypothesis that the measured net intensity is strongly correlated to actual mass concentration within the composition range of interest, which needs to be verified. Preparation of calibration samples is of critical importance for accurate evaluation of chloride or sulphate content in concrete. There are also other parameters that might affect the chloride and sulphur signals in cement-based materials. For example, Proverbio & Carassiti [1997] studied the influence of morphology and composition of chloride containing phases on microXRF analytical results. They observed that for the same chloride concentration, chloride fluorescence intensity decreased when the chloride was present in the concrete matrix as sodium chloride salt instead of being dissolved in pore solution.

The aim of chapter is to develop calibration curves for quantitative analysis of chloride and sulphate content in cement-based materials. These calibration curves will be produced by measuring samples containing known amounts of admixed chloride or sulphate, and exploring the correlations between measured fluorescence intensities and actual concentrations. This Chapter also aims to understand the effects of w/c ratio, binder type, curing age and sample conditioning (drying prior to μXRF analysis) on the correlations and resulting calibration curves for chloride and sulphate. Another

objective is to establish if a “master” calibration curve exists for a range of mix composition, which would greatly facilitate quantitative analysis.

5.2 Methodology

5.2.1 Samples containing admixed chloride

Three series of cement paste calibration samples with known admixed chloride content were prepared. In series I, cement pastes of water-to-cement (w/c) mass ratios of 0.3, 0.4, and 0.5 were prepared. For each w/c ratio, seven samples each with different admixed chloride content were prepared. The chloride contents were 0.00, 0.10, 0.15, 0.20, 0.50, 2.00, and 3.00% by mass of cement. This range of chloride content was designed based on the range of typical chloride threshold values as reviewed by Angst et al. [2009]. The cement type was CEM I that contained no chloride. The purpose of this series was to examine the effect of w/c ratio on the correlation between measured chloride X-ray intensity and actual chloride content.

Samples in series II were prepared with either CEM I cement with 60% wt. replacement of ground-granulated blast furnace slag (GGBS) or CEM I cement with 30% wt. replacement of pulverised fuel ash (PFA). The water-to-binder (w/b) ratio was fixed at 0.4. For every binder type, seven paste samples 0.00, 0.10, 0.15, 0.20, 0.50, 2.00, and 3.00% admixed chloride by mass of binder were prepared. The purpose of this series was to examine the effect of binder type on the correlation between measured chloride X-ray intensity and actual chloride content.

For each mix proportion, ingredients were batched by mass and mixed in a bowl mixer for three minutes. Tap water was used as batch water. Mixes containing chloride were prepared by first dissolving the required amount of sodium chloride (NaCl) in batch water. Samples were cast by compacting in two equal layers in plastic cylindrical moulds (50 mm diameter, 60 mm height) using a vibrating table. For each layer, the compaction was considered sufficient when no significant air bubbles escaped the surface. The mould was then capped and sealed with waterproof tape to avoid leakage. Subsequently, the mould was fixed to a rotating machine with adjustable speed and rotated slowly for 24 hour to avoid bleeding and segregation effects. These steps were repeated for all the mix each with different chloride content.

After the first 24 hours, samples were de-moulded, labelled, and placed in fog room at 100% RH for curing until the age of 28 day. After the curing period, each sample was dry saw-cut into halves or three equal slices along the transverse axis. The sample was then freeze dried (Section 3.2.2) until constant mass is reached, which took approximately 24 to 30 days.

Samples in series III were prepared with CEM I cement at w/c ratio of 0.4 and chloride contents of 0.00, 0.15, 0.50, 2.00, and 3.00% by mass of cement. These were prepared following the same manner for series I and II, except that two replicate cylindrical samples were cast for each admixed chloride content. After the initial 24 hour following mixing, the samples still in their plastic containers were wrapped in cling film and sealed cured in polythene bags at 20^0C until the age of 3 days. At the end of the curing period, the samples were de-moulded and saw-cut into halves along the transverse axis. For each set, one half was freeze dried, one half was oven dried at 50^0C, one half was analysed as-is without any drying, and the last remaining half was unused. Freeze-drying and oven-drying took about 24 days to reach constant mass. The purpose of this series was to study the effect of sample conditioning (drying) on the correlation between measured chloride X-ray intensity and actual chloride content.

5.2.2 Samples containing admixed sulphate

Cement paste samples containing known amounts of admixed sulphate were prepared using CEM I cement at w/c ratio of 0.4. The sulphate (SO_4) contents were 0.0, 0.5, 1.0, 1.5, 2.0, 3.0, and 5.0% by mass of cement. This range was designed based on the recommended maximum limit on total SO_3 content in concrete which is typically in the range of 3.5 – 4.0% by mass of cement [The Concrete Society, 2014]. To convert SO_3 to SO_4, the value for SO_3 was multiplied by 1.2.

Samples were prepared following the same mixing and casting procedures described in the previous section. Mixes containing sulphate were prepared by first dissolving the required amount of sodium sulphate (Na_2SO_4) in the batch water (tap water).

Two replicate samples were prepared for each mix. The first replicate was cured in the plastic container wrapped in cling film and sealed in polythene bags at 20^0C until the age of 3 days. The second replicate was de-moulded after the first 24-hour following

mixing, labelled, and then cured in fog room at 100% RH for curing until the age of 28 day. At the end of curing, samples were saw-cut into three equal sections along the transverse axis. One section from each cylindrical sample was then freeze dried until constant mass is reached, which took approximately 22 days.

5.2.3 Preparation for μXRF analysis

At the completion of curing and conditioning, the saw-cut surface of each sample was dry ground to achieve a flat surface for μXRF analyses. The grinding process was carried out using a Struers LaboPol-5 machine with adjustable speed with Struers silicon carbide paper of grit size of 80 and then grit size 120. Samples from series III (containing admixed chloride) were ground further at grit size 500 and finally 1200. For each grit size, the samples were ground at 100 – 150 rpm for 2 minutes and cleaned using compressed air before moving to the next finer grit size. Samples were then analysed immediately or kept in sealed bags which were then placed in dessicators to avoid carbonation.

The μXRF data acquisition and analysis were carried out based on the optimised procedures described in Chapter 3. The background spectrum was subtracted based on the background subtraction method proposed by Ernst et al. [2012] which is explained in Chapter 3.2.5. The net X-ray counts obtained after the manual background subtraction were converted into counts per second (CPS) by dividing with the acquisition time used.

5.3 Results

In this section, the measured characteristic X-ray intensities (in counts per second) for chloride and sulphate are plotted against the known values in the form of a series of "calibration" graphs. For the chloride calibration graphs, each point is an average of twenty separate measurements spread over the entire sample surface. For the sulphate calibration graphs, each point is an average of ten separate measurements spread over the entire sample surface. The lower level of replication used in sulphate analysis was deemed adequate because the measured signal (counts per second) was stronger than that of chloride. The error bars represent the standard error for the mean value (equals to standard deviation of the average divided by square-root of number of determination).

5.3.1 General observations

All results are presented in Figures 5.1 to 5.5. It is very clear that the measured characteristic X-ray intensities for chloride and sulphate show a strong linear correlation with their actual known amounts in the cement paste samples. The coefficient of linear regression (R^2) is at least 0.9 and is greater than 0.99 in many cases. Therefore, this gives a good confidence that the measured characteristic X–ray intensities from μXRF can be used for quantitative analysis of unknown samples. Parameters such as w/c ratio, curing age, binder type and conditioning regime can have a small, but detectable influence on the characteristic of the correlation. These are discussed in subsequent sections.

5.3.2 Effect of w/c ratio

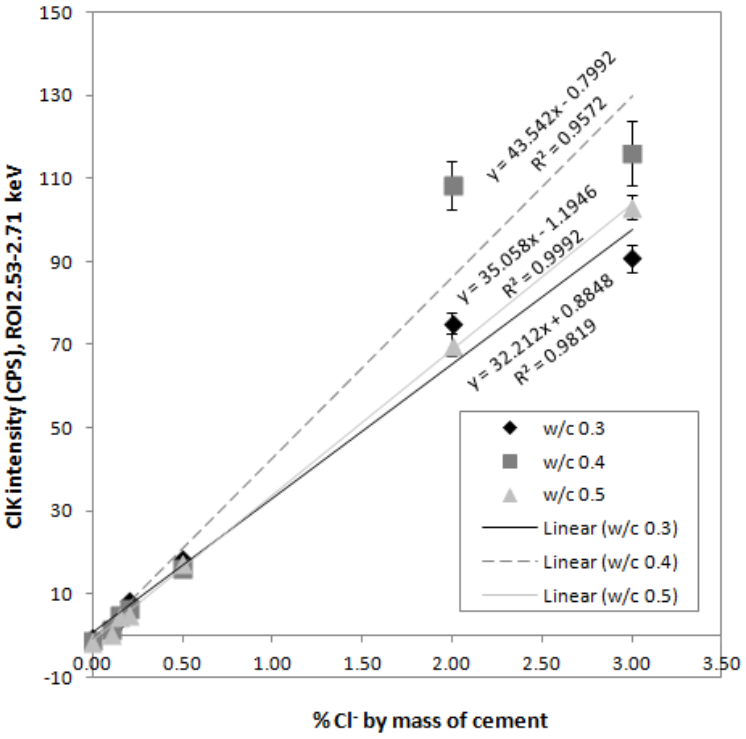
Figure 5-1a shows the correlation between measured characteristic X-ray intensity (counts per second) and actual chloride content (expressed as percentage by mass of cement) for 28-day CEM I cement pastes at different w/c ratios (0.3, 0.4, and 0.5). The samples are from series I (Chapter 5.2.1). Beam voltage and beam current used was 30 kV and 170 μA respectively. Time constant was 12.8 μs and the 25 μm aluminium filter was applied to remove rhodium Rayleigh scatter from obscuring the chloride peak. The beam size and acquisition time were 30 μm and 200 s live time respectively. The analyses were carried out under vacuum. With this set of operating parameters,

the dead time ~ 40%. Actual dead time achieved at each spot was in the range of 38-42%.

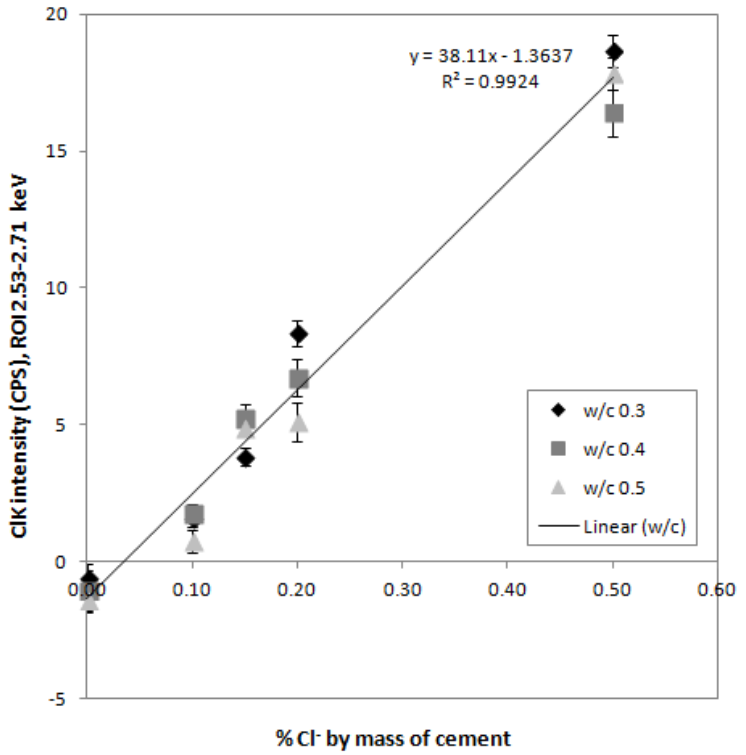
The results show that at 0% chloride content, the measured X-ray intensity at all w/c ratios has a very slight negative value (~ -1 cps). This is most likely due to errors in measurements at trace levels and/or errors arising from imperfect background correction when the instrument is operating at its detection limit. Nevertheless, this is small and considered insignificant. As the chloride content increased, the measured X-ray intensity increased following a strong linear correlation.

However, the results in Figure 5-1a suggest that w/c ratio may have a slight effect on the correlation, particularly for samples containing high chloride content (> 0.5 % by mass of cement). The regression line for w/c 0.3 produced the smallest slope and this could be due to the increase in sample density as water/cement ratio decreases [Hover, 2006]. It is well-known that X-ray attenuation is greater in denser materials [Hands & Armitt, 1998; McKetty, 1998]. Therefore, incoming X-rays from the X-ray tube as well as the emitted characteristic X-rays including that of chloride would be attenuated to a greater degree in samples with w/c ratio 0.3 leading to lower measured intensities.

If the reasoning above is true, then it would also be expected that the regression line for w/c ratio 0.5 to have the greatest slope. However this is not the case. Instead, the slope for the calibration graph for w/c ratio 0.5 was in between that of w/c ratio 0.3 and 0.4. Unfortunately, this discrepancy cannot be explained at the moment. The μXRF analysis was repeated, but the same results were obtained. It is possible that an experimental error has occurred during sample preparation for w/c 0.4 where higher amount of chloride was added to the mix that should contain 2% and 3% chloride by mass of cement. However, if we ignore samples with higher amounts of chloride and only consider those that contain ≤ 0.5% chloride by mass of cement, then we find that all data from different w/c ratios can be represented by a single regression line. This is shown in Fig. 5.1b. This suggests that the effect w/c ratio on the calibration graph is small.



a) Full results



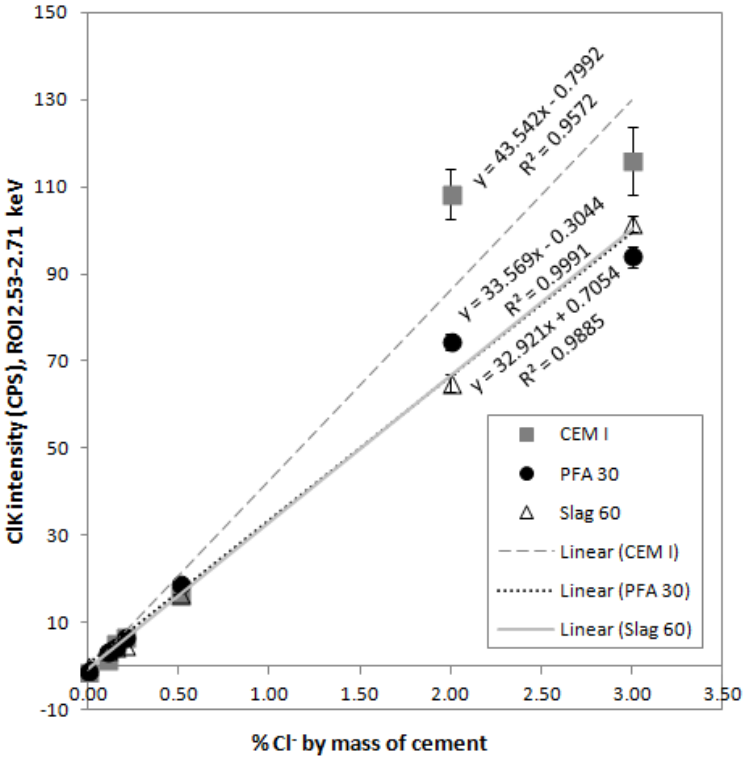
b) Partial results (Cl ≤ 0.5% by mass of cement)

Figure 5-1: Correlation between measured characteristic X-ray intensity and actual chloride content for 28-day CEM I cement pastes at various w/c ratios.

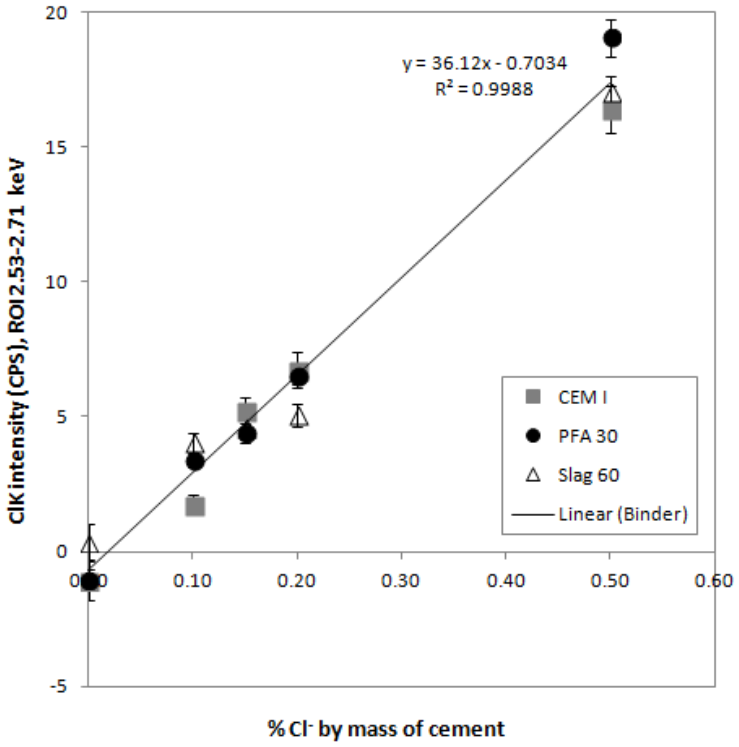
5.3.3 Effect of binder type

Figure 5-2 shows the effect of binder type on the correlation between measured characteristic X-ray intensity (counts per second) and actual chloride content (expressed as percentage by mass of cement) for 28-day CEM I cement pastes at 0.4 w/c ratio. The samples are from series II (Chapter 5.2.1). Operating parameters for the μXRF are the same as that used in section 5.3.2 for establishing the effect of w/c ratio.

As seen in Figure 5-2, the linear regression for samples containing PFA is almost identical to that for samples containing slag. However, the correlation for samples containing CEM I only is significantly different and has greater slope compared to those of samples containing SCMs. Again, the y-intercepts at 0% chloride showed slight non-zero values and this is probably due to errors in measurements and background corrections as discussed earlier. If we only consider samples that contain ≤ 0.5% chloride by mass of cement, then we observe that the data from different binder types can be represented by a single regression line. This is shown in Fig. 5.2b.



a) Full results



b) Partial results (Cl ≤ 0.5% mass of cement)

Figure 5-2: Effect of cement type on the correlation between measured characteristic X-ray intensity and actual chloride content for 28-day cement pastes

Figure 5-3 shows the correlation between measured characteristic X-ray intensity and actual chloride content for all samples from mixes of different w/c ratios and binder types. It is very clear that two data points from w/c 0.4 are outliers (circled). This lends support to the suggestion earlier (Chapter 5.3.2) that an experimental error has occurred during the preparation of these samples. If the two outliers are data points are excluded, then the remaining data set can be represented by a single linear equation with a coefficient of regression greater than 0.99, as shown in Figure 5-3.

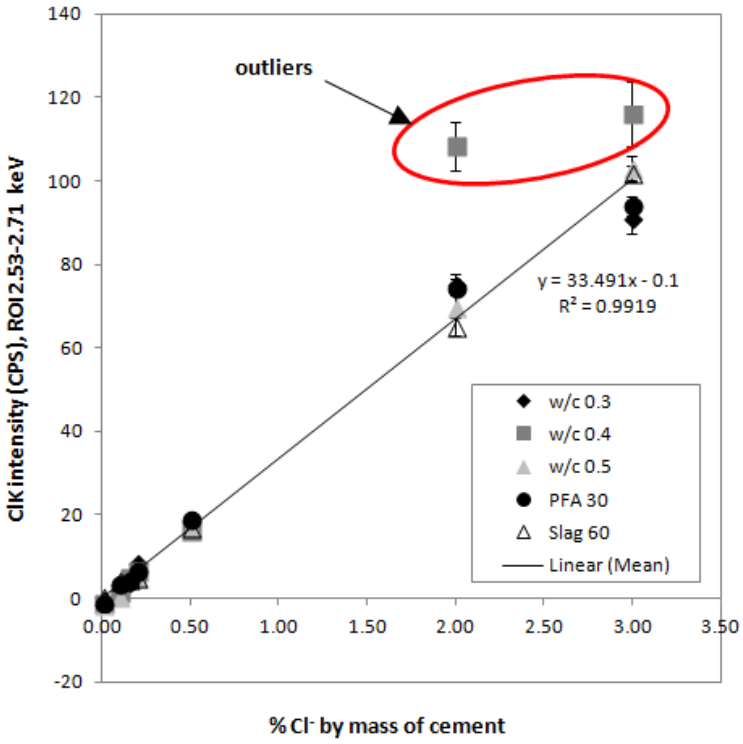


Figure 5-3: Correlation between measured characteristic X-ray intensity and actual chloride content for 28-day cement pastes with different w/c ratio and binder types.

5.3.4 Effect of curing age

Figure 5-4 shows the correlation between measured characteristic X-ray intensity (counts per second) and actual sulphate content (expressed as percentage by mass of cement) for 3 and 28-day CEM I cement pastes at 0.4 w/c ratio. The samples are those explained in Chapter 5.2.2. The beam voltage and beam current used was 25 kV and 90 µA respectively. The acquisition time, time constant, and beam spot size was 250 s live, 12.8 µs, and 30 µm respectively. The analyses were carried out in vacuum environment and without the application of filter. With this set of operating condition, the dead time was ~ 40%. Dead time achieved at each spot was in the range of 38-42%.

Similar to the chloride calibration curve, the results show a strong linear correlation for the case of sulphate. However, curing age of the samples at the time of measurement has a clear influence on the regression line. As seen in the figure, 3-day

cured samples produced higher sulphur signals in comparison to 28-day samples. This is due to the effect of curing and further hydration on the densification of the sample. The samples cured for 28 day are denser than samples cured for 3 day. As discussed in Chapter 5.3.2, the attenuation of X-rays is greater in denser material. X-rays that penetrated the sample from the X-ray tube as well as the emerged characteristic X-ray photons including that of sulphur were attenuated to a greater degree in samples cured for 28 day leading to lower sulphur intensity. Another possible explanation is related to the differences in bound water content of the samples at 3 and 28 days. The bound water content in samples cured for 28 days is higher than that in samples cured for 3 days. Therefore, both the incoming X-rays from the X-ray tube and the emerging characteristic X-ray photons which include characteristic X-rays for sulphur were attenuated to a higher degree in the 28-day samples leading to lower sulphur intensity. The intensities for aluminium, silicon, and calcium of the 28-day samples are also lower in comparison to those of the 3-day samples.

It is likely that the effect of curing age will continue up to a point beyond which, the change in density is too small to cause further X-ray attenuation. Therefore, calibration graphs produced from well-hydrated systems would be more accurate and better suited for analysing well-cured field samples.

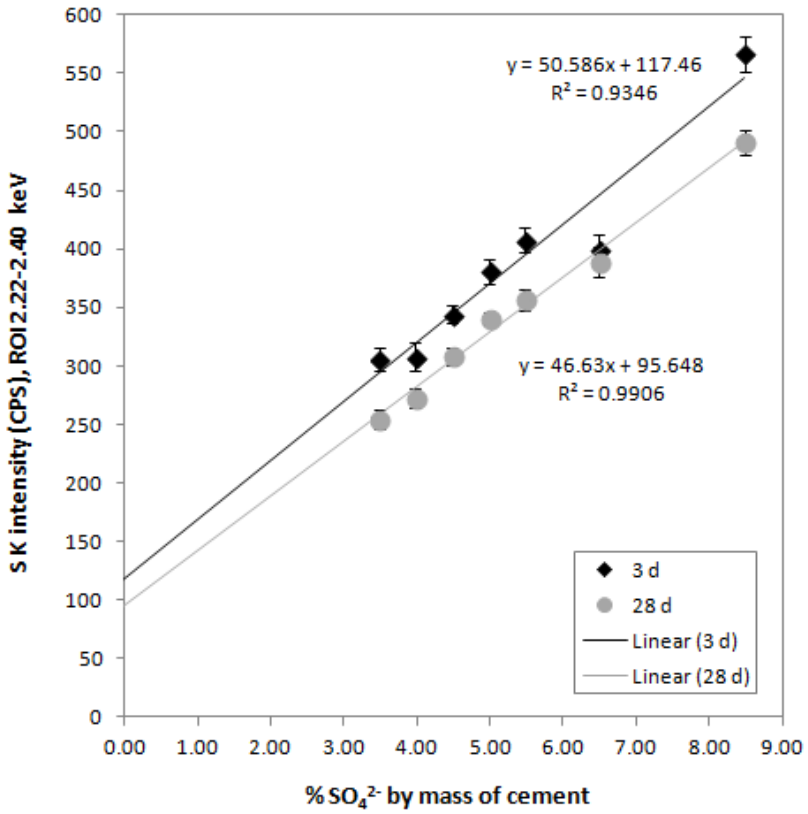


Figure 5-4: Correlation between measured characteristic X-ray intensity and actual sulphate content for 3-day and 28-day cement pastes

5.3.5 Effect of sample conditioning

Figure 5-5 shows the effect of sample conditioning, i.e. drying regime prior to μXRF analysis, on the correlation between measured chloride X-ray intensity and actual chloride content. The samples were from Series III (Chapter 5.2.1) and they were analysed either as-is (wet condition), after freeze drying or oven-drying at 50°C. The applied beam voltage was 15 kV and beam current was adjusted to 520 μA to reach a dead time of ~ 30%. The acquisition time and time constant were 100 s live time and 12.8 μs respectively. A 25 μm aluminium filter was applied and beam spot size was 30 μm throughout. However, the analyses were carried out in air chamber (ambient condition) rather than in vacuum to prevent the wet samples from out-gassing and drying during measurements.

Results in Figure 5-5 show that the strong linear correlation between measured chloride X-ray intensity and actual content is maintained even when samples were

analysed in a wet state (as-is) and in ambient environment (air-chamber). This highlights a technical advantage of μXRF for its ability to analyse wet samples that may be sensitive to drying-induced changes or damage.

However, the drying condition or rather the moisture state of the sample has a huge effect on the measured X-ray intensity. As seen in Figure 5-5, the X-ray intensities from samples analysed as-is are substantially lower for all chloride contents compared to those from samples that were freeze dried or 50°C oven dried. This is due to presence of moisture in the sample that absorbs the chloride characteristic X-ray photons leading to a lower emitted intensity. This equally means an increase in the number of X-ray counts with time at a location in a specimen may indicate a decrease in moisture content [Wojcik, 2004]. The 50°C oven dried samples had the lowest moisture content and therefore produced the highest X-ray intensities.

The effect of conditioning regime can be further elucidated by examining the dead time achieved while analysing each sample. The results are shown in Table 5-1. The midrange is the mean of the maximum and minimum values of each data set, calculated using Equation 4-2 as shown in Chapter 4. As seen in Table 5-1, higher dead time was achieved when sample was in dried condition. For example, the midrange dead time for as-is, freeze dried, and 50^0 C oven dried sample at 3% chloride content was 30%, 31%, and 32% respectively. The midrange dead time for as-is sample at 2% chloride content was 30% while the midrange dead time for freeze dried and 50^0C oven dried sample were both 32%. The same pattern was observed in samples with 0.50 and 0.15% chloride content.

As explained in Chapter 4, dead time increases when more X-rays try to enter the detector leading to frequent detector close down. In moist sample, both the incoming X-rays from the X-ray tube and the emerging characteristic X-ray photons which include the characteristic X-rays for chloride are attenuated by both the sample and water molecules to a certain degree. This leads to a lower incoming intensity and therefore dead time. In dry samples, less X-rays are absorbed due to the absence of moisture. This resulted in more X-rays trying to enter the detector and therefore leading to higher dead time.

It can also be observed that the measured chloride intensities for the freeze-dried samples are significantly lower (about 50% lower) than those obtained from similar samples but tested in vacuum (see Figure 5.3). This is because the presence of gas molecules in the analysis chamber that attenuates the emitted X-ray photons as explained in Chapter 3.3.2

The results show that sample moisture content has a huge effect on the emitted fluorescence X-ray intensities. Therefore, samples must be pre-conditioned to a standard moisture state to ensure repeatable results and allow meaningful comparison across different samples.

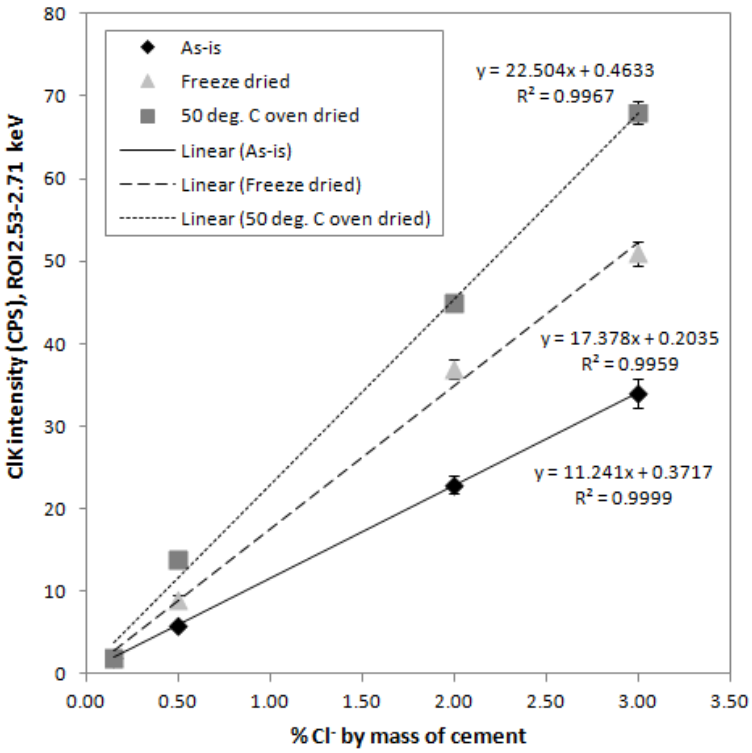


Figure 5-5: Effect of sample conditioning (drying) on the correlation between measured characteristic X-ray intensity and actual chloride content. Samples are CEM I pastes at 0.4 w/c ratio.

Table 5-1: Effect of drying condition on dead time achieved for samples from Series III.

Sample condition	% Cl^- by mass of cement					
	3.00%			2.00%		
	Actual Dtm (%)	Midrange Dtm (%)	Mean CPS	Actual Dtm (%)	Midrange Dtm (%)	Mean CPS
As-is	28-31	30	34	29-31	30	23
Freeze dried	29-33	31	51	30-33	32	37
50^0C oven dried	30-33	32	68	30-34	32	45

5.4 Conclusions

The results from this chapter show that a strong linear correlation ($R^2 > 0.9$) is observed between characteristic X-ray intensities for chloride (or sulphate) and the actual known amounts in cement paste samples with a different w/c ratio, binder type, curing age and drying condition. This is observed even when samples were analysed in a wet state (as-is) in ambient environment (air-chamber). The measured X-ray signals are sensitive to changes in small quantities (close to threshold values) within typical allowable limits. These findings provide evidence that the measured characteristic X–ray intensities from μXRF and the observed correlations can be used as calibration for quantitative analysis of unknown samples. Furthermore, μXRF can be used for quantitative analysis of wet samples that may be sensitive to drying-induced changes or damage.

Drying condition and sample moisture state has a major effect on the measured X-ray intensities. Wet samples produce lower X-ray intensities compared to dried samples. This is due to the attenuation of X-rays by the presence of water in moist samples. Therefore, it is very important that samples are pre-conditioned to a standard moisture state to ensure repeatable results and to allow meaningful comparison across different samples. Similarly, sample curing age at the time of measurement has a slight influence on the correlation. Well hydrated and therefore denser materials attenuated more X-rays, thus leading to lower chloride or sulphur signals, producing calibration

graphs with smaller slopes. The effect of curing age is likely to continue up to a point beyond which, the change in density is too small to cause further X-ray attenuation. Therefore, calibration graphs produced from well-hydrated systems would be more accurate and better suited for analysing field samples.

For 28-day cured samples, parameters such as w/c ratio and binder type seem to have only a small effect on the correlation. The data from a range of sample types can be represented by a single regression line with a coefficient of regression greater than 0.99, as shown in Figure 5-3. Based on these results, it is evident that the choice of calibration samples is important for accurate determination of chloride or sulphate content in cement-based materials.

Chapter 6 Transport of chloride and sulphate in cement based materials

This Chapter investigates the effect of sample drying, surface preparation (grinding), binder type and water/binder ratio on chloride profiles of mortar samples exposed to wick action. The aim of the work was to determine the most appropriate preparation method for studying non-saturated transport processes and to ascertain whether μXRF has sufficient sensitivity to measure the effects of binder type and water/binder ratio on transport properties. This Chapter also demonstrates the application of the proposed approach for identifying cement paste regions in mortars and concretes using dead time as presented in Chapter 4 and the calibration graphs constructed in Chapter 5 for quantitative analysis of chloride and sulphate. Chloride concentrations measured using this approach were slightly higher than those measured by wet chemistry analysis (titration). However, the characteristics of the chloride profiles and penetration depths measured by both methods were identical.

6.1 Introduction

Chapter 3 showed that the SNR and LOD of chloride and sulphate improves when samples are analysed in vacuum. However, samples have to be dried for analysis in vacuum. A wet sample will outgas in a vacuum environment and this will affect results or may cause damage to the equipment. However, drying the sample prior to analysis may distort the measured chloride (or sulphate) profile in the samples. For example, the removal of water may pull chlorides or sulphates from the internal concrete via capillary effects towards the external surface subjected to drying. Another possible effect is that the loss of water in the surface region causes an increase in ionic concentration and therefore further diffusion occurs into the sample.

It seems that no studies have been carried out to examine this. The main research questions that need to be answered are: a) what are the effects of drying on concentration profiles, and b) what is the optimum method to dry samples prior to μXRF analysis that will best preserve chloride/sulphate profiles?

Another issue is with surface preparation. Previous research prepared the sample surface for μXRF analysis in different ways. Sutter et al. [2009] epoxy impregnated and ground their samples until uniformly flat surfaces were obtained. Davis et al. [2011] analysed their sample in an unpolished state. Snyder et al. [2012] did mention that some consideration of the sample surface roughness is required to produce high quality images and spectra. However there was no explanation on what is the optimal sample surface preparation. Based on these, another question was raised on whether grinding of the sample surface affects the original chloride profiles.

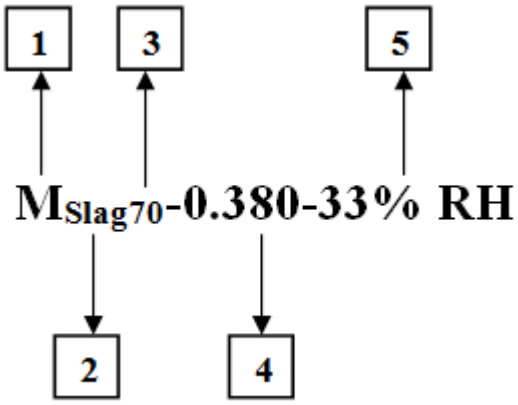
One of the aims of this Chapter is therefore to answer these questions. In addition, this chapter also aims to study the influence of binder type and water/binder ratio on the chloride profiles of samples exposed to a wick action environment. Lastly, this Chapter will demonstrate the application of the dead time approach developed in Chapter 4 and the calibration graphs developed in Chapter 5 for the quantitative analysis of chloride and sulphate in concrete.

6.2 Parametric study

There are several parameters that might affect the chloride profiles in cement based materials. In this work, the parameters under study were binder type, water/binder (w/b) ratio, drying method, and surface grinding. Because chloride diffusion in cementitious materials is essentially a very slow process and accelerating this process tends to distort the transport process, it usually requires several years to prepare and expose samples in order to gain an appreciable diffusion profile. As such, the results presented in this section were obtained from samples that have been prepared from another project (Nanocem supported) that was carried out by Nilla Olsson, a PhD student from Lund University, Sweden. The aim of Nilla's PhD was to better understand non-saturated chloride diffusion. The work presented in section also received help from François Marin-Cudraz [2015], an MSc student at Imperial College London. All of the data collection and analyses were carried out by myself with assistance from François Marin-Cudraz.

6.2.1 Methodology

The sample naming convention in this Chapter differs from the one in the previous Chapters due to the different nature of the samples analysed. The sample naming convention is shown in Figure 6-1.



where:

Number	Definition	Detail
1	Sample type	M is for mortar
2	Binder type	-
3	Percent of cement replacement	-
4	Water/binder ratio	-
5	Drying environment	Relative humidity

Figure 6-1: The sample naming convention.

Sample preparation

All of the samples investigated in this section were mortars. Four different binders were used. The binders were ordinary Portland cement (OPC) CEM I 42.5 N, OPC with 5% silica fume (SF), OPC with 40% ground granulated blast furnace slag (slag), and OPC with 70% slag. The percentage replacement of OPC with either SF or slag is by mass. The main oxide compositions of the OPC and the slag are shown in Table 6-1.

Table 6-1: Oxide composition of the OPC and slag.

Main oxide	OPC (% wt.)	Slag (% wt.)
SiO_2	19.88	36.11
Al_2O_3	4.47	9.87
Fe_2O_3	2.96	0.43
CaO	63.49	42.25
MgO	1.77	7.26
SO_3	2.96	3.30

Siliceous (quartz) sand in accordance with EN 196-1 was used as the aggregates. The binder-to-sand ratio was 1:3 on equivalent volume basis. The water/binder ratios were 0.38 and 0.53 on equivalent volume basis. This gives a slight variation in w/b ratio for binders with slag and silica fume.

Mortar blocks of 60cm×25cm×25cm were cast and de-moulded after the first 24 hour. After de-moulding, these blocks were placed into containers with a limited amount of tap water for wet curing. The curing water was limited to approximately 1 cm around the edges of the blocks to limit the volume of water and thus minimising leaching. After one week of curing, cores with a diameter of 94 mm were drilled from the blocks. The cores were then immediately placed into their holes in the blocks for further wet curing. After two months, the cores were wet saw cut into discs with a thickness of 36 mm. The sets of discs were placed back in their holes for further wet curing until the age of 3 years. Figure 6-2 shows the wet curing of the samples. As seen in the figure, the blocks were placed in large containers in a way that the blocks were completely submerged in the curing water. To maintain a constant water level, containers were covered with plastic films and regularly refilled with water.



Figure 6-2: Wet curing of the mortar samples [Personal communication with Nilla Olsson].

Sample exposure to wick action

At the end of the curing period, the mortar discs were exposed to chloride penetration via wick action. The samples were in saturated condition at the beginning of the exposure to wick action. One flat end of each of the mortar cylindrical samples was exposed to 6.0 weight percentage sodium chloride (NaCl) solution while the other flat end was exposed to drying conditions of either 33% or 75% relative humidity (RH). The side exposed to NaCl was referred to as the wet side while the side exposed to the different RHs was referred to as the drying side. The samples were exposed to wick action experiment from February 2013 until spring 2015. Figure 6-3 shows the wick action test setup. The bottom sides of the samples were the drying side while the top sides were the wet sides.



Figure 6-3: The wick action test setup [Personal communication with Nilla Olsson].

At the end of the exposure to the wick action environment for approximately 2 years, the samples were split longitudinally into two halves and sent to Concrete Durability lab at Imperial College London. The samples were kept in the lab at 20^0C while waiting to be analysed in order to preserve the profiles of the chemical elements.

For the study on the effect of drying on chloride profiles, the sample (mortar cylinder, 20 mm diameter, 25 mm length) was analysed either as is, freeze-dried or oven-dried at 50°C. Based on the naming convention, the sample was M_{SF5}-0.380-50% RH. This sample was one of the samples in the preliminary batch prior to the actual batches which the sample casting and sample exposure to wick action are explained in the previous paragraphs. The w/b and binder to sand ratio was 0.38 and 1:3 respectively. The binder was OPC with 5% silica fume. The sample was also exposed to wick-action experiment. The wet side was treated with 6 weight% NaCl solution for approximately 6 month while the dry side was exposed to 50% RH at 20^0C. The sample was split longitudinally into two halves prior to submission to Imperial College London. The sample was sealed with blue waterproofing tape, which appears to have fused on the sample upon arrival.

Data acquisition

Without further treatment, one half of all samples were analysed as-is for the chloride profiles using μXRF. Sample was first positioned on the Plexiglas stage in a way that the side exposed to NaCl solution was on the left while the side exposed to the drying condition was on the right. Sample was secured to the stage using Blu-Tack. It is important to ensure sample is properly fixed to the stage to avoid sample disturbance when the stage moves, which then might alter the pre-selected analysis points. Loosely attached sample might also fall off the stage during analysis period and thus putting the equipment at risk. The Z axis was then adjusted so that the sample appears in sharp focus under both low magnification camera (10×) and high magnification camera (70×). A total of 170 points were selected on the sample surface with distance between points of 2 mm measured from centre of beam. Figure 6-4 shows two of the selected points for analysis. Some region appears sharp and some region appears blurry, due to the uneven surface of the as received sample.

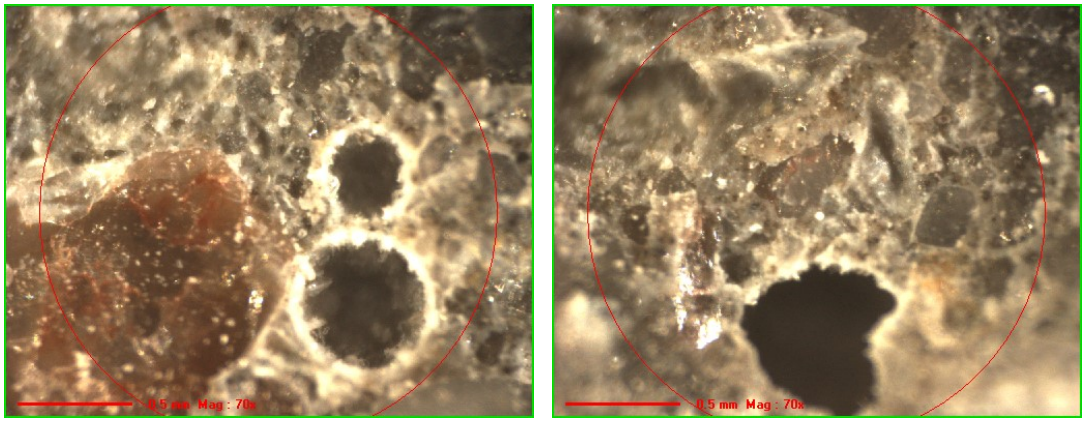


Figure 6-4: Examples of the selected points for analysis.

On the sample surface, ten points were measured on each X coordinate at different Y coordinates. This is shown in Figure 6-5. The bold lines represent the flat sides of the sample. Please note that the image is not to scale. The details on the locations of the points are shown in Table 6-2. The letter P in the table is an abbreviation of the word ‘point’.

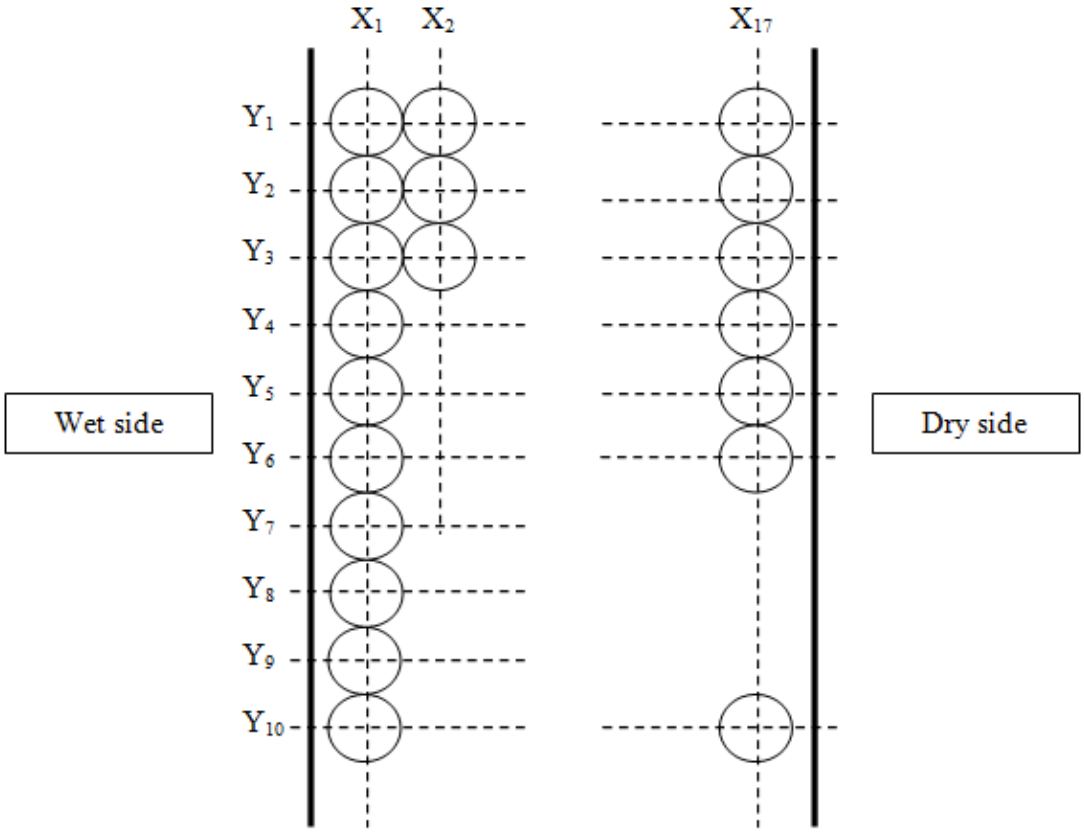


Figure 6-5: Sample and point orientation.

Table 6-2: Details on the location of the points.

	X_1	X_2	X_{17}
Y_1	P1	P11	P161
Y_2	P2	P12	P162
Y_3	P3	P13	P163
Y_4	P4	…	P164
Y_5	P5	…	P165
Y_6	P6	…	P166
Y_7	P7	…	…
Y_8	P8	…	…
Y_9	P9	…	…
Y_{10}	P10	…	P170

The chloride profiles were constructed by first averaging the intensity of chloride characteristic X-rays in counts per second (CPS) values from P1 to P10 on X_1 coordinate. This process was repeated for X_2 to X_{17}. There were therefore 17 mean CPS values from X_1 to X_{17}. These values were then plotted against depth (mm). For each sample, the analysed area was approximately 680 mm^2.

For the sample from the preliminary batch (M_{SF5}-0.380-50% RH), a total of 78 points were selected on the sample surface with distance between points of 2 mm measured from centre of beam. Figure 6-6 shows two of the selected points for analysis. Instead of ten, only six points each at different Y coordinates were measured on each X coordinate. The details on the location of the points are shown in Table 6-3.

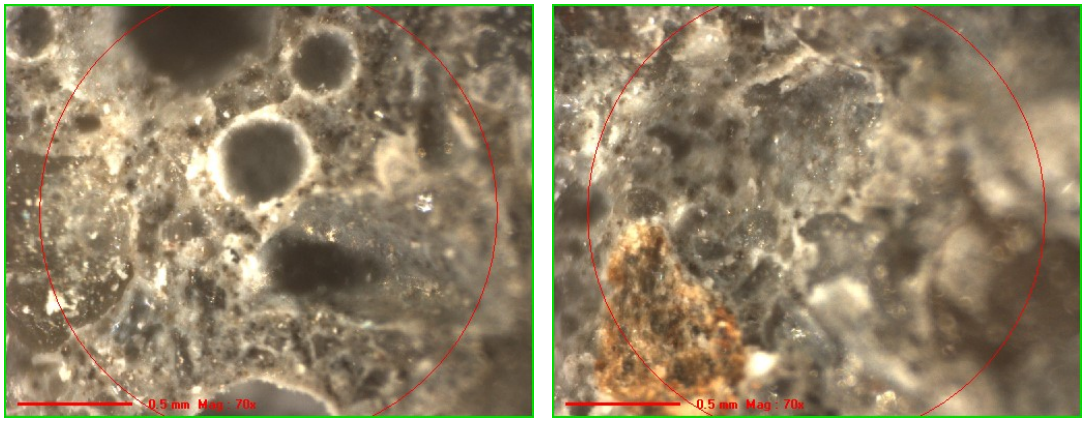


Figure 6-6: Examples of the selected points for analysis for M_{SF5}-0.380-50% RH.

Table 6-3: Details on the location of the points for M_{SF5}-0.380-50% RH.

	X_1	X_2	X_{13}
Y_1	P1	P7	P73
Y_2	P2	P8	P74
Y_3	P3	P9	P75
Y_4	P4	…	P76
Y_5	P5	…	P77
Y_6	P6	…	P78

As explained previously, the chloride profiles were constructed by first averaging the counts per second (CPS) values from P1 to P6 on X_1 coordinate. This process was repeated for X_2 to X_{13}. There were therefore 13 mean CPS values from X_1 to X_{13}. These values were then plotted against depth (mm). The area covered has a dimension of 10 mm width and 24 mm length, also measured from centre of beam. The distance, D between X-ray beam to the sample surface on both wet and dry side was also measured as additional information. The distance was measured from centre of beam to the sample surface for each of the six points on the X coordinate closest to the wet side (X_1). The values were then averaged. These steps were repeated for the dry side. This is shown in Figure 6-7. D indicates the measured distance while r is the radius of the circular X-ray beam. Please note the image is not to scale. The average distance from the centre of the X-ray beam to the sample surface on the wet side was 1.08 mm while that of the dry side was 1.23 mm.

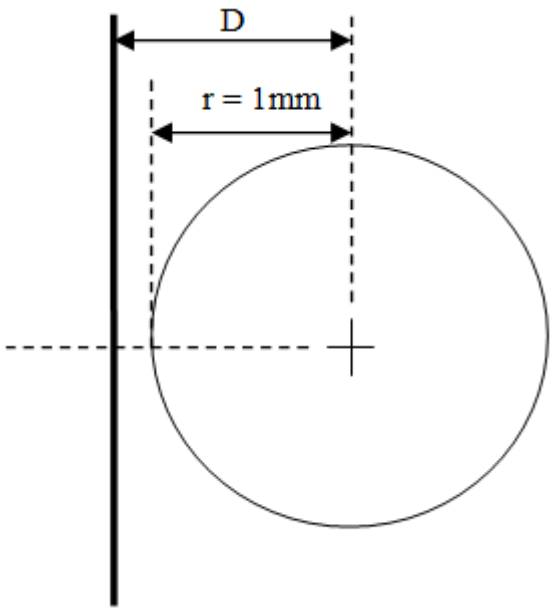


Figure 6-7: Distance between X-ray beam to the sample surface for M_{SF5}-0.380-50% RH.

For all samples, the analysis was carried starting from the wet side and ending on the dry side. Table 6-4 shows the operating conditions employed for the determination of chloride profile of the samples as received (no drying and grinding). The analysis was carried out in ambient condition (i.e. no vacuum) because wet sample outgassing might

occur in vacuum environment and thus will put the equipment at risk. A 25 μm aluminium filter was employed to improve the detection of chloride peak by removing rhodium spurious peaks overlap with the chloride peak.

Table 6-4: Operating condition for chloride profile determination.

Operating condition	Details
Beam voltage (kV)	20
Dead time (%)	30
Acquisition time (s Live)	100
Chamber	Air
Time constant (μs)	25.6
Filter	25 μm aluminium
Beam spot size	2 mm

After the measurement in the as-received condition, samples M_{OPC}-0.380-33% RH, M_{Slag70}-0.391-33% RH, M_{Slag70}-0.391-33% RH (Replicate), and M_{SF5}-0.381-33% RH were ground using Struers silicon carbide paper of successively finer grit sizes from 80 to 120. After each grinding session, the samples were cleaned using compressed air to remove dirt and debris. Each sample was then re-analysed to study the effect of surface grinding on the chloride profiles.

Sample M_{SF5}-0.380-50% RH was dried in oven at 50^0C until constant mass, which took about 25 days, and re-analysed to study the effect of oven drying on the chloride profiles. This sample was not ground which means the surface to be analysed was uneven. Samples M_{Slag40}-0.386-33% RH and M_{OPC}-0.380-33% RH were freeze dried until constant mass, which took approximately 42 and 21 days respectively, and re-analysed. The procedure for sample freeze drying was explained in Chapter 3. Sample M_{Slag40}-0.386-33% RH was not ground while sample M_{OPC}-0.380-33% RH was ground prior to being freeze dried for the study on the effect of grinding on the chloride profiles. Sample M_{OPC}-0.380-33% RH was used in both the study on the effect of sample grinding and sample freeze drying on the chloride profiles.

At the end of each sample preparation (grinding, oven drying, or freeze drying), each sample was placed on the stage at the same position as that of the first measurement. The operating condition as described in Table 6-4 was employed for chloride profile determination of the ground, oven-dried, and freeze-dried samples. This is to ensure comparability of the results obtained before and after sample preparation. After the measurement on the ground surface, sample M_{Slag70}-0.391-33% RH was further ground with silicon carbide paper of grit 500 and finally 1200. Subsequently, the sample was further analysed using the operating condition as listed in Table 6-4 to complete the study on the effect of surface grinding on the chloride profiles.

The background spectrum was subtracted manually based on the background subtraction method proposed by Ernst et al. [2012] which is explained in Chapter 3. The net counts obtained after the manual background subtraction were converted into counts per second by dividing each values with the acquisition time used.

6.2.2 Results and discussions

The effect of the different parameters on chloride profiles is presented and discussed. The parameters are binder type, w/b ratio, drying method (oven drying at 50^0C and freeze drying), and grinding.

Effect of binder type

Figure 6-8 shows the effect of different binder types on the chloride profiles. The samples were analysed as-is which means no grinding and drying were carried out prior to the μXRF analysis. Each point is an average of ten measurements except the last point of sample M_{OPC}-0.380-33%RH and the last point of sample M_{SF5}-0.381-33%RH which is an average of seven and nine measurements respectively. The error bars represent the standard error for the mean value.

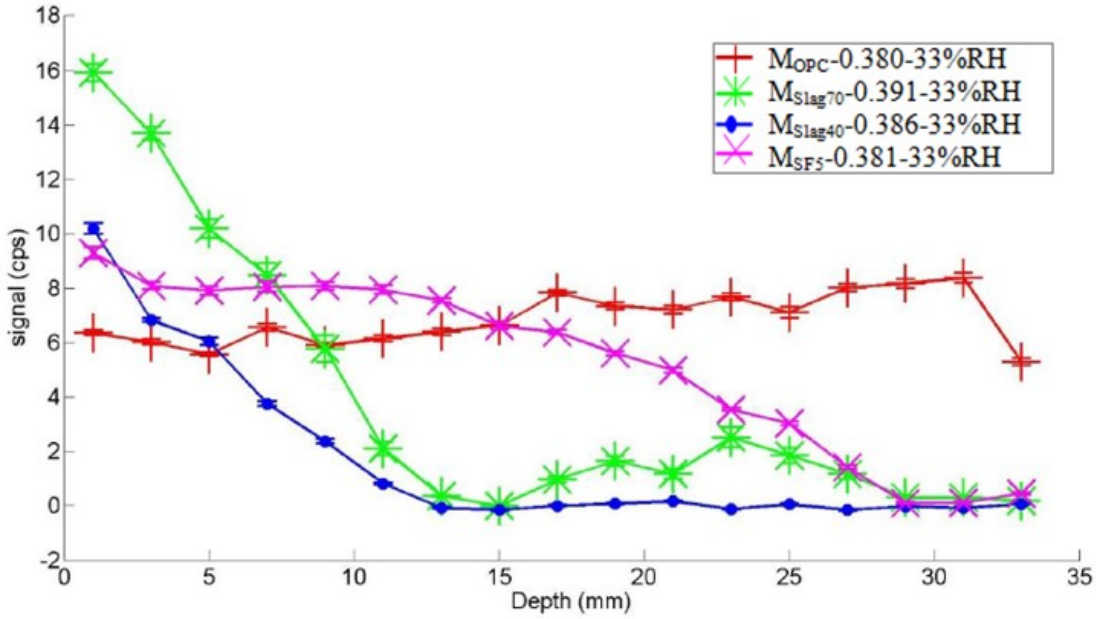
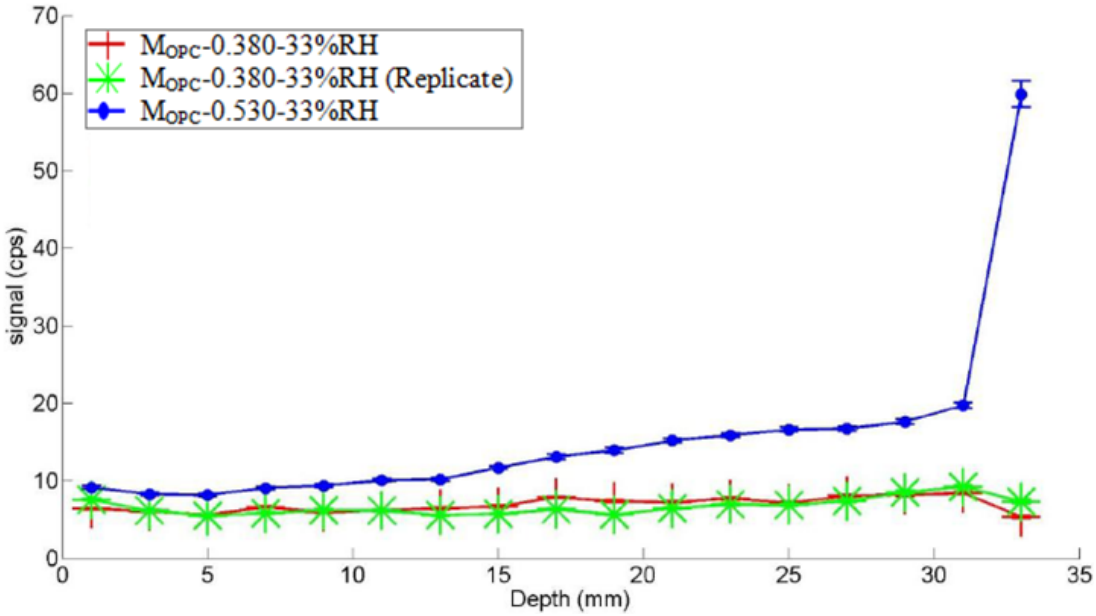


Figure 6-8: Effect of binder type on chloride profiles of the mortars.

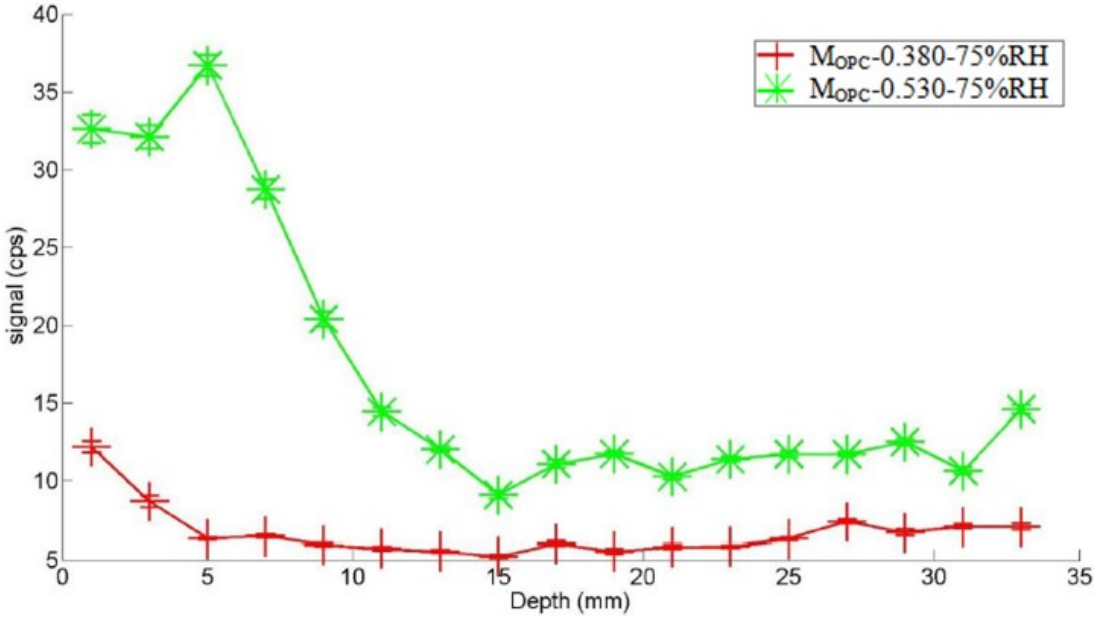
As seen in Figure 6-8, chloride has penetrated throughout sample M_{OPC}-0.380-33%RH. Chloride has penetrated approximately 13 mm into samples M_{Slag70}-0.391-33%RH and M_{Slag40}-0.386-33%RH. Chloride has penetrated to a depth of 30 mm in sample M_{SF5}-0.381-33%RH. The results show that the use of supplementary cementitious materials is very effective in supressing chloride ingress. This is due to the well-known pozzolanic reaction of supplementary cementitious materials that form additional hydrates in particular C-S-H, causing densification and pore refinement. The effect is the reduction in transport properties and therefore an increase in its resistance to the ingress of deleterious ions. The results also show that μXRF has sufficient sensitivity to detect changes in transport properties between different binder types.

Effect of w/b ratio

Figure 6-9 shows the effect of w/b ratios on the chloride profiles of samples with OPC as the binder. Each point is an average of ten measurements except the last point of sample M_{OPC}-0.380-33%RH (Figure 6-9 (a)) and the first point of sample M_{OPC}-0.380-75%RH which are an average of seven measurements. The error bars represent the standard error for the mean value.



(a)



(b)

Figure 6-9: Effect of w/b ratio on chloride profiles for samples exposed to the drying environment of (a) 33% RH and (b) 75% RH.

Effect of w/b ratio on the chloride ingress in this study depends on the composition of the binder. For samples with pure OPC as the binder, the results show that chloride has penetrated through the thickness. Furthermore, the sample with higher w/b ratio shows higher chloride concentration throughout and a strong gradient is seen near the near the wet side exposed to chloride solution. Furthermore, the data shows

precipitation of chloride salt occurred near the dry side of sample at higher w/b ratio and exposed to 33% RH on the dry side (Figure 6-9 (a)). This did not occur for sample exposed to 75% RH (lower moisture gradient driving wick action) and samples of the lower w/ b ratio. This can be explained by the fact that higher w/b ratio leads to a more porous mortar which in turn increases chloride ingress. For sample exposed to 75% RH, the chloride gradient was also higher for higher w/b ratio however no precipitation near the dry side was observed. This is shown in Figure 6-9 (b).

For all samples containing the supplementary cementitious materials, the penetration length was minimally affected by the w/b ratio. This is unexpected since theoretically, higher w/b ratio would results in a more porous samples and thus deeper chloride penetration in comparison to the lower w/b ratio, as seen in samples containing OPC (CEM I) only. There are two possible explanations for the minimal effect of w/b ratio on the chloride profile. First, higher w/b ratio increases the number as well as the size of capillary pores. On the contrary, the addition of supplementary cementitious materials (SCMs) modifies capillary structure of concrete and tends to densify the paste matrix. The effect of higher w/b ratio therefore could be suppressed by the effect of the addition of SCMs on the porosity and permeability of the paste. Second, the effect of w/b ratio might be unobserved due to the insufficient sensitivity of the measurement operating conditions, which was carried out as-received in air (not vacuum) and without any surface preparation. In order to overcome this, a more appropriate sample preparation and optimised operating parameters are required.

Effect of sample drying

Figure 6-10 shows the chloride profiles of sample M_{SF5}-0.380-50% RH, before and after-drying in an oven at 50^0C. Both analyses were carried out in air chamber. Each point is an average of six measurements. The error bars represent the standard error for the mean value. As seen in Figure 6-10, chloride profile of the sample before oven drying is significantly different from that after drying at 50^0C. Chloride has penetrated approximately 11 mm into the un-dried sample while chloride seems to penetrate the entire length of the dried sample. The measured chloride contents were significantly higher throughout for the dried sample. Thus, the chloride profile was disturbed during oven-drying. This shows that oven-drying removes water very rapidly and this causes a redistribution of chlorides within the sample. Essentially, bulk movement of the pore

water during rapid drying causes the internal dissolved chloride ions to shift towards the sample surface via capillary effects, and therefore increasing the measured chloride contents on the surface.

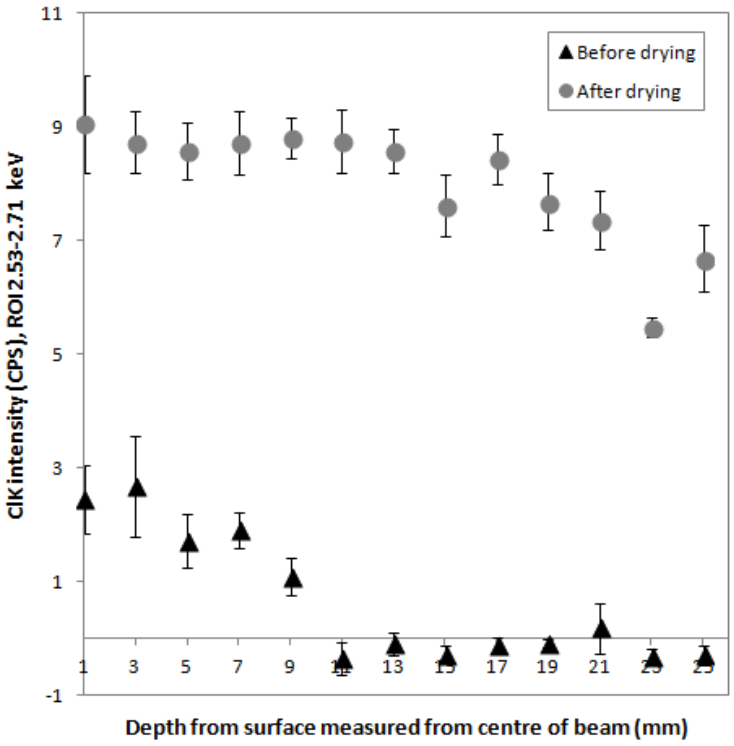
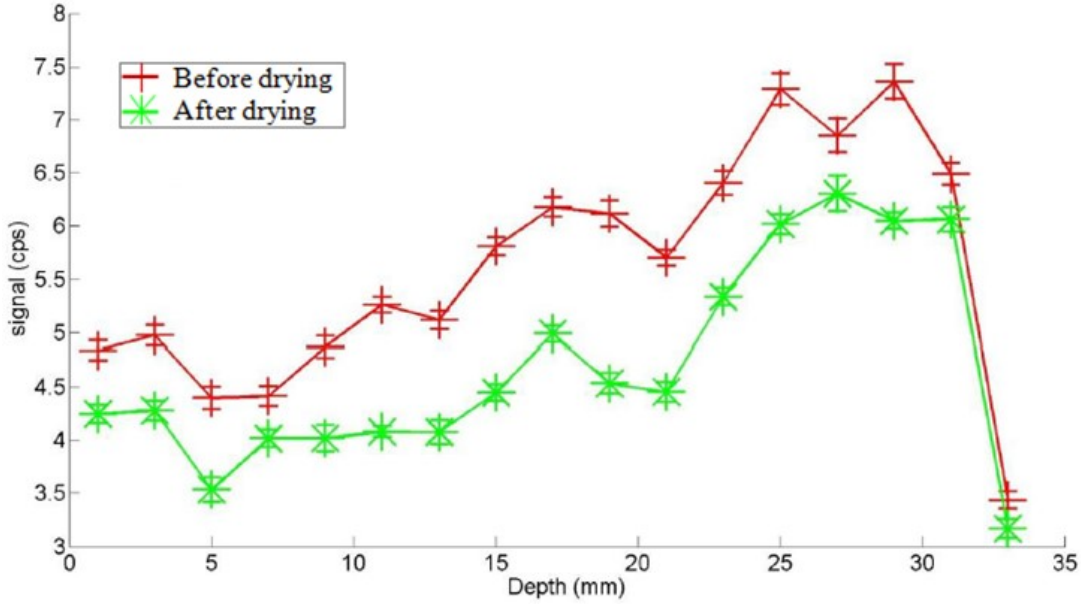
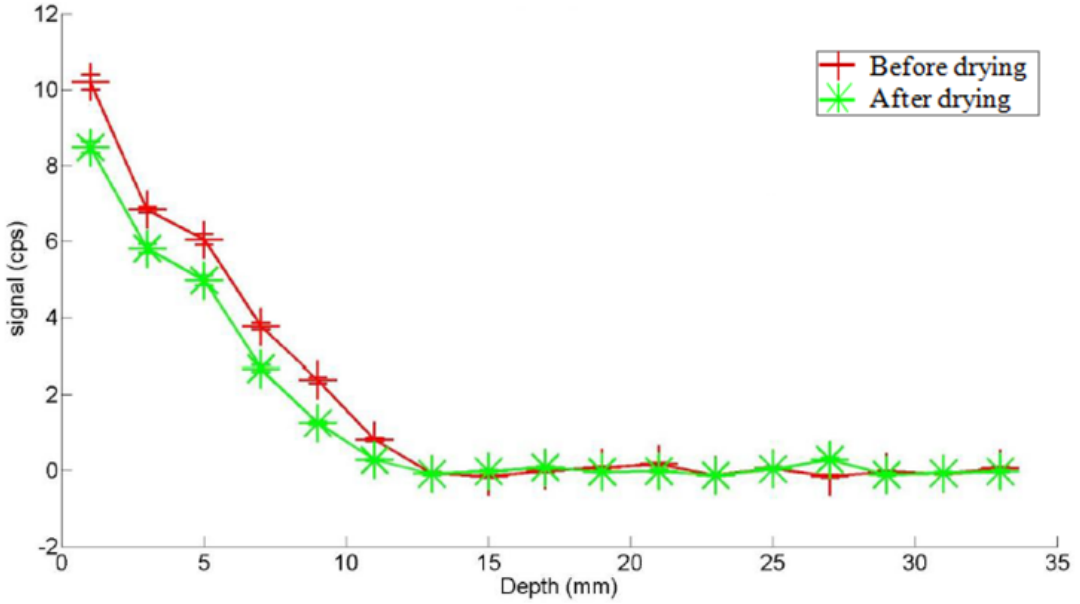


Figure 6-10: Chloride profiles of before and after drying in oven at 50^{0}C for sample M_{SF5}-0.380-50%RH.

Figure 6-11 shows the chloride profiles of samples M_{OPC}-0.380-33%RH and M_{Slag40}-0.386-33%RH, before and after-freeze drying. Each point is an average of ten measurements. The error bars represent the standard error for the mean value. As seen in Figure 6-11 (a) and (b), freeze-drying preserves the chloride profiles much better than oven-drying. The measured signal for chloride was slightly lower (by approximately 20%) after drying, but alteration to the profiles including the penetration depth was insignificant. This shows that freezing the sample rapidly and subsequent drying by sublimation prevents additional movement of chlorides leaving the chloride profiles almost unaffected.



(a)



(b)

Figure 6-11: Chloride profiles of before and after freeze drying for samples (a) M_{OPC}-0.380-33%RH and (b) M_{Slag40}-0.386-33%RH.

Effect of sample grinding

Figure 6-12 shows the effect of surface treatment (grinding) on the chloride profiles of sample M_{Slag70}-0.391-33% RH. Each point is an average of ten measurements. The error bars represent standard error of the mean value. The analysis was done twice on

the sample surface ground with silicon carbide paper of grit 120 hence the numbers in parentheses of Figure 6-12.

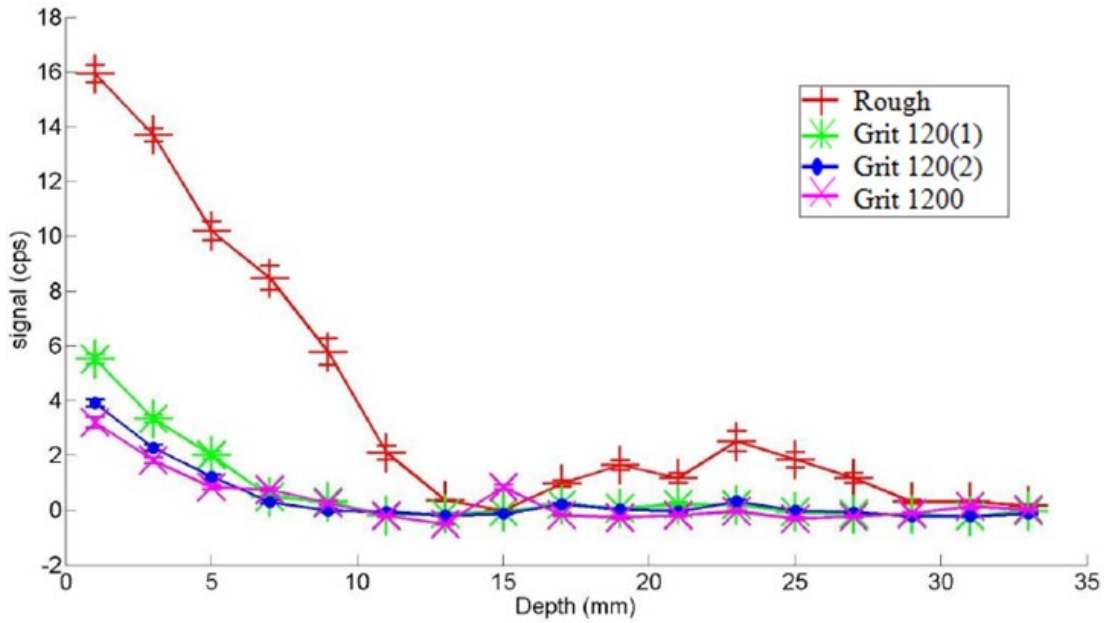


Figure 6-12: Effect of sample grinding on the chloride profiles of M_{Slag70}-0.391-33%RH.

As seen in Figure 6-12, sample grinding tends to decrease the measured chloride intensity. Spatial variability of chloride signal also decreased (i.e. less fluctuations) for measurements made on ground surface. These effects can be explained by considering the phases of the analysed surface. It is important to recall that the cylindrical samples were manually split in their longitudinal direction which means they did not undergo any cutting or grinding before analysis. Therefore, when the sample was analysed as-is, the measured surface corresponded essentially to the fractured surface. Cracking is likely to occur through the weakest regions of mortar which is the paste cement matrix and the aggregate paste interface [Grassl et al., 2010; Wu et al., 2015]. Therefore, it is very likely that the analysed surface would contain a higher amount of cement paste (and therefore more chloride) than if the measurement was made on a random flat section through the sample. On a fractured surface, it is also likely that a substantial portion of exposed aggregate particles will be covered with cement paste.

All these heterogeneities will be removed when the sample is ground flat, essentially producing a random section that is more representative of the sample. This is illustrated in Figure 6-13. Based on these reasoning, the original fractured surface has higher amount of cement paste which contains chloride ions, leading to higher chloride intensity compared to the flat ground surface. Furthermore, a ground surface contains less heterogeneities and therefore producing a more stable profile with less spatial variability. Figure 6-14 (a) shows the analysed surface of sample M_{OPC}-0.380-33% RH before grinding while Figure 6-14 (b) shows the analysed surface of the same sample after grinding with silicon carbide paper of grit 120. The ground surface is clearly more uniform, contain less debris and show better phase separation.

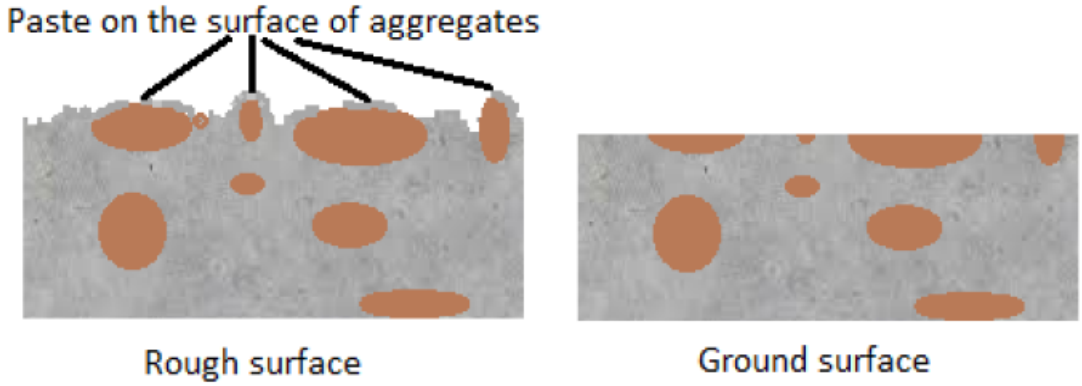
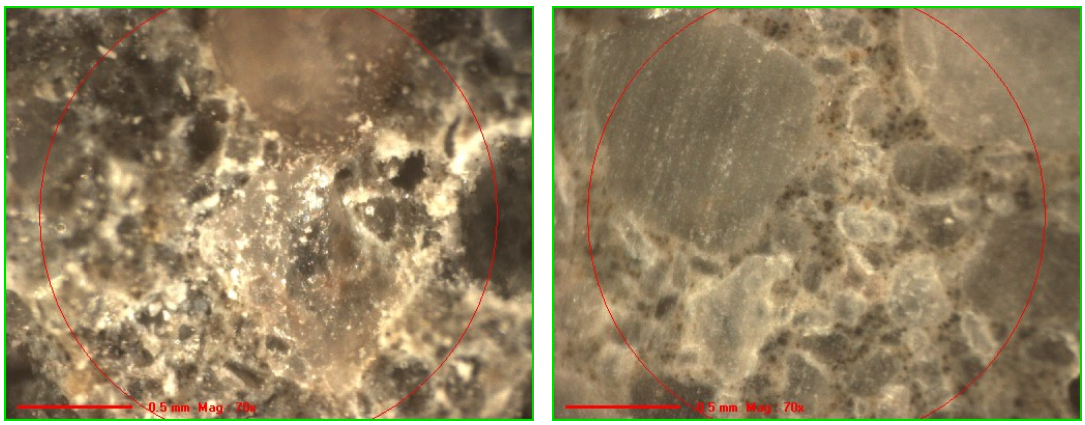


Figure 6-13: Schematic of rough (left) and ground surface (right) [Marin-Cudraz, 2015].



(a) **(b)**

Figure 6-14: Analysed surface of sample M_{OPC}-0.380-33% RH (a) as-is and (b) ground with silicon carbide paper of grit size 120.

As seen in Figure 6-14 (b), aggregates are more visible when the sample surface was ground. This means more aggregates and therefore less cement paste region were analysed on the ground sample. The aggregates were also siliceous which means the abundant element was silicon. These factors might contributed to the lower and more representative intensity of chloride measured on the ground surface in comparison to the one measured on the uneven, un-ground surface.

One of the major concerns about grinding was the risk of contamination of the samples. Dust and debris produced during the dry-grinding might accumulate in the pores and crack of the sample. An air duster was used to remove the dirt and debris at the end of each grinding session, however some residues might remain. Theoretically, contamination will result in flatter chloride profiles as well as modify the penetration depth of chloride since dust containing chloride would contaminate the whole surface of the ground sample. However as shown in Figure 6-12, the profile and penetration length of chloride measured on ground surface were almost similar to those measured on the uneven surface. Therefore, we can conclude that contamination of the analysed surface due to grinding has minimal effect on the chloride profiles.

6.3 Study on chloride ingress in mortars using dead time approach

In this section, cement paste regions of mortar sample were located using the proposed dead time approach presented in Chapter 4. The chloride content was then measured on these regions via μXRF and the results compared to that obtained by the conventional profile grinding and titration method.

6.3.1 Methodology

The sample used for this study was M_{OPC}-0.380-33% RH (Replicate). The final grit size of silicon carbide paper used to grind the sample was 120 since further grinding using silicon carbide paper of grit 1200 has minimal effect on the chloride profile (as shown in Figure 6-12). As reported in Chapter 6.2.2, sample grinding decreases the chloride intensity, however the penetration depth remains similar to the un-ground sample. It is also very difficult to locate paste regions on rough fractured surfaces using the dead time approach. Furthermore, grinding samples produces uniform surface conditions for the purpose of data comparison between different samples. For these

reasons, we decided to grind the sample so that more representative results can be obtained.

The sample was also freeze dried until constant mass, which took 114 days. The sample was assumed to have reached constant mass when the mass loss was less than 0.01% in 24 hour. Freeze drying was chosen as the drying method since it preserves the chloride profile as shown in Chapter 6.2.2. During data acquisition, the sample was positioned on the Plexiglas stage in a way that the side exposed to 6 wt% NaCl solution was on the left. The sample was secured to the stage using Blu Tack. For selecting the paste regions, the sample was divided vertically into 5 mm strips. In each strip, ten points which visually appeared to be paste matrix were selected. Figure 6-15 shows two of the selected points for analysis. The tiny red circles in Figure 6-15 indicate the sampling points analysed by the 30 μm beam size.

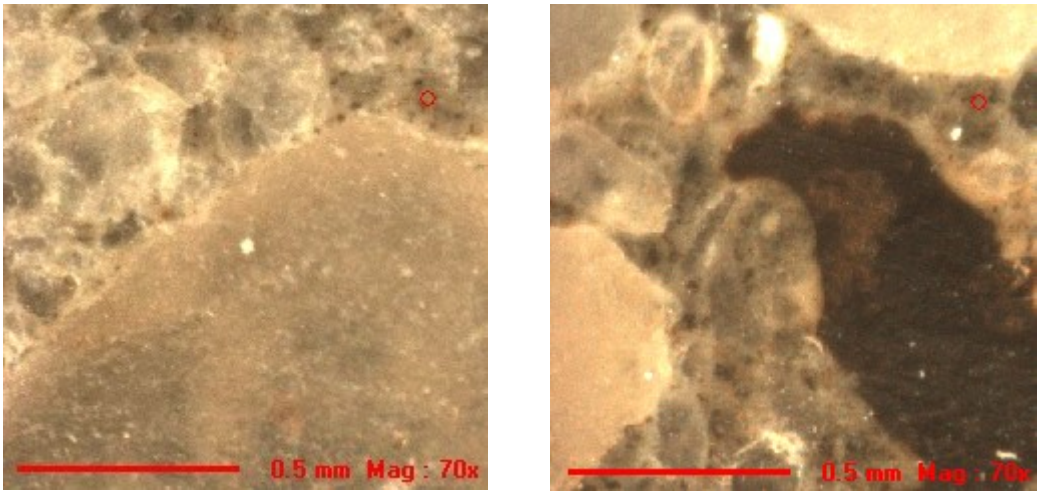


Figure 6-15: Examples of the selected points for analysis on MOPC-0.380-33% RH (Replicate).

In addition, the dead time achieved at each point should be in the range of 38-42% when the set of operating condition in Table 6-5 was employed. The same set of operating condition was employed to analyse the calibration paste samples with known chloride content as presented in Chapter 5. The analysis was carried out starting from the side exposed to the sodium chloride solution and ended at the side exposed to 33% RH drying environment. The background spectrum was subtracted manually as explained in Chapter 3. The net counts obtained after the manual background subtraction for each point was converted into counts per second by dividing the value with the acquisition time used which was 200 s.

Table 6-5: Operating condition for the study on chloride ingress using dead time approach.

Operating condition	Details
Beam voltage (kV)	30
Beam current (μA)	170
Acquisition time (s Live)	200
Chamber	Vacuum
Time constant (μs)	12.8
Filter	25 μm aluminium
Beam spot size	30 μm

The chloride intensity at each point was then converted to chloride concentration (percent by mass of cement) using the calibration graph in Chapter 5 (Figure 5-3). The equation was $y = 0.0296x + 0.009$ where y is the chloride content and x is the chloride intensity in counts per second. The chloride content for sample M_{OPC}-0.380-33% RH (Replicate) determined by μXRF was compared to the chloride content for sample M_{OPC}-0.380-33% RH determined by wet chemistry analysis. The data for the wet chemistry analysis was provided by Nilla Olsson.

6.3.2 Results and discussions

Figure 6-16 shows the chloride profiles determined by μXRF and wet chemistry analysis of samples M_{OPC}-0.380-33% RH (Replicate) and M_{OPC}-0.380-33% RH respectively. For μXRF, each point is an average of ten measurements. The error bars represent the standard error for the mean value.

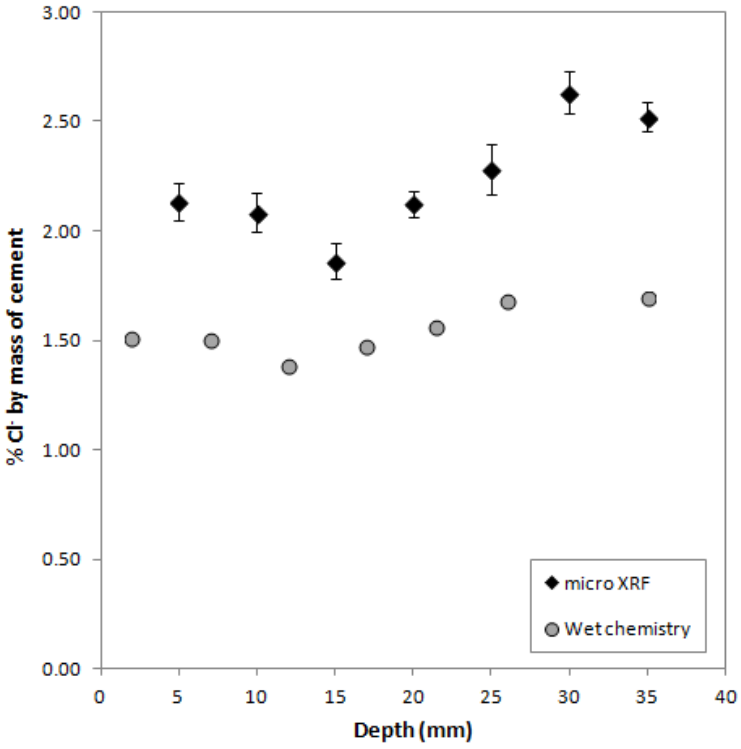


Figure 6-16: Chloride profiles determined by µXRF and wet chemistry.

As seen in Figure 6-16, chloride has penetrated throughout the length of both samples each determined by different techniques. This is in agreement with the results on the effect of binder type on chloride profiles as presented in Chapter 6.2.2 despite the difference in the operating condition employed as well as the point selection approach. The chloride profiles bear similar characteristics, however the chloride content determined by wet chemistry analysis is consistently slightly lower than that determined by µXRF. A possible explanation is the indirect comparison of the chloride content of the sample, which was based on measurements on two different samples. However, since the sample analysed by µXRF was a replicate of the sample analysed by wet chemistry technique, it was expected that the chloride content in both samples to be in close agreement. Therefore, indirect comparison of the chloride content is not sufficient to justify the results pattern in Figure 6-16.

As mentioned in Chapter 1, some studies have shown that the profile grinding and nitric acid extraction (wet chemistry analysis) for chloride analysis is prone to sample preparation errors and may not dissolve all chloride from powdered samples [Dhir et al., 1990; Wall & Nillson, 2008]. Incomplete extraction of chloride by nitric acid from powdered samples might explain the lower chloride content as determined by wet

chemistry analysis in comparison to the chloride content determined by μXRF. If the extraction of chloride by nitric acid from powdered samples is complete, the new chloride contents should be higher than the existing values in Figure 6-16 due to the presence of more chloride ions. As for the μXRF, the matrix effects (absorption and enhancement effect) were not corrected in this study. This might also contribute to the slightly higher chloride content determined by μXRF than that determined by wet chemistry analysis. If the matrix effects are corrected, the new chloride contents should either be higher than the current values in Figure 6-16 if the effect of enhancement is corrected or lower than the current values in the same figure if the effect of positive absorption is corrected.

6.4 Study on sulphate ingress in concretes using dead time approach

The paste regions in concrete sample were located using the dead time approach as presented in Chapter 4 and analysed for sulphate content.

6.4.1 Methodology

Sample casting

For the study on sulphate ingress, concrete samples were prepared, exposed to sulphate solution and analysed. The binder type was Portland cement CEM I. The oxide composition and loss on ignition (LOI) are shown in Table 6-6. The calculated Bogue composition of the cement was 53.1% C_3S, 19.1% C_2S, 10.8% C_3A, and 7.2% C_4AF by mass. The specific gravity and fineness of the cement were 3.06 and 2905 cm^2/g respectively. Thames Valley sand and gravel were used as fine aggregates and coarse aggregates respectively. The maximum particle size for sand and gravel was 5mm and 10mm respectively. The physical properties of the fine and coarse aggregates are shown in Table 6-7.

Table 6-6: Oxide composition and LOI of the CEM I.

Oxide composition									Loss on ignition (%)
CaO	SiO_2	Al_2O_3	Fe_2O_3	MgO	Na_2O	K_2O	SO_3	Cl^-	
63.4	20.8	5.4	2.4	1.5	0.3	0.7	2.9	<0.01	2.1

Table 6-7: Saturated surface dry (SSD) specific gravity, moisture content, and absorption of the aggregates.

Property	Sand	Gravel
Specific gravity (SSD)	2.6	2.51
Moisture content	0.25	0.40-0.43
24-hr absorption (%)	0.62	0.82-0.86

The proportion of cement, tap water, and aggregates were calculated based on absolute volume method which assumes the volume of a fully compacted concrete sample equals to the sum of the volumes of all components [Neville, 2011]. The amount of water absorbed by the aggregates when the concrete is in a fresh state was also corrected to ensure the targeted free water/cement ratio is achieved. The total aggregate volume fraction was 70% and sand-to-total aggregate ratio was 0.4. The measured slump for the concrete mix was in the range of 90 to 100mm, which indicates high workability. Table 6-8 shows the mix proportion of concrete prepared for this study.

Table 6-8: Mix proportion of the concrete.

Free w/c ratio	Cement (kg/m^3)	Sand (kg/m^3)	Gravel (kg/m^3)	Aggregate volume fraction (%)
0.4	345	726	1090	70

Materials were batched by mass. Cement and aggregates were first dry mixed in a pan mixer. Then, water was added to the dry mixture and mixed for 3 minutes. The mix was compacted in two layers in steel cylindrical moulds. The compaction was done using a vibrating table with adjustable intensity. The compaction for each layer was considered sufficient when no significant air bubbles escaped the surface. The compacted samples were covered with plastic sheet and wet hessian for the first 24 hour at room temperature. At the end of the 24 hour, samples were de-moulded and wrapped in cling film and plastic bags at 20^0C for seal curing until the age of 28 day.

Sample exposure

Subsequently, the concrete sample was immersed in shallow 5% sodium sulphate (Na_2SO_4) solution for 35 days. The minimum assay of the Na_2SO_4 was 99%. The concentration was chosen to simulate an environment with high sulphate content as well as to accelerate sulphate penetration into the samples [Tittelboom et al., 2013]. Prior to the immersion, the curved surface of each sample was wrapped with two layers of waterproof adhesive tape to allow unidirectional sulphate penetration. Figure 6-17 shows the sulphate penetration test setup which was inspired by the test setup for chloride penetration.

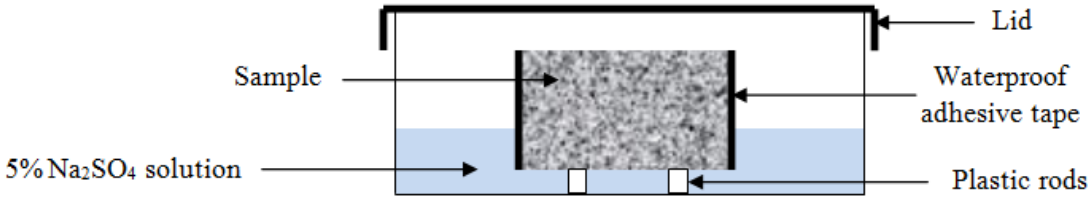


Figure 6-17: Sulphate penetration test setup.

Data acquisition with µXRF

At the end of the exposure period, the sample was sectioned into two halves. One half was further sectioned vertically to produce a sample of approximately 10 mm in thickness for µXRF analysis. The cutting of sample was carried out using a diamond abrasive cutter with water as the coolant. Then, the sectioned sample was weighed and immersed in liquid nitrogen for freeze drying as explained previously in Chapter 3. The sample was assumed to have reached constant mass when the mass loss was no more than 0.02% in 24 hour period. The drying process for the sample took approximately 100 days to reach constant mass. The sample was then sealed in polythene sample bags and placed in desiccators to prevent from carbonating until the time of testing.

Prior to µXRF analysis, one sectioned surface of each sample was ground to a flat surface. The final grit size of silicon carbide paper used for grinding was 120. The grinding process was carried out using a Struers LaboPol-5 machine with adjustable speed. During data acquisition, the sample was positioned on the Plexiglas stage in a

way that the side exposed to Na_2SO_4 solution was on the left. The sample was secured to the stage using Blu Tack. For selecting the paste regions, the sample was divided vertically into 2 mm strips. In each strip, ten points which visually appeared to be paste matrix were selected. The total vertical strip was 24. Figure 6-18 shows examples of two of the selected points for analysis. The tiny red circles in Figure 6-18 indicate the sampling points.

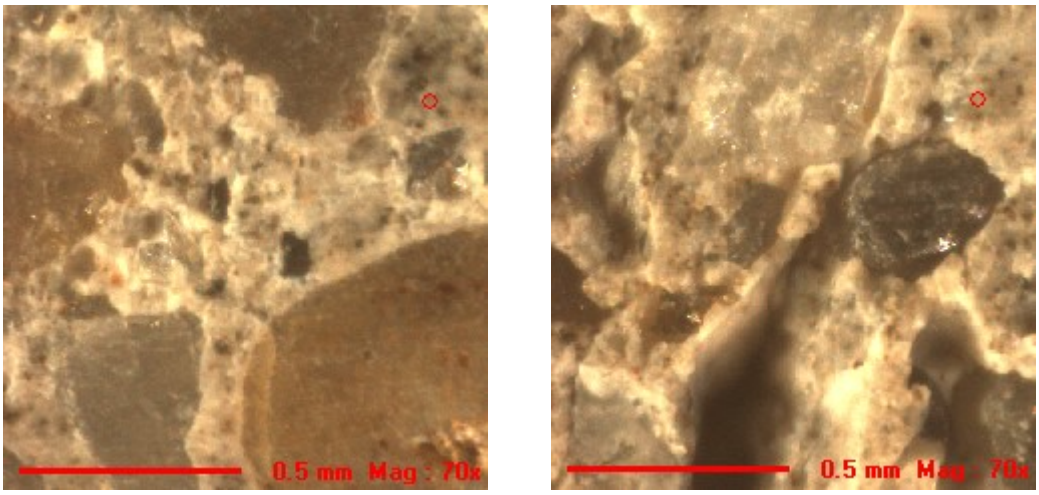


Figure 6-18: Examples of the selected points for analysis.

The dead time achieved at each point should be in the range of 38-42% when the set of operating condition in Table 6-9 was employed. The same set of operating condition was employed to analyse the calibration paste samples with known sulphate content as presented in Chapter 5. The analysis was carried out starting from the side exposed to the sodium sulphate solution. The background spectrum was subtracted manually as explained in Chapter 3. The net counts obtained after the manual background subtraction for each point was converted into counts per second by dividing the value with the acquisition time used which was 250 s.

Table 6-9: Operating condition for the study on sulphate ingress using dead time approach.

Operating condition	Details
Beam voltage (kV)	25
Beam current (μA)	90
Acquisition time (s Live)	250
Chamber	Vacuum
Time constant (μs)	12.8
Filter	No filter
Beam spot size	30 μm

The sulphur intensity at each point was then converted to sulphate concentration (percent by mass of cement) using the calibration graph for 28 day as presented in Chapter 5 (Figure 5-4). The equation was $y = 0.0212x - 1.9814$ where y is the sulphate content and x is the sulphur intensity in counts per second.

6.4.2 Results and discussions

Figure 6-19 shows the sulphate profile of the concrete sample exposed to 5% Na_2SO_4 solution for 35 days. Each point is an average of ten measurements. The error bars represent the standard error for the mean value.

As seen in Figure 6-19, sulphate has penetrated approximately 10-15 mm into the sample. The black line in the figure represents the baseline for the natural sulphate content of the cement which was 3.48%. However sulphate contents at several points were slightly lower than the natural sulphate content of the cement. This is probably due to the slight shift of the originally selected paste regions to a different location which might include a small portion of aggregates as the stage moved. This issue can be avoided by ensuring the sample is properly secured to the stage to minimise its movement as the stage moved.

Furthermore, due to the size of the X-ray beam and interaction volume, it is very difficult if not impossible to ensure that the analysed volume of material do not contain some amount of fine aggregates. Presence of small aggregate particles within the X-

ray sampling volume will inevitably dilute the collected sulphate signal and therefore giving slightly lower than expected sulphate contents. Related to this, it should be noted that the calibration graph used (Figure 5-4) was obtained from analyses of neat cement paste samples and therefore would not be affected by aggregate sampling. Nevertheless, the discrepancies are relative small and it is very encouraging the find that the method is able to detect and measure the penetration of sulphate.

Due to time constraint, the sulphate profile in Figure 6-19 determined by µXRF could not be compared to sulphate profile determined by other analytical technique such as the conventional wet chemistry analysis. This is therefore included in the future work for the continuation of this study.

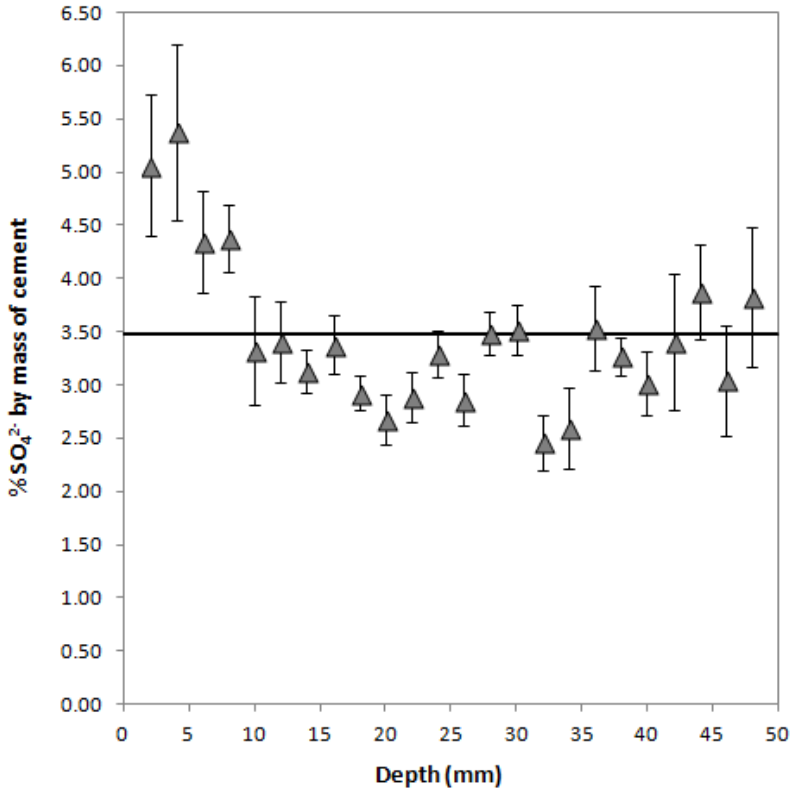


Figure 6-19: Sulphate profile of the sample exposed to 5% Na_2SO_4 solution for 35 days

6.5 Conclusions

This aim of this Chapter was to investigate the effects of drying and surface roughness to ascertain the most appropriate sample preparation method for studying transport properties using μXRF. This chapter also looked at the effects of binder type and w/b ratio on transport via wick action and to demonstrate the application of the methods developed in Chapters 4 and 5 for quantitative analysis of chloride and sulphate.

Results show that oven-drying at 50^0C distorts the chloride ingress profiles and produces chloride contents higher than expected throughout the sample thickness. This is due to movement of pore water containing dissolved chloride during the drying process causing redistribution of chlorides within the sample and increasing the chloride content at the measurement surface. Freeze-drying was able to preserve the chloride profiles much better than oven drying. It produces identical chloride penetration depths to that measured before drying. This shows that unlike oven-drying, movement of pore water containing dissolved chloride within the sample ceased instantly during rapid freezing in liquid nitrogen and that subsequent drying by sublimation does not affect the original chloride profile.

Sample grinding produces a clean, uniform and representative surface for μXRF analysis. This decreases the fluctuations in measured signals. The intensity of chloride measured on a ground surface is lower than that measured on a fractured surface because the latter contain higher cement paste due to the nature by which the fracturing occurs (via cement paste matrix and aggregate-paste interface).

The results also show that chloride ingress is influenced by binder type and water/binder ratio. Supplementary cementitious materials is very effective in supressing chloride ingress via wick action. The findings from this Chapter provide evidence that μXRF has sufficient sensitivity to detect changes in transport properties of samples between different binder types, water/binder ratio and drying conditions. Furthermore, this chapter demonstrates the applicability of the proposed dead time approach (Chapter 4) and calibration method (Chapter 5) in quantitative analysis of chloride and sulphate in concrete samples.

Chloride profiles determined by μXRF were compared to those determined by wet chemistry (titration). Both methods produced profiles with similar characteristics and identical penetration depths. However, the chloride contents determined by wet chemistry analysis were consistently slightly lower than that determined by μXRF. This is possibly due to the incomplete extraction of chloride from powdered samples by nitric acid for titration.

Chapter 7 Conclusions and recommendations for further research

7.1 Main conclusions

The aim of this thesis was to develop, optimise, and exploit μXRF for characterisation of concrete and to study the transport of chloride and sulphate in cement-based materials.

Firstly, the effect of seven operating conditions of μXRF on its sensitivity to chloride and sulphate was investigated to understand factors influencing its accuracy and to determine its optimum operating conditions. The operating parameters are beam voltage, analysis chamber, filter, acquisition time, time constant, beam spot size, and dead time. The results show that the signal-to-noise ratio (SNR) and its corresponding limit-of-detection (LOD) for both chloride and sulphur improves when the analysis is carried out at higher voltages in the range of 25 – 50 kV. This is due to a shift of the bremsstrahlung radiation to higher energies at these beam voltages, and thus giving a more pronounced chloride and sulphur peaks in the collected spectrum. The results also improve for measurements executed in vacuum, but this requires sample to be dried. For moisture sensitive samples, analysis can be carried out in ambient environment. However, this produces lower SNR due to attenuation of emitted characteristic X-rays by gas molecules in the chamber.

For chloride analysis, the use of 25 μm aluminium filter is necessary to remove overlapping rhodium spurious peak which originated from the X-ray tube. This filter is not a requisite for sulphur analysis as its ROI does not overlap with the rhodium peak. Longer acquisition time gave better SNR and LOD in all cases. A time constant of 12.8 μs time constant and dead time between 30 – 50% were optimum. Furthermore, a beam spot size of 30 μm was superior to 1 or 2 mm in terms of improving the SNR and LOD of both chloride and sulphur. This is probably due to the design of the 30 μm poly-capillary which utilises a bundle of 3-5 μm fibres that produces a higher X-ray flux. At these optimum operating condition, the lowest achievable LOD for chloride is 0.007% by mass of cement (70 ppm) at 6000 s live acquisition time and for sulphur is 0.003% by mass of cement (30 ppm) at 3000 s live acquisition time.

Aggressive species including chloride and sulphate penetrate concrete mainly through the paste matrix since it is the main interconnected phase of significantly higher porosity than aggregates particles. Therefore, the ability to identify cement paste regions in concrete is important as it will aid the analyst to locate sampling points to avoid interference of signals from aggregate particles. An image analysis technique was developed to produce elemental mapping images with high contrast between the different phases of concretes which are coarse aggregates, fine aggregates, and the cement paste matrix. This method is based on combining the key and trace elemental maps to produce a composite map which can then be employed for locating the different phases in concretes. However, this approach is very time-consuming

A new approach for identifying cement paste regions in mortars and concretes was proposed in this thesis. The method is based on exploiting the changes in dead time when a 30 μm beam samples cement paste or aggregate regions. The magnitude of dead time is a function of the input count rate. Using one set of operating condition, the dead time achieved in aggregate particles abundant in silicon, calcium, and iron were in the range of 15-16%, 34-36%, and 41-44% respectively. The dead time achieved while analysing cement pastes with different w/c ratio and curing age were in the range of 28-32%. The dead time achieved at the interfaces varied between that of pure cement paste and aggregate regions. These results show that cement paste can be differentiated from aggregate particles on the basis of dead time. The main advantage of the dead time approach over elemental mapping and image analysis is speed and ease of use.

A series of calibration graphs was developed to enable quantitative analysis by converting measured chloride or sulphur intensity at each selected paste matrix to actual mass concentration. For a wide range of samples, a strong linear correlation (R^2 > 0.9) is observed between characteristic X-ray intensities for chloride (or sulphate) and the actual known amounts. This strong correlation is observed in cement paste samples with different w/c ratio, binder type, curing age, and drying condition. This is also observed even when samples were analysed in a wet state (as-is) in ambient environment (air chamber). These findings provide evidence that the measured characteristic X-ray intensities from μXRF and the observed correlations can be used as calibration for quantitative analysis of unknown samples. However drying

condition and sample moisture state has a major effect on the measured X-ray intensities. Wet samples produce lower X-ray intensities compared to dried samples. This is due to the attenuation of X-rays by the presence of water in moist samples. Therefore, it is very important that samples are pre-conditioned to a standard moisture state to ensure repeatable results and to allow meaningful comparison across different samples.

The effect of drying and grinding was investigated to establish an appropriate preparation method for μXRF analysis of mass transport processes in cement-based materials. Rapid drying for example in the oven at 50^0C distorts the chloride ingress profiles and produces chloride contents higher than expected. This is due to movement of pore water containing dissolved chloride during drying that causes a redistribution of chlorides within the sample and increasing the chloride content on surface. Freeze-drying was able to preserve chloride profiles much better, producing identical chloride penetration depths to that measured before drying. This shows that rapid freezing preserves the chloride spatial distribution and that subsequent drying by sublimation does not affect this. Furthermore, analysis on a flat ground surface provides more representative results than that on rough fractured surfaces. This is because fractures occur mainly through weakest phase, i.e. the hardened cement paste and the paste-aggregate interface. Fractured surface contains higher cement paste and this increases the measured chloride intensity.

Finally, quantitative analysis of chloride and sulphate by combining the proposed dead time approach and calibration graphs was demonstrated on a series of mortars and concretes. Results also show that chloride ingress is influenced by binder type and water/binder ratio. Supplementary cementitious materials are very effective in suppressing chloride ingress via wick action. Chloride profiles determined by μXRF were compared to those determined by wet chemistry (titration). Both methods produced profiles with similar characteristics and identical penetration depths. However, the chloride contents determined by wet chemistry analysis were consistently slightly lower than that determined by μXRF. This is possibly due to the incomplete extraction of chloride from powdered samples by nitric acid for titration.

The findings from this thesis provide evidence that μXRF has sufficient sensitivity to detect changes in transport properties of samples with different binder types, water/binder ratio and drying conditions.

7.2 Recommendations for further research

This thesis has proposed a procedure for quantification of chloride and sulphate in cement based materials. However, a major issue associated to quantitative analysis using XRF/μXRF techniques which is the matrix effects has not been addressed due to time constraints. It is known that matrix effects can cause non-linear behaviour between net intensities measured with XRF and concentration particularly on relatively thick samples. For analysis on thin samples, matrix effects can be neglected without major consequences. For future research, the matrix effects (absorption and enhancement) should be corrected in order to achieve more accurate results. Two common methods for correcting matrix effects are the influence coefficients method and fundamental parameters method. A more suitable method for the matrix effects corrections in cement-based materials needs to be investigated.

From the optimisation of the operating parameters of μXRF, the results show that the 30 μm beam spot is superior to the 1 and 2 mm beam in term of improving the SNR and LOD of chloride and sulphate. However, the 30 μm size is small in relative to the typical size of sample for analysis in the laboratory. Due to this, a large number of points needs to be analysed in order to obtain a result that is representative of the composition of the sample. Further work could be carried out to improve the accuracy and sensitivity of the method when using large beam spots.

The determination of LOD of chloride and sulphur has been carried out using one cement paste sample with chloride content of 0.50% by mass of cement, w/c ratio of 0.4, and cured for 28 day. Future work should involve the determination of LOD of chloride and sulphur on wider samples such as different chloride (or sulphur) content, w/c ratio, binder type, and curing age. The aim is to obtain a more representative LOD of chloride and sulphur which can be determined by μXRF.

The proposed approach for the identification of different phases of concrete by monitoring the change in dead time can be further developed and refined. Using one set of operating parameters, it was shown that this approach can differentiate three types of aggregates from the cement paste region, i.e. siliceous, calcareous and ferrous aggregates. However, there are other types of aggregates and other phases that exist in concrete. The quantification of chloride and sulphate using the combination of dead time approach for locating cement paste regions and the calibration graph could also be extended to a wider range of cement-based materials for a more comprehensive study. The concentration of the elements obtained from this approach then should be compared to other analytical techniques such as the conventional profile grinding and titration analysis to investigate the practicality and accuracy of this method.

References

Abbas, A., Carcasses, M. & Ollivier, J.P. (1999), Gas permeability of concrete in relation to its degree of saturation, Materials and Structures, Vol. 32, No. 1, pp. 3-8.

ACS Committee on Environmental Improvement (1983) Analytical Chemistry. Vol. 55, No. 14, pp. 2210-2218

Abdul Razak, H., Chai, H.K. & Wong, H.S. (2004), Near surface characteristics of concrete containing supplementary cementitious materials, Cement and Concrete Composites, Vol. 26, No. 7, pp. 883-889.

Alzyoud, S., Wong, H.S. & Buenfeld, N.R. (2016), Influence of reinforcement spacers on mass transport properties and durability of concrete structures, Cem. Concr. Res., 87, 31-44.

Alzyoud, S., Wong, H.S. & Buenfeld, N.R. (2014), Effect of spacers on concrete transport properties and chloride penetration, Concrete, Materials & Conservation, Structural Faults & Repair, Imperial College London, 8-10th July.

Anabitarte, F., Cobo, A., & Lopez-Higuera, J.M. (2012) Laser-induced breakdown spectroscopy: Fundamentals, applications, and challenges. ISRN Spectroscopy. Vol. 2012, pp. 1-12

Angst, U., Elsener, B., Larsen, C.K., & Vennesland, O. (2009) Critical chloride content in reinforced concrete – A review. Cement and Concrete Research. pp. 1122-1138

ASTM C1556 – 11a (2011) Standard test method for determining the apparent chloride diffusion coefficient of cementitious mixtures by bulk diffusion. ASTM International. United States

ASTM C1152/C1152M (2012) Standard test method for acid-soluble chloride in mortar and concrete. ASTM International. United States

Barnes, R. & Ingham, J. (2013) The chemical analysis of hardened concrete: results of a ‘round robin’ trial –Part I. Concrete. Vol. 47, No. 8, pp. 45-48

Barnes, R. & Ingham, J. (2013/2014) The chemical analysis of hardened concrete: results of a ‘round robin’ trial – Part II. Concrete. pp. 48-51

Bécares, V. & Blázquez, J. (2012) Detector dead time determination and optimal counting rate for a detector near a spallation source or a subcritical multiplying system. Science and Technology of Nuclear Installations. Article ID 240693. Vol. 2012, pp. 1-7

Bicchieri, M., Ronconi, S., Romano, F.P., Pappalardo, L., Corsi, M., Cristoforetti, G., Legnaioli, S., Palleschi, V., Salvetti, A., & Tognoni, E. (2002) Study of foxing stains on paper by chemical methods, infrared spectroscopy, micro-X-ray fluorescence spectrometry and laser induced breakdown spectroscopy. Spectrochimica Acta Part B. Vol. 57, pp. 1235-1249

British Standards Institution (1988) BS 1881-124:1988 Testing concrete – Part 124: Methods for analysis of hardened concrete. ISBN 0 580 16617 1

British Standards Institution (2011) BS EN 197-1:2011 Cement Part 1: Composition, specifications and conformity criteria for common cements. ISBN 978 0 580 76786 9

British Standards Institution (2013) BS EN 206:2013 Concrete – Specification, performance, production and conformity. ISBN 978 0 580 85966 3

Buenfeld, N.R., Shura-Daoudi, M-T., & McLoughlin, I.M. (1995) Chloride transport due to wick action in concrete. Proceedings of RILEM International Workshop on Chloride Penetration into Concrete. pp. 315-324

Buenfeld, N.R., Glass, G.K., Hassanein, A.M., & Zhang, J-Z. (1998) Chloride transport in concrete subjected to electric field. Journal of Materials in Civil Engineering. Vol. 10 (4), pp. 220-228

Buenfeld, N.R. & Wong, H.S. (2011), Assessing the durability of new concretes, 31st Cement and Concrete Science Conference, Novel Developments and Innovations in Cementitious Materials, 12-13 Sept, Imperial College London.

Castellote, M. & Andrade, C. (2001) Round-robin test on chloride analysis in concrete – Part II: Analysis of water soluble chloride content. Materials and Structures. Vol. 34, pp. 589-598

Cheng, L., Ding, X., Liu, Z., Pan, Q., & Chu, X. (2007) Development of a micro-X-ray fluorescence system based on polycapillary X-ray optics for non-destructive analysis of archaeological objects. Spectrochimica Acta Part B. Vol. 62, pp. 817-823

Chinchón-Payá, S., Aguado, A., Coloma, F., & Chinchón, S. (2013) Study of aggregate samples with iron sulfides through micro X-ray fluorescence (μXRF) and X-ray photoelectron spectroscopy (XPS). Materials and Structures. Vol. 48, Issue 5, pp. 1285-1290

Criss, J.W. & Birks, L.S. (1968) Calculation methods for fluorescent X-ray spectrometry – Empirical coefficients vs. fundamental parameters. Analytical Chemistry. Vol. 40, No. 7, pp. 1080-1086

Davis, J.M., Newbury, D.E., Rangaraju, P.R., Soundrapanian, S., & Giebson, C. (2009) Milli X-ray fluorescence X-ray spectrum imaging for measuring potassium ion intrusion into concrete samples. Cement & Concrete Composites. Vol. 31(3), pp. 171-175

Davis, J.M., Newbury, D.E., Fahey, A., Ritchie, N.W.M., Vicenzi, E., & Bentz, D. (2011) Bridging the micro-to-macro gap: A new application for micro X-ray fluorescence. Microscopy and Microanalysis. Vol. 17(3), pp. 410-417

De Vries, J.L. & Vrebos, B.A.R. (2002) Quantification of infinitely thick specimens by XRF analysis, In: Handbook of X-ray Spectrometry – Second Edition, Revised and Expanded. Marcel Dekker Inc. ISBN 0-8247-0600-5

Dehghanpoor Abyaneh, S., Wong, H.S. & Buenfeld, N.R. (2013), Modelling the diffusivity of mortar and concrete using a three-dimensional mesostructure with several aggregate shapes, Computational Materials Science, Vol. 78, pp. 63-73.

Dehghanpoor Abyaneh, S., Wong, H.S., Buenfeld, N.R. (2014), Computational investigation of capillary absorption in concrete using a three-dimensional mesoscale approach, Computational Materials Science, Vol. 87, pp. 54-64

Dehghanpoor Abyaneh, S., Wong, H.S. & Buenfeld, N.R. (2016), Simulating the effect of microcracks on the diffusivity and permeability of concrete using a three-dimensional model, Computational Materials Science, Vol. 119, pp. 130-143

Dhir, R.K., Jones, M.R., & Ahmed, H.E.H. (1990) Determination of total and soluble chlorides in concrete. Cement and Concrete Research. Vol. 20, pp. 579-590

Diamond, S. (1986) Chloride concentrations in concrete pore solutions resulting from calcium and sodium chloride admixtures. Cement, Concrete, and Aggregates. Vol. 8, pp. 97-102

EDAX (2009) EDAX Orbis Vision user's manual. Revision 1.00

EDAX (2010) EDXRF user training – ORBIS setup and hardware

Ernst, T., Berman, T., Buscaglia, J., Eckert-Lumsdon, T., Hanlon, C., Olsson, K., Palenik, C., Ryland, S., Trejos, T., Valadez, M., & Almirall, J.R. (2012) Signal-to-noise ratios in forensic glass analysis by micro X-ray fluorescence spectrometry. X-ray Spectrometry. pp. 13-21

Espen, P.V. (1998) Analytical Chemistry. Section 8.3 X-ray fluorescence spectrometry. Weinheim, WILEY-VCH

Glass, G.K. & Buenfeld, N.R. (1997) The presentation of the chloride threshold level for corrosion of steel in concrete. Corrosion Science. Vol. 39, No. 5, pp. 1001-1013

GlobalSino (2013) Sum Peaks/Peak pile-up in X-ray/EDS profiles – practical electron microscopy and database [Online] Available from: http://www.globalsino.com/EM/page3803.html [Accessed 13th October 2013]

Gondal, M.A., Yamani, Z.H., Hussain, T., & Al-Amoudi, O.S.B. (2009) Determination of chloride content in different types of cement using laser-induced breakdown spectroscopy. Spectroscopy Letters. Vol. 42, pp. 171-177

Goni, S. & Andrade, C. (1990) Synthetic concrete pore solution chemistry and rebar corrosion rate in the presence of chlorides. Cement and Concrete Research. Vol. 20, pp. 525-539

Grassl., P., Wong, H.S. & Buenfeld, N.R. (2010), Influence of aggregate size and volume fraction on shrinkage induced micro-cracking of concrete and mortar, Cement & Concrete Research, Vol. 40, pp. 1139-1148

Hands, G. & Armitt, T. (1998) Chapter 5 - Surface and internal defect detection, In: Handbook of Condition Monitoring – Techniques and Methodology. Chapman & Hall. ISBN 0 412 61320 4

Hansson, C.M. & Sørensen, B. (1990) The threshold concentration of chloride in concrete for the initiation of reinforcement corrosion. Corrosion rates of steel in concrete, ASTM STP 1065. pp. 3-16

Hausmann, D.A. (1967) Steel corrosion in concrete. How does it occur? Materials Protection. Vol. 6, pp. 19-23

Head, M.K., Wong, H.S., Buenfeld, N.R. (2006), Characterisation of 'Hadley' grains by confocal microscopy, Cement & Concrete Research, Vol. 36, No. 8, pp. 1483-1489.

Ho, Y.W. (2013) Determining the composition of concrete using micro X-ray fluorescence. MSc Dissertation. Imperial College London

Horiba (2016) X-ray generators – Experimental control [Online] Available from: http://www.horiba.com/scientific/products/x-ray-fluorescence-analysis/tutorial/x-ray-generators-experimental-control/ [Accessed 29th March 2016]

Hooton, R.D. (1986), Permeability and pore structure of cement pastes containing fly ash, slag, and silica fume, Blended Cements, ASTM STP 897, G. Frohnsdorff (eds.), American Society for Testing and Materials, Philadelphia, pp.128-143.

Houst, Y.F. & Wittmann, F.H. (1994), Influence of porosity and water content on the diffusivity of CO_2 and O_2 through hydrated cement paste, Cement and Concrete Research, Vol. 24, No. 6, pp. 1165-1176.

Hover, K.C. (2006) Chapter 26 - Air content and density of hardened concrete, In: Significance of Tests and Properties of Concrete & Concrete-Making Materials. ASTM STP 169D pp. 288-308

Kearton, B. & Mattley, Y. (2008) Laser-induced breakdown spectroscopy – Sparking new applications. Nature Photonics. Vol. 2, pp. 537-540

Kellner, R.A. (1998) Analytical chemistry. Section 7.2 Gravimetry. Weinheim, WILEY-VCH

Klinghoffer, O., Frolund, T., & Poulsen, E. (2000) Rebar corrosion rate measurements for service life estimates. ACI Fall Convention, Toronto, Canada

Korpa, A. & Trettin, R. (2006) The influence of different drying methods on cement paste microstructures as reflected by gas adsorption: Comparison between freeze-drying (F-drying), D-drying, P-drying and oven-drying methods. Cement and Concrete Research. Vol. 36, pp. 634-649

Labutin, T.A., Popov, A.M., Raikov, S.N., Zaytsev, S.M., Labutina, N.A., & Zorov, N.B. (2013) Determination of chlorine in concrete by laser-induced breakdown spectroscopy in air. Journal of Applied Spectroscopy. Vol. 80, No. 3, pp. 315-318

Labutin, T.A., Popov, A.M., Zaytsev, S.M., Zorov, N.B., Belkov, M.V., Kiris, V.V., & Raikov, S.N. (2014) Determination of chlorine, sulfur and carbon in reinforced concrete structures by double-pulse laser-induced breakdown spectroscopy. Spectrochimica Acta Part B. Vol. 99, pp. 94-100

Lachance, G.R. (1993) Correction procedures using influence coefficients in X-ray fluorescence spectrometry. Spectrochimica Acta. Vol. 48B, No. 3, pp. 343-357

Lachance, G.R. & Claisse, F. (1995) Quantitative X-ray fluorescence analysis – Theory and application. John Wiley & Sons Ltd. Chichester, ISBN 0471951676

Lambert, P., Page, C.L., & Vassie, P.R.W. (1991) Investigations of reinforcement corrosion. 2. Electrochemical monitoring of steel in chloride-contaminated concrete. Materials and Structures. Vol. 24, Issue 5, pp. 351-358

Lee, H.X.D., Wong, H.S., & Buenfeld, N.R. (2016), Self-sealing cracks in concrete using superabsorbent polymers, Cement and Concrete Research, Vol. 79, pp. 194-208.

Lee, H.X.D., Wong, H.S. & Buenfeld, N.R. (2010), The potential of superabsorbent polymer for self-sealing cracks in concrete, Advances in Applied Ceramics, Vol. 109, No. 5, pp. 296-302.

Lee, H.X.D., Wong, H.S. & Buenfeld, N.R. (2010), Self-sealing concrete using superabsorbent polymers, RILEM International Conference, Use of superabsorbent polymers and other new additives in concrete, Lyngby, 15-18 Aug, 171-178.

Liao, Y. (2007) Practical electron microscopy and database. [Online] Available from: http://www.globalsino.com/EM/ [Accessed 13th October 2013]

Lothenbach, B., Scrivener, K.L. & Hooton, R.D. (2011), Supplementary cementitious materials, Cement and Concrete Research, Vol. 41, pp. 1244-1256.

Maage, M., Helland, S.T., & Carlsen, J.E. (1994) Chloride penetration in high performance concrete exposed to marine environment. International RILEM Workshop on Durability of High Performance Concrete. pp. 194-207

Marin-Cudraz, F. (2015) Characterising non-saturated transport in mortars using micro X-ray fluorescence. MSc Dissertation. Imperial College London

Markowicz, A. (2011) An overview of quantification methods in energy-dispersive X-ray fluorescence analysis. Pramana-Journal of Physics. Vol. 76, No. 2, pp. 321-329

Martys, N.S. & Ferraris, C.F. (1997) Capillary transport in mortars and concrete. Cement and Concrete Research. Vol. 27, No. 5, pp. 747-760

McKetty, M.H. (1998) The AAPM/RSNA physics tutorial for residents – X-ray attenuation. RadioGraphics. Vol. 18, pp. 151-163

Mehta, P.K. (2000) Sulfate attack on concrete: Separating myths from reality. Concrete International. Vol. 22, Issue 8, pp. 57-61

Mehta, P.K. & Monteiro, P.J.M. (2006) Concrete: Microstructure, properties, and materials. McGraw-Hill Education. ISBN 978-0-07-179787-0

Mermet, J.M. (1998) Analytical Chemistry. Section 8.1 Atomic emission spectrometry. Weinheim, WILEY-VCH

Moradllo, M.K., Sudbrink, B., Hu, Q., Aboustait, M., Tabb, B., Ley, M.T., & Davis, J.M. (2017) Using micro X-ray fluorescence to image chloride profiles in concrete. Cement and Concrete Research. No. 92, pp. 128-141

Muller, U. (2004) The Micro-XRF – A new technique for the analysis of building materials. Construction Technology in Europe. Issue 26, pp. 3-4

Müller, U. & Rübner, K. (2006) The microstructure of concrete made with municipal waste incinerator bottom ash as an aggregate component. Cement and Concrete Research. No. 36, pp. 1434-1443

Nehdi, M.L., Suleiman, A.R., & Soliman, A.M. (2014) Investigation of concrete exposed to dual sulfate attack. Cement and Concrete Research. Vol. 64, pp. 42-53

Neville, A. (2004) The confused world of sulfate attack on concrete. Cement and Concrete Research. Vol. 34, pp. 1275-1296

Neville, A.M. (2011) Properties of concrete. Pearson Education Limited. Fifth Edition. ISBN 978-0-273-75580-7

Neville, A.M. & Brooks, J.J. (2010) Concrete Technology. Pearson Education Limited. Second Edition. Essex. ISBN: 978-0-273-73219-8

Newbury, D.E. (2009) Mistakes encountered during automatic peak identification of minor and trace constituents in electron-excited energy dispersive X-ray microanalysis. Scanning. Vol. 31 (8), pp. 1-11

Ngala, V.T., Page, C.L., Parrott, L.J., & Yu, S.W. (1995) Diffusion in cementitious materials: II. Further investigations of chloride and oxygen diffusion in well-cured OPC and OPC/30% PFA pastes. Cement and Concrete Research. Vol. 25, No. 4, pp. 819-826

NORAN Instruments (1999) Energy dispersive X-ray microanalysis: An introduction. Middleton, Wisconsin

NordTest Method NT Build 443 (1995) Concrete, Hardened: Accelerated chloride penetration

NordTest Method NT Build 208 (1996) Concrete, Hardened: Chloride content by Volhard titration. Edition 3

Ollivier, J.P., Maso, J.C. & Bourdette, B. (1995), Interfacial transition zone in concrete, Advanced Cement Based Materials, Vol. 2, pp. 30-38.

PANalytical B.V. (2006) Theory of XRF. Almelo, the Netherlands

Philips (2008) Inductively coupled plasma-atomic emission spectrometry (ICP-AES) [Online] Available from:

http://www.innovationservices.philips.com/sites/default/files/materials-analysis-icp-aes.pdf [Accessed 6th May 2013]

Pogge, R.W. (2013) Astronomy 350: Methods of astronomical observation and data analysis – Spectra of different atoms [Online] Available from: www.astronomy.ohio-state.edu/~pogge/Ast350/Labs/Lamps [Accessed 27th September 2013]

Poole, D.M. (n.d.) Kaye & Laby Tables of physical & chemical constants – 4.2.1 X-ray absorption edges, characteristic X-ray lines and fluorescence yields [Online] Available from: http://www.kayelaby.npl.co.uk/atomic_and_nuclear_physics/4_2/4_2_1.html

Potts, P.J. (2004) Chapter 7 X-ray fluorescence analysis, In: Soil and Environmental Analysis – Modern Instrumental Techniques. Marcel Dekker Inc. Third Edition. ISBN 0-8247-0991-8

Proverbio, E. & Carassiti, F. (1997) Evaluation of chloride content in concrete by X-ray fluorescence. Cement and Concrete Research. Vol. 27, No. 8, pp. 1213-1223

Richardson, I.G., Skibsted J., Black, L. & Kirkpatrick, R.J. (2010), Characterisation of cement hydrate phases by TEM, NMR and Raman spectroscopy, Advances in Cement Research, Vol. 22, Issue 4, pp. 233-248.

Rousseau, R.M. (2001) Concept of the influence coefficient. The Rigaku Journal. Vol. 18, No. 1, pp. 8-21

Šavija, B., Schlangen, E., Pacheco, J., Millar, S., Eichler, T., & Wilsch, G. (2014) Chloride ingress in cracked concrete: a laser induced breakdown spectroscopy (LIBS) study. Journal of Advanced Concrete Technology. Vol. 12, pp. 425-442

Schiessl, P. & Raupach, M. (1990) Influence of concrete composition and microclimate on the critical chloride content in concrete. Proceedings 3rd International Symposium on Corrosion of Reinforcement in Concrete. Elsevier Applied Science, Wishaw, UK. pp. 49-58

Schlegel, M.C., Mueller, U., Panne, U., & Emmerling, F. (2011) Deciphering the sulfate attack of cementitious materials by high-resolution Micro-X-ray diffraction. Analytical Chemistry. 83(10), pp. 3744-3749

Scrivener, K.L., Crumbie, A.K. & Laugesen, P. (2004), The Interfacial Transition Zone (ITZ) between cement paste and aggregate in concrete, Interface Science, Vol. 12, pp. 411-421.

Scruggs, B., Lee, A., & Jackson, M.D. (2014) Using the Orbis micro-XRF spectrometer to study the microstructure of ancient Roman seawater concrete. Atomic Spectroscopy. pp. 6-7

Sergi, G., Yu, S.W., & Page, C.L. (1992) Diffusion of chloride and hydroxyl ions in cementitious materials exposed to a saline environment. Magazine of Concrete Research. Vol. 44, No. 158, pp. 63-69

Silva, N., Luping, T., & Rauch, S. (2013) Application of LA-ICP-MS for meso-scale chloride profiling in concrete. Materials and Structures. Vol. 46, pp. 1369-1381

Skalny, J., Marchand, J., & Odler, I. (2002) Sulfate attack on concrete. Spon Press. ISBN 0-203-30162-5

Skoog, D.A., West, D.M., & Holler, F.J. (1994) Analytical chemistry An introduction. Sixth edition. Saunders College Publishing

Snyder, K.A., Bentz, D.P., & Davis, J.M. (2012) Using viscosity modifiers to reduce effective diffusivity in mortars. Journal of Materials in Civil Engineering. Vol. 24, No. 8, pp. 1017-1024

Streli, C., Marosi, N., Wobrauschek, P., & Frank, B. (2003) Microanalysis with a polycapillary in a vacuum chamber. The Rigaku Journal. Vol. 20 (2), pp. 25-29

Sudbrink, B., Moradllo, M.K., Hu, Q., Ley, M.T., Davis, J.M., Materer, N., & Apblett, A. (2017) Imaging the presence of silane coatings in concrete with micro X-ray fluorescence. Cement and Concrete Research. No. 92, pp. 121-127

Sutter, L.L., Peterson, K.R., & King, M.T. (2009) Chloride profiling using X-ray microfluorescence. 12th Euroseminar on Microscopy Applied to Building Materials. pp. 129-140

Tittelboom, K.V., Belie, N.D., & Hooton, R.D. (2013) Chapter 10 Test methods for resistance of concrete to sulfate attack – A critical review, In: Performance of Cement-Based Materials in Aggressive Aqueous Environments. State-of-the-Art Report, RILEM TC 211-PAE

The Concrete Society (2014) Technical Report 32: Analysis of hardened concrete – A guide to tests, procedures and interpretation of results. Second edition. ISBN 978-1-904482-82-6

Wall, H. & Nillson, L-O. (2008) A study on sampling methods for chloride profiles: simulations using data from EPMA. Materials and Structures. Vol. 41 (7), pp. 1275-1281

Weritz, F., Ryahi, S., Schaurich, D., Taffe, A., & Wilsch, G. (2005) Quantitative determination of sulfur content in concrete with laser-induced breakdown spectroscopy. Spectrochimica Acta Part B. Vol. 60, pp. 1121-1131

Weritz, F., Taffe, A., Schaurich, D., & Wilsch, G. (2009) Detailed depth profiles of sulfate ingress into concrete measured with laser induced breakdown spectroscopy. Construction and Building Materials. Vol. 23, pp. 275-283

Whittaker, M & Black, L, (2015) Current knowledge of external sulfate attack. Advances in Cement Research, Vol. 27, Issue 9, pp. 532-545

Wilsch, G., Weritz, F., Schaurich, D., & Wiggenhauser, H. (2005) Determination of chloride content in concrete structures with laser-induced breakdown spectroscopy. Construction and Building Materials. Vol. 19, pp. 724-730

Wojcik, G.S. (2004) Determining the uncertainty of X-ray absorption measurements. Journal of Research of the National Institute of Standards and Technology. Vol. 109, No. 5, pp. 479-496

Wong, H.S. & Buenfeld, N.R. (2006) Patch microstructure in cement-based materials: Fact or artefact? Cement and Concrete Research. Vol. 36, Issue 5, pp. 990-997

Wong, H.S. & Buenfeld, N.R. (2006b), Euclidean Distance Mapping for computing microstructural gradients at interfaces in composite materials, Cement and Concrete Research, Vol. 36, No. 6, pp. 1091-1097

Wong, H.S. & Buenfeld, N.R. (2006c), Monte Carlo simulation of electron-solid interactions in cement-based materials, Cement and Concrete Research., Vol. 36, No. 6, pp. 1076-1082

Wong, H.S., Buenfeld, N.R., Hill, J. & Harris, A.W. (2007), Mass transport properties of mature wasteform grouts, Advances in Cement Research, Vol. 19, No. 1, pp. 35-46

Wong, H.S., Zobel, M., Buenfeld, N.R., & Zimmerman, R.W. (2009), Influence of the interfacial transition zone and microcracking on the diffusivity, permeability and sorptivity of cement-based materials after drying, Magazine of Concrete Research, Vol. 61, No. 8, pp. 571-589

Wong, H.S., Zhao, Y.X., Karimi, A.R. Buenfeld, N.R. & Jin, W.L. (2010), On the penetration of rust from reinforcing steel into concrete due to chloride-induced corrosion, Corrosion Science, Vol. 52, pp. 2469-2480

Wong, H.S., Pappas, A.M., Zimmerman, R.W. & Buenfeld, N.R. (2011), Effect of entrained air voids on the microstructure and mass transport properties of concrete, Cement and Concrete Research, Vol. 41, 1067-1077

Wong, H.S., Zimmerman, R.W., Buenfeld, N.R. (2012), Estimating the permeability of cement pastes and mortars using image analysis and effective medium theory, Cement and Concrete Research, Vol. 42, pp. 476-483.

Worley, C.G., Wiltshire, S.S., Miller, T.C., Havrilla, G.J., & Majidi, V. (2006) Detection of visible and latent fingerprints using micro-X-ray fluorescence elemental imaging. Journal of Forensic Sciences, Vol. 51, No. 1, pp. 57-63

Wu, Z., Wong, H.S. & Buenfeld, N.R. (2014), Effect of confining pressure and microcracks on mass transport properties of concrete, Advances in Applied Ceramics, Vol. 113, No. 8, pp. 485-495

Wu, Z., Wong, H.S. & Buenfeld, N.R. (2015), Influence of drying-induced microcracking and related size effects on the mass transport properties of concrete, Cement and Concrete Research, Vol. 68, pp. 35-48

Yio, M.H.N., Wong, H.S. & Buenfeld, N.R. (2016), 3D Monte-Carlo simulation of backscattered electron signal variation across pore-solid boundaries in cement-based materials, Cement and Concrete Research, Vol. 89, pp. 320-331.

Yu, S.W., Sergi, G., & Page, C.L. (1993) Ionic diffusion across an interface between chloride-free and chloride-containing cementitious materials. Magazine of Concrete Research. Vol. 45, No. 165, pp. 257-261

Zhao, Y.X., Karimi, A.R., Wong, H.S., Hu, B.Y. Buenfeld, N.R., Jin, W.L. (2011), Comparison of uniform and non-uniform corrosion induced damage in reinforced concrete based on image analysis, Corrosion Science, Vol. 53, No. 9, pp. 2803-2814

Zheng, J.J., Wong, H.S. & Buenfeld, N.R. (2009), Assessing the influence of ITZ on the steady-state chloride diffusivity of cement-based materials using a numerical model, Cement and Concrete Research, Vol. 39, pp. 805-813